Evaluating the Eco-Hydrochemical Response of Tropical Glacierized Mountainous Watersheds to Climate Change: A Case Study of the Volcán Chimborazo, Ecuador

A THESIS
SUBMITTED TO THE FACULTY OF THE GRADUATE SCHOOL
OF THE UNIVERSITY OF MINNESOTA
BY

Leila Saberi

IN PARTIAL FULFILLMENT OF THE REQUIREMENTS
FOR THE DEGREE OF
DOCTOR OF PHILOSOPHY

Gene-Hua Crystal Ng

May, 2021

Acknowledgements

My journey through my Ph.D. had so many ups and downs and there were many people who made this part of my life journey exciting and helped me through it. First and foremost, I want to thank my friends and family for their unwavering support. To Scott Frayn, who inspired me to walk my own path through life. To my cat Odin: last year has been challenging and I could not imagine going through it without you. Thank you for making my life brighter and for the endless cuddles.

To my advisor, Gene-Hua Crystal Ng: It has been an immense pleasure to work with you. I am incredibly grateful for your compassionate guidance and for you fully supporting me throughout my Ph.D., both professionally and personally. Your input and advice have been invaluable to my professional and personal growth.

I have been fortunate to work with fantastic collaborators over the course of my Ph.D. Most prominent among these are Li Li, Wei Zhi, and Yuning Shi who helped me significantly with model simulations and calibrations. Jeff La Frenierre and Andy Wickert, for their invaluable advice and infinite support with the data collection, field work, and geospatial data analysis. Daniel Stanton, for helping me to understand and visualize the ecology of the site and developing the land cover map. Lian Rampi, for her incredible assistance with the land cover classification. Nate Looker, for assisting with grain size analysis. Veronica Minaya, Carla Manciati, and Xavier Zapata-Rios for their help with the data collection and conducting field work in Ecuador and to all others who I did not mention explicitly here.

Thanks to the other graduate students in the Hydrology research group and department who have been supportive, engaging, and fun. To Harsh Anurag, who has been an incredible friend throughout the graduate school: thank you for always listening and supporting me. I cannot be more grateful for having you by my side during the graduate

school. Kerry Calaghan has been an amazing friend whom I could rely on anytime I needed help. Evan Withing has been the most supportive office-mate I could ask for. Leah Nelson, Alex Waheed, and Maddy Nyblade have been wonderful and supportive friends. Thanks to the friends from AGU Hydrological Section Student Subcommittee (H3S) who expanded my professional horizons and supported me to make long-lasting changes in the hydrologic scientific community for the better. To my lifelong friends Hadis Babaei, Parvaneh Asgarzadeh, Parvin and Ahmad Mokhtari: I am so grateful for having you in my life and thank you for standing beside me through everything and helping me to believe in myself.

For financial support, I am grateful to the NSF for their support under grant no. EAR-1759071. I am also grateful for the Doctoral Dissertation Fellowship (DDF) and Francis Gibson Fellowship offered by the University of Minnesota and Department of Earth and Environmental Sciences that helped me especially through the last year of my Ph.D.

Abstract

With global climate change, some of the highest rates of warming are occurring at high elevations in low latitudes, making tropical glacierized mountains some of the most vulnerable hydrological systems in the world. In the Andes, which hold 99% of all tropical glaciers, observations reveal that streamflow in many watersheds is already decreasing due to the retreat of glaciers. With the water security threat this presents to populations who rely on stream discharge from these glacierized mountains, understanding the hydrological impacts of climate change in these systems is critical. Recent studies have begun to investigate the response of streamflow to fast-retreating glaciers. However, many important knowledge gaps remain. For example, the contribution of meltwater to streamflow through subsurface flow has been largely overlooked, and this may be biasing estimates of how much groundwater may buffer glacier retreat. Further, in addition to causing glacier retreat, warming temperatures are also driving upslope vegetation migration, yet little is known about how this will further affect stream discharge in tropical glacierized watersheds. Finally, climate-driven changes in hydrology can alter solute weathering and transport on glacierized mountain slopes, but the effect on solute export from these watersheds has not been investigated, even though this could have implications for geochemical cycling and ecological function downstream in the Amazon Basin.

Data sparsity in these remote, tropical glacierized mountainous watersheds, as well as unique characteristics such as their year-round glacier ablation and endemic páramo ecosystem, present major uncertainties associated with predicting hydrogeological, hydrochemical, and ecohydrological responses to climate change. We address these challenges by implementing a recently developed watershed model with reactive transport, BioRT-Flux-PIHM, for a sub-humid glacierized watershed on Volcán Chimborazo in the Ecuadorian Andes. BioRT-Flux-PIHM integrates multicomponent reactive transport with hydrological processes and land surface interactions, and thus has the potential to capture spatiotemporally distributed watershed surface and subsurface flows and pathways as well as hydrochemical processes. Implementing BioRT-Flux-PIHM with

available field observations makes it possible extend sparse measurements over space and time, and to uncover unobserved processes.

Our model results indicate that glacier melt contributes a broad range of 10-90% of weekly discharge (∼50% on average) over the course of one study year, mostly through fast surface runoff, but also through infiltration that increases groundwater flow by nearly 37%. Combined removal of glacier melt, upslope migration of vegetation, and a 4.5 °C increase in temperature results in substantial reduction of streamflow by 74% from current conditions, primarily due to an increase in evapotranspiration. Under this scenario, the model shows that near no-flow conditions can occur in the stream, which has crucial implications for local communities who rely on this water for irrigation.

The model further predicted a unique relationship between the concentration (C) of weathering solutes in the stream and discharge (Q) that was mostly chemostatic (constant C with varying Q) because of large melt-supported groundwater inputs, but superimposed by melt event-driven dilution episodes. In a model scenario with no glacier melt, major ion concentrations, including Na^{+}, Ca^{2+}, and Mg^{2+}, became higher and much more stable, but weathering rates decreased, which ultimately attenuated solute export by 23% compared to current-day estimates. We expect this reduction to be exacerbated by higher evapotranspiration and drier conditions with expanded vegetation. This work brings to light the importance of understanding interactions among warming temperatures, mineral weathering, subsurface meltwater flow, and vegetation changes to predict hydrological and hydrochemical processes in tropical watersheds with rapidly retreating glaciers.

Contents

List of Tables

List of Figures

Chapter 1

Introduction

Glaciers store about 70% of the Earth's fresh water and serve as important sources of water for over 600 million people in mountainous regions worldwide (Messerli et al., 2004). By melting during dry seasons and drought years, they supplement streamflow (Fountain & Tangborn, 1985; Lang, 1986; Escher-Vetter et al., 1994; Jansson et al., 2003; Juen et al., 2007; Soruco et al., 2015; Chen et al., 2017) and ensure reliable water supplies (Mark & Seltzer, 2003; Mark & Mckenzie, 2007; Bury et al., 2013). Threatening this resource, the global average air temperature has warmed by 1 °C over the past century, and in response, Earth's glaciers are rapidly retreating. Tropical glaciers are particularly sensitive to increases in temperature due to the year-around ablation they experience even under current climate conditions (Kaser & Osmaston, 2002; Vuille et al., 2008). This is of critical concern in the central Andes, where almost all (99%) of the world's tropical glaciers are located (Kaser, 1999), because glaciers there supply meltwater to resource-limited communities (Bury et al., 2011; La Frenierre & Mark, 2017). Observations already reveal reduced and fluctuating flows in tropical glacierized watersheds (Mark & Seltzer, 2003; Huss et al., 2009; Baraer et al., 2012, 2015), threatening the water security of millions of people (Immerzeel et al., 2010; Carey et al., 2017; Vuille et al., 2018).

Warming and the associated glacier retreat on mountain slopes also alters the hydrologic state of mountainous watersheds by expanding upward the suitable elevation for plant growth. Expansion of vegetation cover due to upslope vegetation migration increases plant water uptake at higher elevations and can thus leave less water for

downgradient regions (Goulden & Bales, 2014; Rasouli et al., 2019). Observations have shown that tropical Andean plants have migrated an average of 25–35 vertical meters upslope per decade, presumably in response to warmer temperatures (Feeley et al., 2011; Morueta-Holme et al., 2015). Although many studies have looked at the direct link between climate change, glacier retreat, and water resources, there has been relatively little attention on the role of plants in mediating the effect of climate on water resources in tropical glacierized watersheds.

Climate-driven changes in tropical glacierized mountains pose an obvious threat for populations living downstream by reducing water availability. These changes can also exert a direct control on solute release and transport, which influences downstream ecosystem productivity and geochemical cycling. While various studies have begun to examine the hydrological impact of glacier retreat in the Andes (Barnett et al., 2005; Ostheimer et al., 2005a; Bradley, 2006; Mark & Mckenzie, 2007; Baraer et al., 2009; Saberi et al., 2019; Somers et al., 2019), little attention has been paid to its implications on geochemical cycling and solute export. Most Andean mountains are located within volcanic zones (Stern, 2004), and they overlie soil and bedrock that are mainly composed of highly reactive silicate minerals (Stallard & Edmond, 1983; Ugolini et al., 2002). Weathering rates are accelerated in humid and tropical mountains by greater gradients (Torres et al., 2015; Wymore et al., 2017a) as well as high temperature and moisture (Ugolini et al., 2002; White et al., 1998). Moreover, transport of the weathering products off of montane slopes with stream discharge is facilitated by the steep topographic gradients in these watersheds (Dessert et al., 2005; Hartmann et al., 2009; Lloret et al., 2013). Despite being thousands of kilometers away and making up only about 13% of the Amazon basin, the combination of high weathering rate and accelerated transport makes tropical Andean mountains an extremely important source of solute and micronutrients for the basin (Gibss, 1967; McClain & Naiman, 2008; Moquet et al., 2018; Wymore et al., 2017a).

Although the tropical Andes are important for the Amazon basin ecosystem, which in turn is a major contributor to global chemical cycling, the role of glacierized tropical mountain watersheds are understudied and poorly characterized (Schlesinger & Bernhardt, 2013). Quantifying the role of tropical glacierized watersheds to regional solute

export is critical because of the fast-changing conditions in these watersheds. This requires an understanding of the factors that control stream chemistry and the effects of changing climate on weathering and solute export in tropical glacierized watersheds.

Understanding how different surface and subsurface pathways as well as spatiotemporally variable processes within the watershed influence the meltwater contribution to streamflow and modulate hydrochemistry of the watershed is critical for predicting how climate change will impact the reliability of watershed discharge and solute export. A major challenge in evaluating these spatiotemporal effects in tropical mountainous watersheds is the relative data sparsity and resource limitation in these regions, compared to better instrumented mountain watersheds in North America and Europe. This data gap and resource limitation serve as obstacles to understanding the response of hydrological and hydrochemical systems to climate change in these vulnerable watersheds, and this calls for an extensive and multiple-approach investigation in order to assess the long-term alteration of watershed hydrology and hydrochemistry in these regions. Our ability to predict the impacts of climate change, future glacier retreat, and upslope migration of vegetation on the hydrological and hydrochemical systems requires understanding complex interactions among climate, hydrology, and ecology at different temporal and spatial scales, and I tackle this challenge using a state-of-the-art computational model that can integrate the dynamic effects of multiple physical, geochemical, and ecological processes within a watershed.

This thesis documents an evaluation of the interactions among groundwater flow, meltwater inputs, vegetation cover, and mineral reactions to answer three overarching sets of questions in a sub-humid glacierized study watershed on Volcán Chimborazo:

1. What is the temporal variability of relative glacier melt contributions to discharge, from hourly to multi-year time scales?

2. How does the hydrochemical system respond to the full retreat of glaciers in a tropical glacierized watershed?

3. How does upslope migration of vegetation, including encroachment of deeper-rooted plants, impact the hydrological system?

To fully understand the eco-hydrogeochemical response of tropical glacierized watersheds to climate change, I developed and implemented an integrated field data and

computational model approach that can resolve multiple processes continuously and over different temporal and spatial scales. Specifically, I leveraged a physically based and coupled land-surface, hydrologic, and reactive transport model called BioRT-Flux-PIHM (Shi et al., 2013; Zhi et al., 2020) to examine the above-mentioned questions.

Structure of this Dissertation

I have written this dissertation as a series of three discrete manuscripts, one of which was published in a peer-reviewed journal (Hydrology and Earth System Sceinces (HESS)), one that is published in the American Geophysical Union (AGU) journal Water Resources Research (WRR), and one that is intended for publication in a peer-reviewed journal. As such, each of the three primary chapters (chapters 2-4) features its own introduction, research site description, methodological overview, results, discussion, and conclusion.

Chapter 2, Multi-scale temporal variability in meltwater contributions in a tropical glacierized watershed offers a comprehensive evaluation of the hydrological process at multiple time scales in a sub-humid tropical glacierized watershed on Volcán Chimborazo in the tropical Ecuadorian Andes to estimate the relative glacier melt contribution to stream discharge. This paper is published in a peer-reviewed journal (Hydrology and Earth System Sceinces (HESS)) (Saberi et al., 2019).

Chapter 3, Spatiotemporal drivers of hydrochemical variability in a tropical glacierized watershed in the Andes, examines the relative roles of subsurface processes, including mineral dissolution and groundwater flow, and year-round glacier melt input, on the export of solutes from a tropical glacierized watershed. This paper is published in the American Geophysical Union (AGU) journal Water Resources Research (WRR) (Saberi et al., 2020).

Chapter 4, Evaluating the Hydrological Response of a Tropical Glacierized Mountainous Watershed to Upslope Vegetation Migration, assesses the impact of upslope migration of vegetation on hydrology of a tropical glacierzied mountainous watershed.

The final chapter, Conclusions and Future Research Directions, briefly summarizes the key findings of this integrative project and identifies possible directions for future research.

Chapter 2

Multi-scale Temporal Variability in Meltwater Contributions in a Tropical Glacierized Watershed

2.1 Introduction

Glaciers supply water resources to over 600 million people worldwide (Messerli et al., 2004). By melting during dry seasons and drought years, they supplement streamflow (Fountain & Tangborn, 1985; Lang, 1986; Escher-Vetter et al., 1994; Jansson et al., 2003; Juen et al., 2007; Soruco et al., 2015; Chen et al., 2017) and ensure reliable water supplies (Mark & Seltzer, 2003; Mark & Mckenzie, 2007; Bury et al., 2013). This has led to the commonly held conceptual model, called the "glacier compensation effect" (Lang, 1986), in which meltwater buffers discharge variability.

Climate change can disrupt the glacier compensation effect, and tropical glacierized watersheds that already experience year-round melt (Kaser & Osmaston, 2002) may be the most vulnerable. Climate models predict amplified temperature increases at high altitudes in low latitudes (Bradley, 2006; Pepin et al., 2015). The retreat of these glaciers temporarily results in increased runoff (Braun et al., 2000; Mark, 2008; Polk et al., 2017; Carey et al., 2017), but gradually depletes the storage of these mountain "water towers". Over time, this reduction in storage capacity can render these glaciers

unable to supply sufficient dry-season meltwater discharge for the communities that depend on it (Barnett et al., 2005; Bradley, 2006; Mackay, 2008; Ostheimer et al., 2005b; Luce, 2018). Indeed, observations already reveal reduced and fluctuating flows in glacierized watersheds (Mark & Seltzer, 2003; Huss et al., 2008; Baraer et al., 2012; Rabatel et al., 2013; Baraer et al., 2015; Soruco et al., 2015), threatening the water security of millions of people (Immerzeel et al., 2010; Carey et al., 2017; Vuille et al., 2018).

Of all glaciers in the tropics, 99% are located in the Andes (Kaser, 1999), often in remote regions, where resource-limited populations rely on their meltwater (Bury et al., 2011; La Frenierre & Mark, 2017). Despite over a decade of research in Peru's heavily glacierized Cordillera Blanca (Mark & Seltzer, 2003; Mark & Mckenzie, 2007; Juen et al., 2007; Mark et al., 2005; Baraer et al., 2012, 2015), many of the processes linking variability in climate, glacier melt, and stream discharge remain uncertain. For example, groundwater is also a major contributor to discharge in many glacierized mountainous watersheds around the world (Clow et al., 2003; Liu et al., 2004; Huth et al., 2004; Hood et al., 2006; Tague et al., 2008; Tague & Grant, 2009; Baraer et al., 2009; Andermann et al., 2012; Baraer et al., 2015; Pohl et al., 2015; Somers et al., 2016; Engel et al., 2016; Schmieder et al., 2018; Harrington et al., 2018). This can further modulate discharge through baseflow, but its capacity to do so as glaciers respond to climate change is complicated by largely unconstrained relationships between glacial meltwater and groundwater recharge (Favier et al., 2008; Baraer et al., 2015; Gordon et al., 2015; Minaya, 2016; Harrington et al., 2018).

Understanding how different surface and subsurface pathways influence the timing of meltwater and groundwater contributions to streamflow is critical for predicting how climate change will impact the reliability of watershed discharge. A major challenge in evaluating these spatiotemporal effects in tropical glacierized watersheds is the relative data sparsity and resource limitations in these regions compared to better instrumented mountainous systems in North America and Europe. Many studies in tropical and other remote glacierized settings rely on focused field campaigns using methods such as synoptic water chemistry tracer sampling (Mark & Mckenzie, 2007; Baraer et al., 2009, 2015; Wilson et al., 2016), but these provide only snapshots of the hydrologic state. Even though physically based hydrologic models can provide greater spatiotemporal

coverage in mountainous settings (e.g., Suecker et al., 2000; Liu et al., 2004; Tague et al., 2008; Tague & Grant, 2009; Lowry et al., 2010, 2011; Markovich et al., 2016; Pribulick et al., 2016; Omani et al., 2017; He et al., 2018), their application is relatively limited in Andean watersheds (previous implementations include work by Buytaert & Beven, 2011; Minaya, 2016; Omani et al., 2017; Ng et al., 2018) due to the lack of extensive monitoring infrastructure. With these obstacles, there remains limited understanding of how stream discharge in tropical glacierized watersheds varies over time scales ranging from hours to years, and how this variability is driven by dynamic inputs of glacial meltwater and precipitation through a combination of surficial and subsurface pathways.

In this study, we probe the multiple time scales of hydrological processes in a sub-humid glacierized watershed on Volcán Chimborazo in the tropical Ecuadorian Andes. Prior to this work, there have been no comprehensive efforts on Chimborazo to quantify glacier melt as a component of watershed discharge. In contrast to the well-studied crystalline-cored Cordillera Blanca in the outer tropics, Chimborazo is a stratovolcano located in the inner tropics, and therefore experiences less-pronounced seasonality in precipitation (Kaser & Osmaston, 2002) and more persistent ablation due to higher humidity (Vuille et al., 2003; Favier, 2004; Harpold & Brooks, 2018). Higher humidity can enhance ablation rates by increasing net longwave radiation and condensation (Harpold & Brooks, 2018). Most mixing model analyses of melt contributions in the outer tropics have been limited to the dry season, leaving wet season effects less well understood. In the inner tropics, coincident glacier melt and precipitation inputs throughout the year could lead to multiple processes simultaneously driving discharge variability that are difficult to disentangle. Furthermore, Andean volcanoes may feature fractured bedrock aquifers that support greater groundwater storage and baseflow than those in crystalline-cored mountainous watersheds (Tague & Grant, 2009; Markovich et al., 2016), adding another factor to be reconciled. A growing body of work at Volcán Antisana, also located in the inner tropics, has begun to shed light on its hydrogeologic (Favier, 2004; Caceres et al., 2006; Favier et al., 2008; Cauvy-Fraunié et al., 2013) and ecohydrologic (Minaya, 2016) conditions, but comprehensive understanding of mountain hydrology in the inner tropics still greatly lags that in the outer tropics.

Here, we implement field and computational methods to answer two questions: (1) What is the temporal variability of relative glacier melt contributions to discharge, from

hourly to multi-year time scales, in a sub-humid glacierized watershed on Volcán Chimborazo? (2) What hydroclimatic factors control this variability? Our approach comprises three methods: mixing model analysis applied to repeat synoptic sampling; time series analysis of hydroclimatic data; and numerical watershed modeling. Each method interrogates a distinct temporal relationship, and synthesizing their results illuminates how the dominant surface and subsurface processes driving the hydrological response of a tropical glacierized watershed vary as a function of time scale.

2.2 Study Area

Volcán Chimborazo is a glacierized stratovolcano in Ecuador (Figure 3.1a) whose glaciers serve as the headwaters for four major river systems – the Rio Mocha (NE flank), Rio Colorado (NW flank), Rio Guano (SE flank), and Rio Chimborazo (SW flank) – that supply water to a population of over 200,000 (INEC, 2010). Located in the inner tropics, Chimborazo's climate is characterized by minimal intra-annual temperature variation ($\sim$2 °C) and moderately seasonal precipitation, with two wetter seasons of unequal length (February-May and October-November) (Clapperton, 1990), and two intervening drier seasons that have less but not negligible amounts of precipitation. Moisture mostly originates from the Amazon Basin to the east (Vuille & Keimig, 2004; Smith et al., 2008a), which produces a steep northeast (up to 2000 mm/yr) to southwest ($<$500 mm/yr) precipitation gradient across the mountain (Clapperton, 1990). Driving interannual climatic variability at the regional scale, El Niño generally brings drier and hotter conditions throughout the Andes (Vuille & Bradley, 2000; Wagnon et al., 2001; Francou, 2003; Bradley et al., 2003; Vuille & Keimig, 2004; Smith et al., 2008a), which enhances glacier ablation (Wagnon et al., 2001; Favier, 2004; Veettil et al., 2014b).

Records since 1980 indicate that, consistent with the rest of the tropical Andes, temperatures have warmed 0.11 °C decade^{-1} around Volcán Chimborazo (Vuille et al., 2008; La Frenierre & Mark, 2017). This likely caused the 21% reduction in ice surface area and 180 m increase in mean minimum elevation of clean ice observed between 1986 and 2013 (La Frenierre & Mark, 2017). Although regional precipitation gauges show no notable change over time, local residents report a reduction in precipitation, which could further drive glacier mass balance changes (La Frenierre & Mark, 2017).

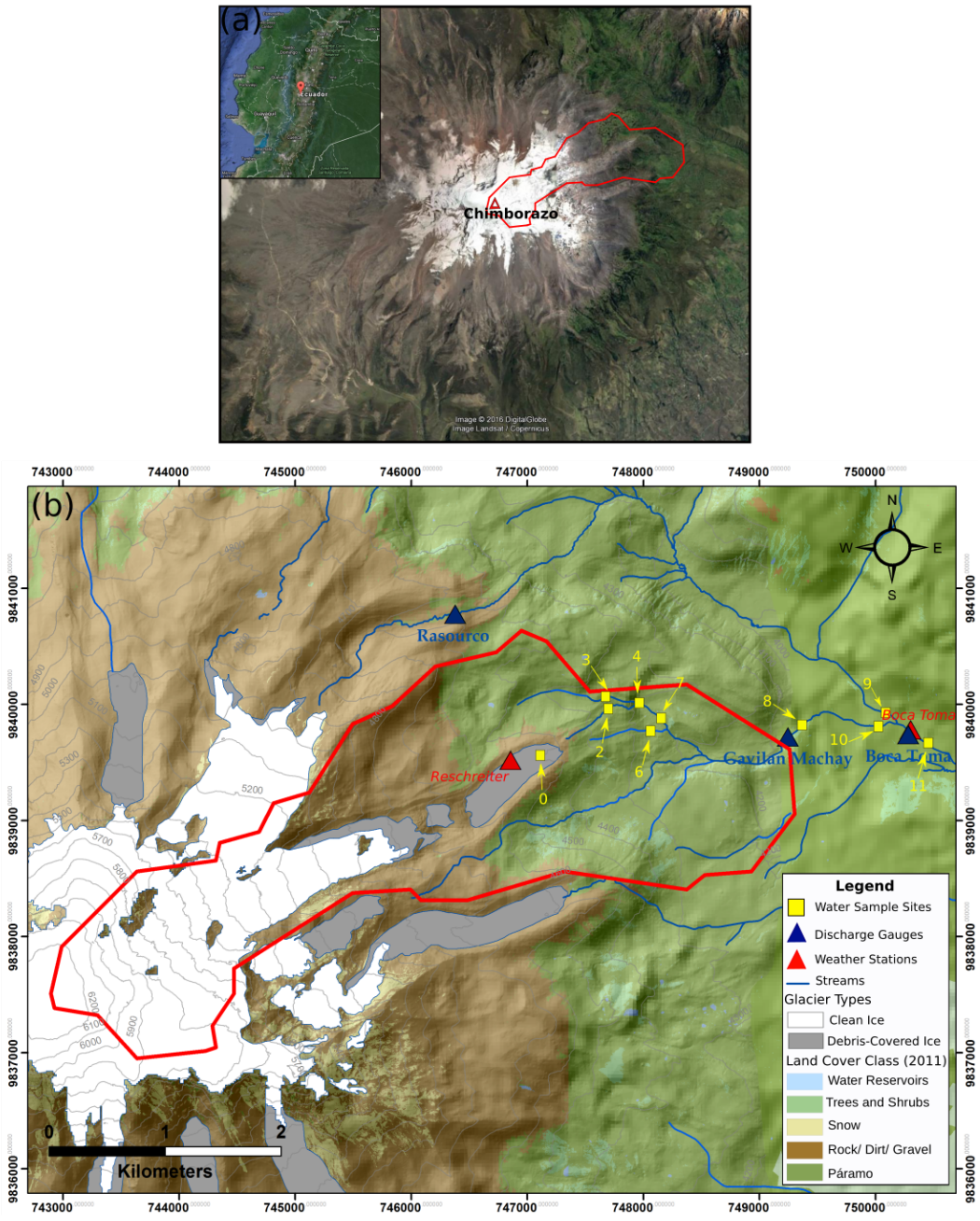

Figure 2.1: (a) Satellite image of Volcán Chimborazo, with the study watershed Gavilan Machay outlined in red, and its location in Ecuador shown in the inset map. The glacierized Gavilan Machay watershed is a relatively humid watershed compared to the western flank of Chimborazo. (b) Land cover and locations of monitoring stations and water sampling within the Gavilan Machay watershed.

Historical records of glacier melt are not available. Under current conditions, only four of Chimborazo's seventeen glaciers, including the two largest, Reschreiter (2.55 km^2) and Hans Meyer (1.33 km^2), generate perennial surface discharge, nearly all of which flows northeast into the Río Mocha watershed. The lowest 16% of Reschreiter Glacier is debris-covered, providing insulation that stabilizes ice at lower elevations (4480 m a.s.l.) than would be expected for clean ice, given current climatic conditions. Our study focuses on the 7.5 km^2 Gavilan Machay sub-catchment on the sub-humid northeast flank of Chimborazo (Figure 3.1b), which is 34% glacierized by Reschreiter and is of concern because it discharges into the main Río Mocha channel just upstream of the Boca Toma diversion point (3895 m a.s.l. elevation) for an irrigation system.

In addition to glacier melt, groundwater and ecological conditions also control the hydrology of the Gavilan Machay watershed. Springs are prevalent below 4400 m a.s.l. Geologic maps and stratigraphic interpretations (Barba et al., 2005; Samaniego et al., 2012) support field evidence for aquifers within unsorted glacial deposits and fractured bedrock (McLaughlin, 2017). Extensive areas of páramo, the biologically rich grasslands endemic to the tropical Andes above ∼3500 m a.s.l., are common across the watershed. Wet páramos commonly contain homogeneous Andosol soils of volcanic origin that can accumulate elevated organic carbon content; this typically gives rise to high porosity, infiltration capacity, hydraulic conductivity, and water retention (Buytaert et al., 2006; Buytaert & Beven, 2011). Absorbent páramo soils are considered to very efficiently regulate watershed discharge throughout Andean Ecuador (Buytaert et al., 2006; Buytaert & Beven, 2011; Minaya, 2016).

2.3 Methods

2.3.1 Hydroclimatic Data

Precipitation, temperature, and relative humidity data were collected from October 2011 to February 2017 from weather stations installed at 4515 m a.s.l. on the debris-covered portion of Reschreiter Glacier and at 3895 m a.s.l. at Boca Toma (Figure A1). Logistical obstacles prevented instrumentation of the upper three-quarters of the watershed above Reschreiter. The Boca Toma weather station was deployed with an Onset Hobo Pendant® Event Logger starting June 16, 2015. The Reschreiter weather

station was deployed with an Onset Hobo Micro Station starting October 2011, but temperature and precipitation data recovery was discontinuous. The short data records from Reschreiter were primarily used together with Boca Toma data to determine a lapse rate for precipitation. Precipitation in mountainous watersheds typically exhibit piecewise linear relationships with elevation, with positive (negative) lapse rates below (above) the elevation of maximum precipitation (Wang et al., 2016). We calculated a negative lapse between the two weather stations, which we applied over the entire watershed with the assumption that the elevation of maximum precipitation lies below the watershed. Uncertainty in this approach arises from the actual unconstrained elevation of maximum precipitation (which requires more than two weather stations), and from unquantified precipitation measurement errors that may be caused by wind and freezing temperatures at high elevations. Glacier melt was separately estimated through model calibration to stream discharge data (Section 2.3.3), which may compensate for errors in the precipitation inputs. Temperature lapse rates were calculated using data collected at glacier ablation stakes (described further below) over June 2016 to November 2016. Relative humidity measured at the Boca Toma station was applied over the entire watershed due to the lack of measurements elsewhere. Discharge simulations should be less sensitive to errors in relative humidity compared to precipitation and temperature, which directly control water inputs to the watershed. We obtained unmeasured meteorological variables (wind speed, solar radiation, longwave radiation, and air pressure) from the Global Land Data Assimilation Systems (GLDAS) (Rodell et al., 2004). A discharge gauging station equipped with a Solinst Levelogger Junior pressure transducer was established at Gavilan Machay, 1.1 km upstream of the Río Mocha confluence. Solinst Barologger measurements at Boca Toma were applied to correct for atmospheric pressure, and standard USGS rating curve techniques (Andrews, 1981a,b) were used to convert water depth to discharge over the period of record (Figure A1).

In June 2016, glacier ablation stakes were installed at two elevations on the Reschreiter Glacier tongue (4792 and 4820 m a.s.l.) and one on the Hans Meyer Glacier tongue (4925 m a.s.l.), all in clean ice. Each stake included a temperature sensor, along with a look-down ultrasonic sensor for measuring changes in distance to the ice surface to estimate glacier mass loss in clean ice. The stakes were deployed using the open-source Arduino-compatible ALog data logger (BottleLogger v1.4.0, an intermediate model

between v1.0.0 (Wickert, 2014) and v2.2.0 (Wickert et al., 2019)). All sensors were mounted at the top of 3 m long PVC tubes, which were inserted into holes drilled to about 2.5 m depth. In addition to the clean-ice mass loss determined with ablation stakes, glacier volume change of debris-covered ice was estimated by differencing a GPS-validated photogrammetric digital elevation model in 1997 and terrestrial laser scanner (Riegl LMS-Z620) surveys in 2012 and 2013 (La Frenierre & Mark, 2017). Because of the sparse spatiotemporal coverage of these glacier melt measurements, these were used only as comparisons for calibrated glacier melt and were not directly applied in our analysis.

Hydroclimatic data collected in the watershed were directly assessed using statistical analyses and implemented as inputs to the integrated hydrologic model. For the statistical analysis, we calculated cross-correlations to probe how the discharge time series may be driven by different climatic factors. Spectral analysis provided further insight on the time scales, represented by time-frequency, over which these interactions occur. Specifically, we examined the magnitude squared coherence (C_{xy}) over time-frequency (f):

$$C_{xy}(f) = \frac{|S_{xy}(f)|^2}{S_{xx}(f)S_{yy}(f)} \tag{2.1}$$

where $S_{xx}(f)$ and $S_{yy}(f)$ are auto-spectral densities of variables x and y, respectively, and $S_{xy}(f)$ is the cross spectral density of x and y. Like the square of a correlation, the magnitude squared coherence varies between 0 and 1, with 0 indicating the weakest relationship between the two variables at frequency f and 1 indicating the strongest relationship.

2.3.2 Hydrochemical and Isotopic Tracers

2.3.2.1 Field Sampling

Water samples were collected for use in the Hydrochemical Basin Characterization Model (HBCM) (Section 2.3.2.3), a hydrochemical mixing model that spans the stream network and requires synoptic water sampling over a sufficiently short time period such that data reflect spatial and not temporal variability. We carried out five synoptic sampling campaigns during January 1-8, 2012; July 7-9, 2012; June 12-15, 2015; June 25-30,

2016; and February 4-7, 2017. The June and July (January and February) samples represent the longer (shorter) dry season. Dry seasons were targeted because of water resource interests during these periods; integrated hydrologic model simulations served to extend the analysis to wet seasons. In addition to limiting the number of days spanned during a sampling campaign, synoptic sampling should avoid hourly timescale hydrochemical fluctuations. All samples were collected between mid-morning and mid-afternoon. In February 2017, we confirmed that 1-minute resolution specific conductivity changes over a 24-hour time period at the Reschreiter glacier tongue were an order of magnitude smaller than the spatial variability across the Gavilan Machay subcatchment (details in McLaughlin, 2017). Logistical difficulties prevented similar measurements farther downstream in the watershed, where dynamic melt versus groundwater contributions likely caused greater hydrochemical variability (Section 2.4.1).

During each of the five campaigns, we collected water samples from meltwater (which may contain both glacier melt and snowmelt), springs, and precipitation, as well as at stream confluence mixing points (locations shown in Figure 3.1b). Spring samples from concrete capture boxes or natural valley wall seeps represent groundwater, which consists of an unconstrained mix of shallow saturated soil water from páramo areas, morainic debris aquifer water, and deeper fractured bedrock aquifer water. Precipitation samples were collected using evaporation-proof totalizing rain gauges deployed for 3-6 days at Boca Toma, near the Reschreiter weather station, and near Hans Meyer glacier (at 4780 m a.s.l.). Each field campaign covered most of the same sampling locations between the Reschreiter glacier tongue and the Gavilan Machay confluence. The 2012 and 2017 sampling periods included additional stream samples between some confluences to estimate groundwater contributions along shorter stream reaches (Figure 2.2b). For each sampling site, 30mL of water were collected, filtered in the field using either 0.45 μm (before 2017) or 0.2 μm (2017) filters, and stored in Nalgene bottles that were capped and sealed with electrical tape, and then stored near 4 °C as soon as possible.

2.3.2.2 Laboratory Analysis

In 2012, major dissolved ions (Li^+, Na^+, K^+, Mg^{2+}, Ca^{2+}, F^-, Cl^-, NO_3^-, PO_4^{3-} and SO_4^{2-}) were measured using a Dionex DX500 Ion Chromatographer at the Water Isotope and Nutrient Laboratory at The Ohio State University, and stable isotopes of

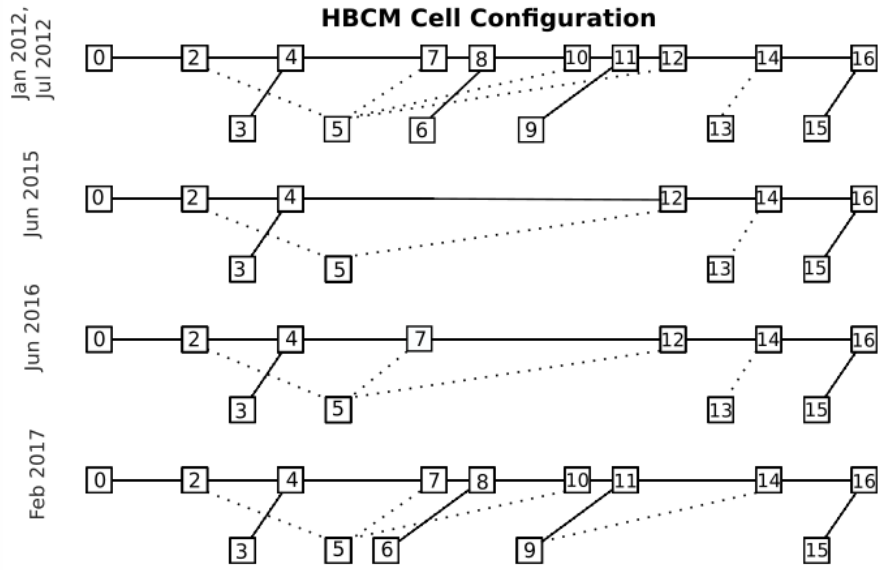

Figure 2.2: Different computational cell configurations for the HBCM mixing model based on the available samples (site codes in squares, see Figure 3.1) for each of the five periods. The upper solid line for each period represents the main channel. The lower solid lines depict tributary links for confluence cells, and the lower dotted lines show groundwater inputs to the main channel for reach cells.

water (δ18O and δ2H) were measured using Piccaro L2130-i CRDS isotope analyzers at the Water Isotope and Nutrient Laboratory and at the Byrd Polar and Climate Research Center. In 2015-2017, cations (Na^+, K^+, Mg^{2+}, Ca^{2+}) were measured using an Agilent 7700X Inductively Coupled Plasma-Mass Spectrometer (ICP-MS) at Gustavus Adolphus College, anions (F^-, Cl^-, SO_4^{2-}) were measured using a Dionex ICS1000 Ion Chromatographer (IC) also at Gustavus Adolphus College, and stable isotopes of water (δ^{18}O and δ^2H) were measured at the University of Minnesota using an LGR DLT-100 Liquid Water Analyzer (a laser spectroscopy system). We calculated the bicarbonate (HCO_3^-) concentration as the charge balance residual. Reported isotope ratios are relative to the Vienna Standard Mean Ocean Water (VSMOW) and typical precisions are $\pm$1.0 for deuterium/hydrogen values and $\pm$0.25 for $^{18}O/^{16}O$ values. Checking for consistency across instruments, we confirmed that bulk concentrations at each location and spatial trends for each analyte were similar across sampling periods (Figure A3). Certain analytes did exhibit a discernible systematic bias for a particular sampling period,

which may be related to laboratory instrument, but this should not pose a problem for the mixing model, because it is implemented only using data within the same sampling period (measured on the same instrument).

2.3.2.3 Mixing Model: Hydrochemical Basin Characterization Model (HBCM)

Naturally occurring dissolved ions and stable isotopes of water (δ^{18}O and δ^{2}H) are commonly used to track the relative contributions of different surface source waters to total watershed discharge (Hooper & Shoemaker, 1986; Mark & Seltzer, 2003; Ryu et al., 2007; Mark & Mckenzie, 2007; Baraer et al., 2009), as well as to identify groundwater flow paths (Clow et al., 2003; Kendall et al., 2003; Baraer et al., 2009; Crossman et al., 2011; Baraer et al., 2015). Here, the proportion of glacier and snow melt versus groundwater in discharge at the Gavilan Machay watershed is quantified using HBCM, a multicomponent hydrochemical mixing model developed for use in data-sparse, glacierized tropical watersheds (Baraer et al., 2009). Given source (or "end-member") and outflow chemistries at different mixing points throughout the watershed, HBCM solves an overconstrained set of mass balance equations for multiple tracers to determine the relative flow contributions of each source. Details are provided in the Appendix A (HBCM Section).

As with all hydrochemical mixing models, HBCM's calculation of relative source contributions depends on three fundamental assumptions: (1) end-member chemistry is unique and spatially homogeneous within the analysis area; (2) tracers are chemically conservative within the analysis; and (3) end-member mixing is instantaneous and complete (Christophersen et al., 1990; Soulsby et al., 2003). A unique feature of HBCM is that it represents spatial information within a watershed through a series of cells that are interconnected by having outflow from one become inflow to a subsequent downstream cell. There are two types of cells, both of which have streamflow at the upgradient end of the cell as a source and streamflow at the downgradient end of the cell as the mixed water output. "Reach cells" have groundwater as their other source, and "confluence cells" have tributary water as their other source (see cartoon in Figure A2). Note that this makes end-members for a particular HBCM cell different than for the full watershed, which has only meltwater and groundwater as sources contributing to discharge at the outlet. Figure 2.2b shows the conceptual schematics of the Gavilan

Machay cell configuration for the five sampling periods.

Although HBCM only requires the three assumptions to be met on a cell-scale, we carried out a preliminary watershed-level analysis considering groundwater and meltwater as sources to all mixed stream samples, in order to identify potential conservative tracers that are reasonable candidates for all cells. Appropriate tracers should show end-members appearing on opposite ends of a line formed by mixed samples in bivariate plots, and samples for different end-members should group separately from each other in hierarchical cluster analysis diagrams (Christophersen et al., 1990; Hooper, 2003; James & Roulet, 2006). Stable isotopes were excluded as tracers for reach cells, because the groundwater likely has a range of isotopic values due to different recharge elevations.

To bracket some of the uncertainty in the method, HBCM generates estimates of fractional contributions from each source using different combinations of potential tracers. The final result consists of a range of estimates that produce similar (within about three times the minimum) cumulative residual errors between the measured tracer concentrations in the mixed outflow water and that predicted by the over-constrained mixing model. This quantifies uncertainty due to the model's inability to distinguish among equally good optimization results but represents only a lower limit of error, because it does not account for the mismatch between the observed and predicted mixed concentration outflows. There are no straightforward methods to convert the sum of residual concentration flux errors to estimated source contribution errors.

2.3.3 Integrated Hydrologic Modeling

Spatially distributed watershed models can integrate surface hydrology and groundwater flow through time to evaluate their joint impacts on water resources. Over the one-year period of June 2015-June 2016 when continuous air temperature and precipitation measurements are available in the watershed, we implemented Flux-PIHM version 0.5.0 (Shi et al., 2013), an intermediate complexity watershed model that balances mechanistic parameterizations with computational efficiency. Full details about Flux-PIHM can be found in Qu & Duffy (2007) and Shi et al. (2013); here, we summarize the major features. Flux-PIHM couples physically based equations for canopy interception, infiltration, surface and subsurface water flow, and snow melt with the energy balance

scheme of the NOAH land-surface model (Ek et al., 2003) for more accurate simulation of evapotranspiration. Flux-PIHM employs a semi-discrete finite volume approach on an unstructured grid that performs efficiently on steep topographies. Channel and overland flow are represented by diffusion wave approximations to St. Venant equations, shallow groundwater flow follows a 2D Dupuit approximation, and unsaturated zone flow is based on a 1D form of Richards equation. The model simulates water storage in one vertically integrated unsaturated zone layer and one vertically integrated saturated zone layer, providing a "2.5D" distributed model. Other PIHM family codes include the watershed reactive transport module RT-Flux-PIHM (Bao et al., 2017; Li et al., 2017b), hydrologic and landscape evolution module LE-PIHM (Zhang et al., 2016), among a suite of other functional modules (Duffy et al., 2014).

Flux-PIHM determines snowmelt based on energy balance. Use of coarse-scale GLDAS radiation inputs introduces errors, but as will be discussed in Section 2.4.3.1, precipitation limitations may make snowmelt calculations less sensitive to radiation input uncertainties compared to glacier melt calculations. Due to the unavailability of high resolution radiation input measurements as well as intensive source-code modifications required to couple energy balance calculations for ice melt into the Flux-PIHM, we added a separate module to simulate glacier melt using a temperature index scheme (NRCS, 2009). Although the accuracy of a temperature index glacier melt model for tropical glaciers can be uncertain due to uncaptured effects of solar radiation, cloud cover, humidity, topography, and aspect (Hock, 1999, 2005; Pellicciotti et al., 2005; Sicart et al., 2008; Huss et al., 2009; Gabbi et al., 2014; Fernández & Mark, 2016), it remains the most feasible approach in poorly instrumented watersheds given its simplicity and limited field data requirement compared to an energy balance approach (Hock, 2005; Fernández & Mark, 2016; Reveillet et al., 2017). The temperature index glacier melt model includes:

$$F_I = \begin{cases} M_I(T_a - T_{M,I}) & \text{if } T_a > T_{M,I} \\ 0 & \text{if } T_a \leq T_{M,I} \end{cases} \tag{2.2}$$

where F_I is the ice melt rate (m/hr), T_a is air temperature in the grid cell containing ice (°C), M_I is the melt factor parameter (m/hr/°C) to be calibrated, and $T_{M,I}$ (°C) is set to 0°C as the air temperature threshold for ice to melt. Over the simulated time period,

we assume that there is an unexhausted supply of ice that can melt in the glaciated grid cells below the equilibrium line altitude (ELA) at ∼5050 m a.s.l. (La Frenierre, 2014), which is a reasonable approximation over the one-year simulation period. The melt simulated with the temperature index model was added to the precipitation amount for the Flux-PIHM forcing inputs.

We used the PIHMgis software (Bhatt et al., 2014) to construct an unstructured domain of 188 cells over the Gavilan Machay subcatchment using a 30 m resolution Shuttle Radar Topography Mission (SRTM) Digital Elevation Model (DEM) (Farr et al., 2007). Although a major feature of PIHMgis is its tight integration with spatial and temporal datasets for model inputs such as soil properties and meteorological forcing, these datasets only cover densely monitored regions, mostly within North America and Europe. For meteorological forcing, we used the spatially distributed inputs described in Section 2.3.1. Vegetation mapping by McLaughlin (2017), based on 30-cm resolution aerial photo surveys conducted by the Sistema Nacional de Información de Tierras Rurales e Infrastructura Tecnológica (SIGTIERRAS; `http://www.sigtierras.gob.ec/descargas/`), provided land-cover types and boundaries. Built-in land-cover parameters from Noah-LSM were used for the "grassland/herbaceous" type at lowest elevations corresponding to páramo, the "barren/sparsely vegetated" type for intermediate elevations with rock/dirt/gravel, and the "perennial ice/snow" type for the ice-covered areas. This approach simplifies the mix of tussock grasses, acaulescent rosettes, and cushion plants that make up the páramo into a single representative "grassland/herbaceous" type in order to reduce the calibration burden. For the grassland/herbaceous land cover type, the default monthly Leaf Area Index (LAI) values were replaced with measurements from MODIS (Vermote, 2015) to avoid using incorrect seasonal changes from the original model settings for this tropical region. Hydraulic parameters were manually calibrated to match observed discharge at Gavilan Machay.

2.4 Results and Discussion

This section presents the respective insights gained from each of the three methods on the temporal relationship among meltwater, groundwater, and discharge: the mixing model analysis offers discrete multi-year estimates over five years; the time series analysis

shows fine-scale hourly resolution correlations; and the integrated hydrological model explores intermediary weekly to seasonal processes within a one-year simulation period containing a strong El Niño event. A complete interpretation of the multi-scale temporal variabilities and their hydroclimatic controls emerges in Section 2.4.3.2 when evaluating the model simulations in relation to the mixing model and time series analysis results.

2.4.1 Mixing-model analysis of meltwater contributions to discharge

Total cation concentrations provide a summary representation of hydrochemistry results from the five dry-season synoptic sampling periods in Figure 2.3. These plots show that even though hydrochemical conditions vary over the different periods, groundwater samples, which geochemically interact with soil and rocks, consistently contain much higher ion concentrations than meltwater samples. The distinctive chemistries of groundwater and meltwater make it possible to use the mixing model approach to estimate their relative contributions to streamwater, which shows an increase in ion concentration while moving downgradient due to the cumulative addition of groundwater (see Figure 3.1b for sample locations). We chose as tracers those analytes that most consistently showed the mixed sample visually falling close to the line between its two source samples in the bivariate plots in Figures A4-A8: sum of monovalent cations, Mg^{2+}, Ca^{2+}, Cl^{-}, and HCO_3^{-}. Hierarchical cluster analysis lends confidence that these five potential tracers can be used in the mixing model analysis to distinguish between groundwater and melt samples as different watershed-level end-members (Figure A9). Precipitation was not included as an end-member, because precipitation samples tended to plot outside the range of stream samples bracketed tightly by groundwater and meltwater samples in bivariate plots. Rather than directly add to streamflow, most of the precipitation that fell close to the sampling time likely evapotranspired or infiltrated and contributed to streamflow through groundwater.

HBCM results in Figure 2.4 illustrate the importance of both meltwater and groundwater in the watershed. Surficial meltwater comprises between 23-66% of discharge during the five dry-season sampling periods, with groundwater constituting the remaining 34-77% at any given time. Notable differences were observed across the sampling periods. The higher relative melt contribution during February 2017 compared to January 2012 could reflect the accelerating melt rates observed on Chimborazo (La Frenierre

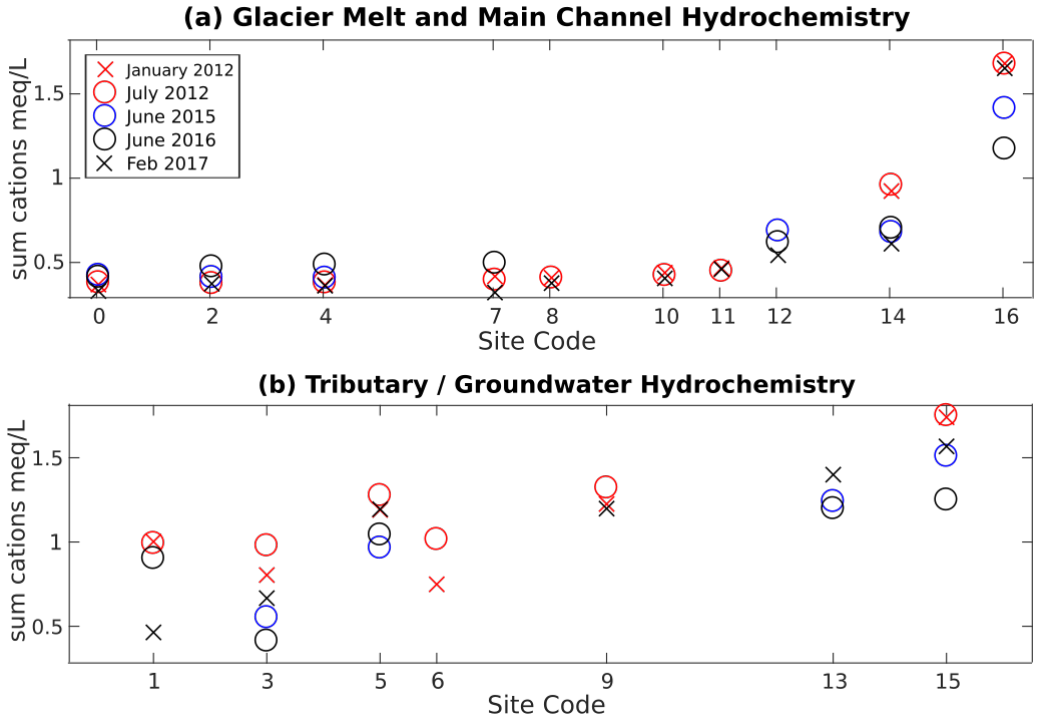

Figure 2.3: (a) Hydrochemistry at different sampling locations along the Gavilan Machay main channel shows variability in space and over the five sampling periods; site codes are ordered from highest (0 for meltwater) to lowest (16 for Boca Toma) elevation (see Figure 3.1b). (b) Hydrochemistry for different tributary (sites 3, 6, 9, and 15) and groundwater (spring) samples (sites 5 and 13), ordered from highest to lowest elevation, show variability in space and time.

& Mark, 2017). However, the absolute melt contribution, determined by applying estimates of relative melt contributions to average observed weekly discharge measurements around the sampling time, was in fact lowest in February 2017, because of significantly less total discharge compared to the other sampling periods (Figure 2.4b). The lower total discharge was likely due to lower precipitation and temperature during the weeks around the sampling period compared to during the other sampling periods (Figure A1). Our findings across the five sampling periods demonstrate that one single synoptic tracer test should not be directly generalized or interpreted without considering temporal dynamics and groundwater conditions.

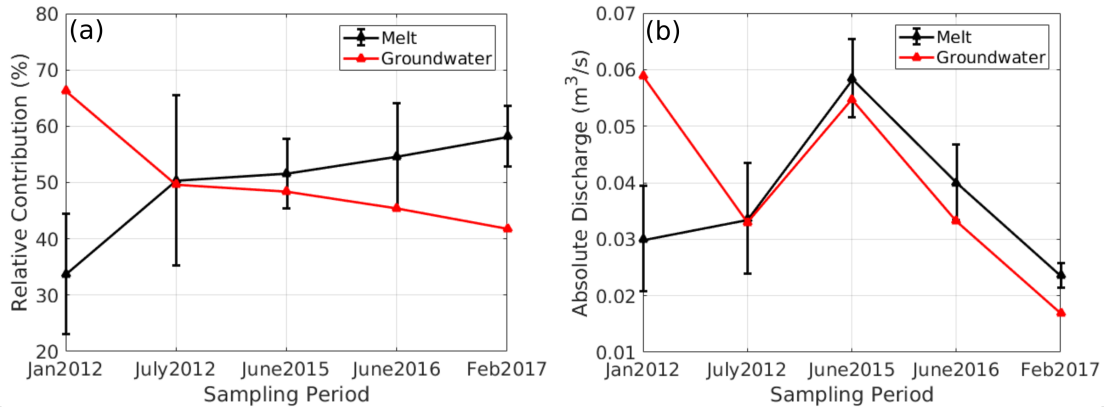

Figure 2.4: The HBCM mixing model predicts a range in relative surficial meltwater contributions to discharge over five discrete sampling times, which may reflect both temporal changes and uncertainties. Error bars bracket HBCM estimates that produced similar best matches to observed tracer concentrations; however, actual uncertainties are higher because of residual errors. Absolute meltwater discharge contributions can vary in time very differently than relative inputs, in part due to varying groundwater contributions.

Our results show Volcán Chimborazo to deviate from trends found at the well-studied Cordillera Blanca, likely due to its distinct climatic and geologic conditions. When compared to an exponential fit between relative groundwater contribution and glacierized fraction for four watersheds in the Cordillera Blanca (Baraer et al., 2015), our estimates for groundwater contributions in Gavilan Machay are approximately twice as large. Also, the glacierized Gavilan Machay sub-catchment of the Upper Río Mocha watershed has a specific discharge that is less than half of that in the non-glaciated portion, in contrast to the greater specific discharge generally found with greater glacierized areas in the Cordillera Blanca (Baraer et al., 2009; Mark & Seltzer, 2003).

HBCM implementation with five different field campaigns enabled us to evaluate uncertainties due to distinct sampling plans. We found that changing HBCM cell configurations could generate up to a 23% melt fraction difference in estimates. Also, having fewer HBCM analysis cells (e.g., longer stream reaches) and fewer groundwater samples consistently led to greater HBCM residual errors. Too few groundwater samples

becomes problematic when groundwater is not a homogeneous end-member throughout the watershed, which is the case in Gavilan Machay, which contains springs with somewhat higher solute concentrations at lower elevations (Figure 2.3b). Further, errors in the estimated groundwater contribution grow when using fewer and longer reach cells, because with additional and shorter reach cells, observations can reset the stream channel chemistry to correct concentrations. These results demonstrate the importance of adequately measuring the spatial variability of the surface and subsurface flow network, and they prompt the use of alternative methods to help constrain uncertainties in HBCM analysis results.

2.4.2 Time series and spectral analysis of hydroclimatic controls

Because of the uncertainties and long time gaps in the HBCM analyses, we applied statistical analyses to the continuous data available from July 2015 to March 2016 at the Boca Toma weather station and Gavilan Machay gauging station to further infer characteristic trends between meltwater and discharge and their climatic controls. Considering air temperature as a proxy indicator of meltwater, the hourly cross correlation of air temperature leading discharge at Gavilan Machay in Figure 2.5a shows a strong diurnal signal, with peak discharge occurring four hours after the warmest part of the day at an average rate (0.1 m^3/s) that is about twice the magnitude of average morning discharge.

To determine if melt could be driving discharge variability beyond diurnal time scales, we examined the magnitude squared coherence between temperature and discharge in Figure 2.5c, which quantifies their correlation at a certain period (inverse time-frequency). As expected from the time-series results, the most prominent feature is the peak at a period of 24 hours. Interestingly, the next highest coherence is at a period of 12 hours. While this could be a harmonic artifact of the dominant 24-hour trend, it is supported by a slight temperature increase commonly observed around 11pm. The resulting increase in discharge, while detectable, is inconsequential to the total daily water balance. Other very narrow coherence peaks at periods less than 12 hours are likely spurious, because the power spectral densities of both temperature and discharge are low over that range (Figure A10). However, the smaller but broader peak around 50 to 60 hours suggests that multi-day warming may also drive multi-day discharge events,

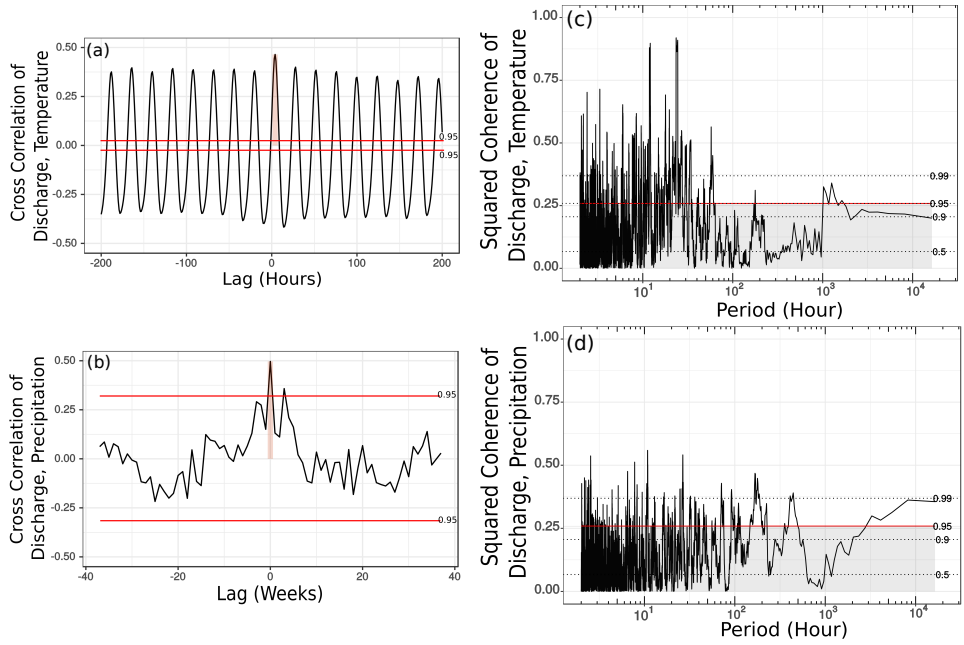

Figure 2.5: Cross-correlations (with 95% confidence interval shown) of observed discharge at Gavilan Machay with (a) hourly temperature and (b) weekly precipitation show that discharge has a clear diurnal link with temperature at about a 4 hour lag and a strong relationship with weekly precipitation, respectively. Magnitude squared coherence (with various confidence intervals shown) between discharge and (c) temperature exhibits a high peak at 24 hours corresponding to the cross-correlation result, as well as a strong peak at 12 hours, and a more moderate peak at a multi-day scale. The coherence between discharge and (d) precipitation peaks between 100 to 200 hours (about 1 week) and may also be significant at scales approaching one year.

though this link is much weaker than the diurnal response.

The substantial groundwater contributions to discharge inferred from the HBCM analysis prompts a look at not only melt but also precipitation controls on multi-day discharge. Hourly precipitation and discharge are very weakly correlated (Figure A11a); however, a significant correlation of 0.5 appears for weekly averages with zero time lag (Figure 2.5b). Correspondingly, a high (above 95% confidence interval) and broad coherence peak between precipitation and discharge can be seen over periods of about one week (168 hours) (Figure 2.5d). Together, these results suggest that sustained rain events influence discharge over a week, and therefore that rainwater tends to infiltrate

instead of flow quickly overland. Other statistically significant (at the 95% confidence interval) coherences between discharge and both temperature and precipitation across multi-week to multi-month periods further support the role of even slower subsurface flow pathways.

Combining the time series analysis with the HBCM results suggests that streamflow at Gavilan Machay is heavily influenced by both surficial meltwater and groundwater, and that the latter is driven by precipitation. Furthermore, time series and spectral analyses highlight temporal links not easily found through a fieldwork-intensive tracer-based approach: meltwater feeds discharge at Gavilan Machay on an hourly time scale, while weekly discharge responds most strongly to precipitation events. There are, however, limitations to this statistical assessment that result from the short nine-month dataset, which precludes robust examination of any seasonal to multi-year responses to bimodal wet and dry seasons and El Niño effects. Hydrologic modeling in the following section can address this, as well as questions about the quantitative role of melt contributions or groundwater buffering periods of low rainfall.

2.4.3 Integrated Hydrologic Model Simulations

2.4.3.1 Calibration Results

Matching the observed discharge dynamics with the hydrologic model required calibration of two different melt factors based on time period: a lower value of 7.10 mm.w.e. (millimeters water equivalent) $^{\circ}C^{-1}$ day^{-1} over December 2015-February 2016; and a higher value of 8.64 mm.we.$^{\circ}C^{-1}$ day^{-1} over the rest of the simulation. The estimated melt factors fall within the range of melt factors calculated for other glaciers in the tropics (3.5-9.9 mm.we.$^{\circ}C^{-1}$ day^{-1}) reported in Fernández & Mark (2016). Our simulation period coincides with a strong El Niño event that generated the warmest and driest conditions from late November 2015 to the start of February 2016 (Figure 2.6a–b). The lower melt factor at this time dampens the intensity of glacier melt, possibly because of the absence of heat transfer from rain (Francou, 2004), but it nonetheless simulates among the highest glacier melt volumes of the simulation period (Figure 2.6a), consistent with other studies showing increased glacier melt in response to El Niño events in the Andes (Francou, 2004; Veettil et al., 2014a; Manciati et al., 2014; Maussion et al.,

2015; Veettil et al., 2016). Overall, in Gavilan Machay, the average specific glacier melt rate (in water equivalence) simulated over glaciated areas below the ELA was 1.5 m/yr. This falls within the range measured at the Reschreiter Glacier tongue, bracketed by mass balance estimates on slower-melting debris-covered ice of 0.87 m/yr (1997–2013) and 0.54 m/yr (June 2012–January 2013), and average ablation stake observations on faster-melting clean ice of 3.4 m/yr (June–November 2016). Although useful for comparing against the calibrated melt model, these measurements do not cover sufficient areas and periods of time to constrain separate melt factors for debris-covered and clean-ice melt factors.

Over the entire watershed, the resulting calibrated glacier melt production is equivalent to 68% of the precipitation input and 567% of the simulated snowmelt amount during the simulation period. Based on temperature, Flux-PIHM partitioned the precipitation input into 12% snowmelt and 88% rainfall. The much smaller amount of simulated snowmelt compared to glacier melt supports the earlier suggestion (Section 2.3.3) that snowmelt could be precipitation-limited rather than energy-limited. This helps justify our separate approach of simulating snowmelt through Flux-PIHM's energy balance module while simulating glacier melt through a calibrated temperature-index model, because energy balance calculations of glacier melt would be much more sensitive to uncertainties in coarse-scale radiation inputs than snowmelt. We do acknowledge, however, that snowmelt simulations depend on lapse-rate-determined precipitation inputs that have their own uncertainties (Section 2.3), and so our calibrated glacier melt may include some amount of snowmelt that is not represented in the model.

The calibration procedure also involved soil parameter adjustments. Hydraulic parameter estimates in páramo environments are scarce, and their characterization can be uncertain (Buytaert et al., 2006). For an initial estimate, we applied pedotransfer functions used in Flux-PIHM (Wosten et al., 1999) to a range of páramo soil measurements from a study area 20 km northwest of Chimborazo (3800 to 4200 m a.s.l.) (Podwojewski et al., 2002) and from a study watershed on glaciated Volcán Antisana also in the Ecuadorian Andes (4000-4600 m a.s.l.) (Minaya, 2016) (see Table A1 for full details).

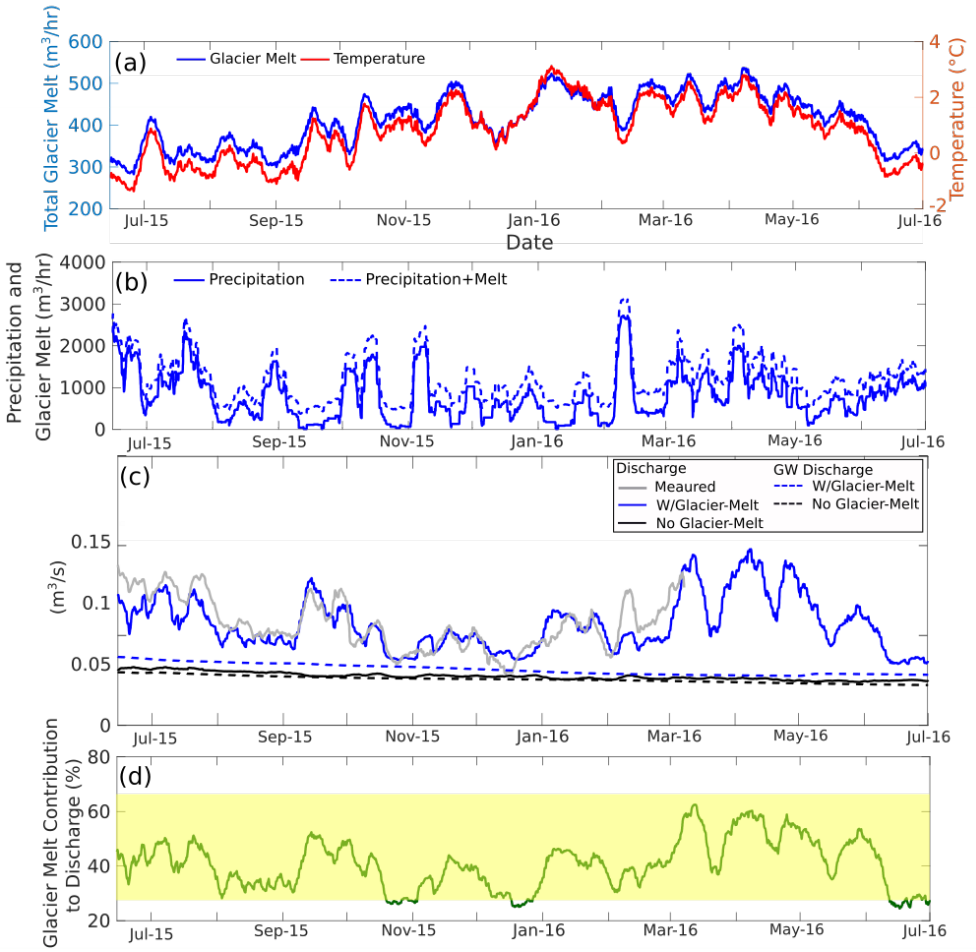

Figure 2.6: Time series of weekly moving average of (a) average air temperature over the ablation zone (glacier-covered areas below the ELA (5050 m a.s.l.)) and simulated glacier melt production; (b) precipitation (solid line), and precipitation+glacier melt (dashed lines) production (c) discharge at Gavilan Machay from observations (gray), calibrated simulations (blue solid), and simulations with no ice-melt (black solid); groundwater contribution to discharge for calibrated (blue dashed) and for no-ice simulations (black dashed); and (d) simulated percent glacier melt contribution to discharge at Gavilan Machay. The shaded block shows the range of percent melt contributions estimated for five sampling periods over 2012-2017 from the mixing model; these estimates may include snowmelt in addition to glacier melt, but omit meltwater contributions through groundwater.

We then calibrated the model for three mapped land-cover zones corresponding to páramo, rock/dirt/gravel, and ice (Figure 3.1). In the páramo zone (Table 2.1), matching observed discharge required lower hydraulic conductivity and greater water retention (expressed in van Genuchten hydraulic parameters) than initially estimated. This is likely due to high organic matter content supported by the study area's sub-humid conditions and the well-recognized retentive hydraulic properties of páramo soils (Podwojewski et al., 2002; Buytaert et al., 2006). In the sparsely vegetated and ice-covered zones, the calibration yielded higher hydraulic conductivities and lower water retentions than in the páramo zone, corresponding to reduced organic matter fraction and fractured bedrock, though the hydraulic conductivities were still lower than the initial estimates from the pedotransfer functions.

	KINF (m/s)	KSATV (m/s)	KSATH (m/s)	Porosity	Residual Moisture	α (1/m)	β (-)
Range predicted for observed páramo soil textures*	3.71E-8–8.28E-5	8.42E-8–3.71E-5	8.42E-7–6.96E-5	0.418–0.493	0.05	0.327–5.82	1.1–1.173
Calibrated: Grassland◇	1.23E-07	4.02E-08	4.02E-07	0.493	0.05	0.488	1.066
Calibrated: Sparsely vegetated◇	1.43E-07	4.63E-08	4.63E-07	0.459	0.05	0.585	1.063
Calibrated: Ice-covered◇	2.07E-07	4.56E-08	6.71E-07	0.461	0.05	0.863	1.06

*Predicted using pedotransfer functions with 9 páramo soil texture measurements from Ecuador. Samples are from 3 locations in a glaciated watershed in Volcan Antisana (Minaya, 2016) and 4 locations about 20 km northwest of Chimborazo (Podwojewski et al., 2002) (see Appendix A for more details). ◇Calibrated to match observed discharge at Gavilan Machay

Table 2.1: Soil hydraulic parameters calibrated for the three soil type areas compared against the range predicted using the pedotransfer function with measured páramo soil textures in Ecuador (Podwojewski et al., 2002; Minaya, 2016). Parameters include hydraulic conductivities for vertical infiltration (KINFV), vertical saturated zone flow (KSATV), and horizontal saturated zone flow (KSATH); porosity; residual soil moisture; and shape parameters (α and β) for the van Genuchten moisture retention curve: $S = \theta_{res} + porosity \times \left(\frac{1}{1+|\alpha\psi|^{\beta}}\right)^{(1-\frac{1}{\beta})}$, with saturation ratio of soil (S), residual water content θ_{res}, and pressure head ψ.

Simulation results in Figure 2.6c show that the calibrated model parameters closely produced the observed weekly discharge, including lower discharge under the drier and warmer El Niño conditions in December 2015-January 2016. The single major model mismatch occurred at a precipitation-driven discharge peak in February 2016. This could reflect uncertainties from the soil parameter calibration, as well as from our use of a lapse rate-based precipitation field over complex terrain, in which high-altitude

precipitation events may not all be recorded at the low-altitude rain gauge. On shorter timescales, hour-of-day simulation results in Figure 2.7b demonstrate that the model does produce a diurnal trend, but with slightly less than half the average range and at a 6-hour later peak compared to observations (Figure 2.7a). These hourly discrepancies can be attributed to weaknesses in the simple melt model. Hock (2005) argued that temperature index models can successfully capture seasonal glacier melt trends but struggle with diurnal fluctuations, which are strongly driven by solar radiation dynamics. Although our simulations cannot reliably produce the timing of hourly discharge, they can provide informative lower bounds on the size of the average diurnal range.

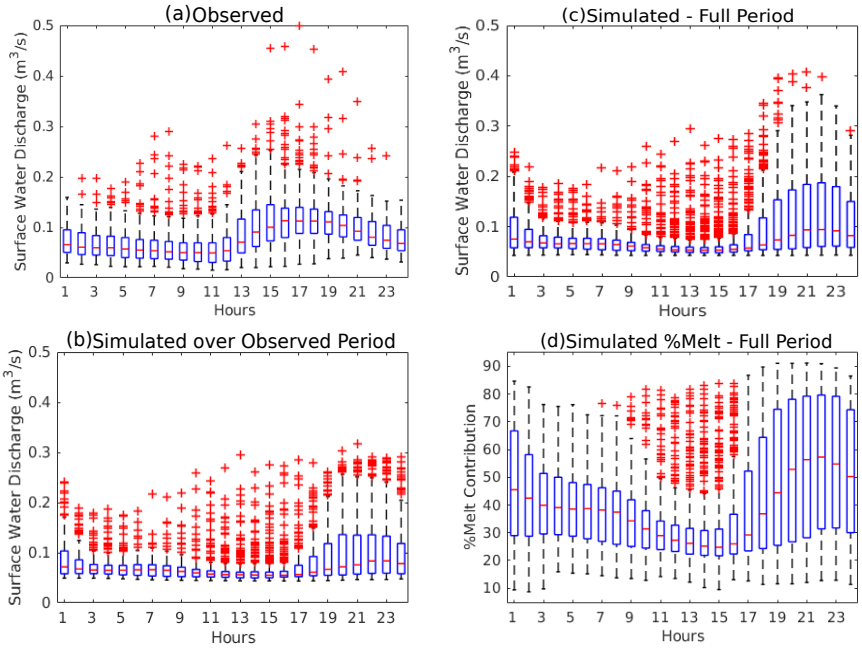

Figure 2.7: Box plots over local hour-of-day showing 25 – 75 percentiles with boxes and maximum and minimum with whiskers for (a) observed discharge over the 9-month observation period, (b) simulated discharge over the 9-month observation period, (c) simulated discharge over the 12-month simulation period, and (d) simulated percent glacier melt contribution to discharge over the 12-month period. Simulations do capture diurnal patterns, but with an underestimated magnitude and shifted peak. Simulated percent glacier melt contributions to discharge closely mirror the simulated diurnal fluctuations in discharge.

2.4.3.2 Simulations of relative glacier melt contribution to discharge

To quantify relative glacial meltwater contribution to stream discharge using Flux-PIHM, we compared the calibrated discharge simulations at Gavilan Machay (Q_{Calib}) with simulations that omitted glacier meltwater in the forcing inputs ($Q_{NoGlacierMelt}$). We then calculated relative glacial meltwater contribution to discharge via:

$$\% \text{ Glacier Melt} = \frac{Q_{Calib} - Q_{NoGlacierMelt}}{Q_{Calib}} \times 100\%. \tag{2.3}$$

Apart from the addition of glacier melt in the calibrated case, the two model scenarios include the same model inputs, including air temperature, precipitation (including identical snowmelt), land cover, and hydrologic properties. Thus, our calculation of change between the two scenarios isolates the effect of having glacier melt versus not having glacier melt. Overall, over the one-year simulation period, an average 50% of stream discharge in Gavilan Machay can be attributed to glacier melt, compared to an 8% contribution by snowmelt. Because the simulated glacier melt amount was calibrated in addition to precipitation inputs, we consider this glacier melt contribution to originate from the pre-existing ice reservoir at the start of the model period. However, as noted above (Section 2.4.3.1), the calibrated glacier melt contribution could include some amount of snowmelt not fully accounted for in the model due to uncertainties in precipitation inputs.

The estimate provided by equation (2.3) may not exactly correspond to the HBCM result for meltwater contribution for a number of reasons. First, the water balance impact of glacier melt conveyed in equation (2.3) may not equal the proportion of meltwater in a sample of discharge water if, for example, melt inputs facilitate more runoff of precipitation-sourced water. Also, while equation (2.3) aims to isolate glacier melt of pre-existing glacier ice, HBCM estimates could include snowmelt and melt of freshly accumulated ice, depending on the composition of the meltwater sample taken just below the glacier tongue. Lastly, any melt that infiltrates is considered as part of the groundwater rather than melt contribution in HBCM estimates, while equation (2.3) includes the effect of both surficial and groundwater contributions of meltwater to discharge.

These conceptual discrepancies complicate comparisons between the two methods,

but it is possible to assess the June 20-25, 2016 HBCM result against the simulation (other HBCM periods fall outside the one-year model period). During June 20-25, 2016, the 45-64% estimate with HBCM is higher than the average simulated relative melt contribution of 29%, but it falls within the simulated hourly range of 13-70% over that time. Considering that samples were collected during the daytime when melt contributions were generally high, the results from these two approaches reasonably agree.

While process-driven temporal patterns were difficult to glean from the sparsely spaced and uncertain HBCM results, Flux-PIHM simulations in Figure 2.6d indicate considerable variability in weekly glacier melt contributions of 25–61% over June 2015–June 2016. This range compares very closely with the 23–66% range bounded by the five HBCM estimates spanning January 2012 to February 2017 (indicated by the shading in Figure 2.6d), lending further confidence in the consistency between the watershed and mixing model results, despite the differences in temporal and other types of representation noted above. Hourly distributions of simulated glacier melt contribution in Figure 2.7d show an average diurnal range of 25-68%; given that the actual range is likely even broader due to underestimations by the temperature index model, diurnal fluctuations in relative melt contributions may be of similar or even greater magnitude than changes on weekly to monthly timescales.

Comparing Figures 2.6c and d reveals a remarkably strong correlation (0.89) between simulated weekly discharge and relative glacier melt contributions, indicating that major discharge peaks over multi-day timescales are melt-driven, a time-scale link that was masked in the time series analysis in Section 2.4.2 by the overwhelming diurnal signal between temperature and discharge. Figure 2.8b shows strong coherence over 30 to 80 day periods between simulated glacier melt production and relative glacier melt contributions to discharge, highlighting those timescales as the most prominent for direct glacier melt inputs beyond diurnal time scales. Although occurring at a longer multi-month timescale, these melt contributions to discharge nonetheless appear to happen mostly through fast surface runoff; the model showed most (86%) of the glacier melt contribution to discharge occurring through surface runoff processes, consistent with the hourly correlations found between observed discharge and temperature in Section 2.4.2. With the model, the influence of glacier melt production on discharge is clear

during times such as early January 2016, when an uptick in discharge occurs despite low precipitation, due to warm temperatures and greater melt production and contribution (Figure 2.6).

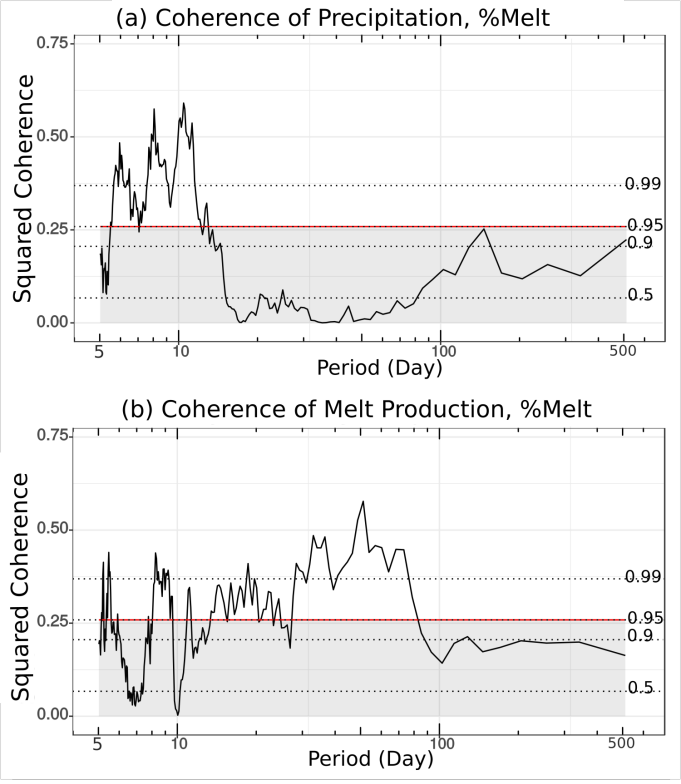

Figure 2.8: Magnitude squared coherences between simulated percent glacier melt contribution to discharge with (a) precipitation and (b) simulated glacier melt production. Calculations used daily average data to avoid known uncertainties in modeling diurnal fluctuations of glacier melt production. Precipitation and glacier melt production appear to be related to glacier melt contributions at complementary timescales.

Unexpectedly, the peak relative glacier melt contributions (Figure 2.6d) do not always align with glacier melt production patterns (Figure 2.6a) (e.g., in early February 2017, percent glacier melt contribution peaks just when temperature and glacier melt production dip), and their weekly correlation is not strong at a 95% confidence level (Figure A11b). Squared coherences in Figure 2.8a indicate that this is because relative glacier melt contribution also responds to precipitation, and this happens at weekly and multi-month timescales when correlations with glacier melt production are low (Figure

2.8b). In fact, the strong coherence between precipitation and glacier melt contribution around 6 to 14 day periods reveals that the high correlation between observed weekly precipitation and discharge in Section 4.3 may relate in part to glacier melt contributions. Inspection of time periods such as mid-February and the start of April 2016 show that rainy periods can augment glacier melt contributions to discharge (Figure 2.6b, d) . During those times, increases in relative glacier melt contributions to discharge coincided with precipitation events during local drops in glacier melt production, possibly because week-long precipitation creates antecedent moisture conditions that enhance the fraction of glacier meltwater that runs off over the surface. Surface runoff can be expected to contain mostly glacier meltwater or high-elevation precipitation, because runoff generally does not occur on low-elevation páramo soils except under intense precipitation (Sarmiento, 2000; Harden, 2004).

At greater timescales, significant coherences between precipitation and simulated relative glacier melt contributions around 120+ days (Figure 2.8a) correspond to overall lowest relative glacier melt contributions during the dry El Niño period (December 2015-February 2016) and highest relative contributions during the two wet seasons (February-May and October-November), possibly due to a transfer of heat from rain to ice. These glacier melt contribution responses to bi-seasonal to interannual climatic patterns likely occur through slower groundwater pathways; the simulation with glacier melt produces 18% greater groundwater contributions to discharge than that without glacier melt (Figure 2.6c). This supports the hypothesis that some amount of glacier meltwater infiltrates and recharges to groundwater that then discharges farther downgradient to the stream channel. It should be noted, however, that the subsurface component of Flux-PIHM contains only a single shallow saturated zone, which mostly closely corresponds to a perched water table in the soil zone. This model implementation may not accurately represent additional deeper fractured bedrock aquifers systems, which could discharge groundwater to streams over shorter, multi-month time scales (Andermann et al., 2012), in contrast to the relatively constant groundwater dynamics simulated in Figure 2.6c.

Our results may be particular to the moist climate in the Gavilan Machay watershed, which supports constant groundwater discharge to the stream throughout the year and reflects compounded effects of melt inputs and rainfall conditions. However, although glacier melt intensifies discharge variability in this watershed, a baseline 25% glacier melt

contribution throughout the simulation period indicates that a constant minimum level of glacier melt helps prevent episodes of even more extreme low flows during drought times, such as during El Niño conditions.

2.5 Summary and Conclusions

Although meltwater is typically credited with modulating stream discharge by buffering periods of low precipitation, we demonstrate using a combination of methods that relative meltwater contributions may drive nearly all the variability in discharge (correlation of 0.89) over a range of hourly to multi-year timescales while buffering only against extreme low discharge periods in a sub-humid glacierized watershed in the Ecuadorian Andes. Hydrochemical mixing model results for five sampling periods spanning 2012-2017 showed the meltwater fraction in discharge may have varied over approximately 20–65%. Hydrologic model simulations over June 2015–June 2016 produced a nearly identical range for weekly contributions. The model also predicted a very similar average diurnal range, which likely provided a lower bound of actual variability based on hydroclimatic data.

This multi-scale variability in melt contributions can be attributed to dynamic climate forcings that also contain a range of temporal patterns (Figure 2.9). We found a strong correlation between diurnal temperature and discharge changes that likely reflects melt production and supports the use of a temperature index melt model (Figure 2.9a). Although such a simple melt approach somewhat underestimated hourly fluctuation extremes with a lag, it led to reasonable weekly discharge predictions when implemented with a seasonally variable melt factor that possibly accounts for additional heat transfer from rainfall to ice during wet seasons. Spectral coherence analysis of the model results showed that not only were diurnal discharge patterns responding to melt production, but relative melt contribution and discharge variations over 30-80 day periods were controlled by extended glacier melt production periods that also contribute to discharge through surface runoff (Figure 2.9c).

Unexpectedly, model results showed that precipitation also boosted melt contributions to discharge, but on weekly and semi-annual timescales that complement the hourly and monthly timescales controlled by temperature and melt production. Weekly

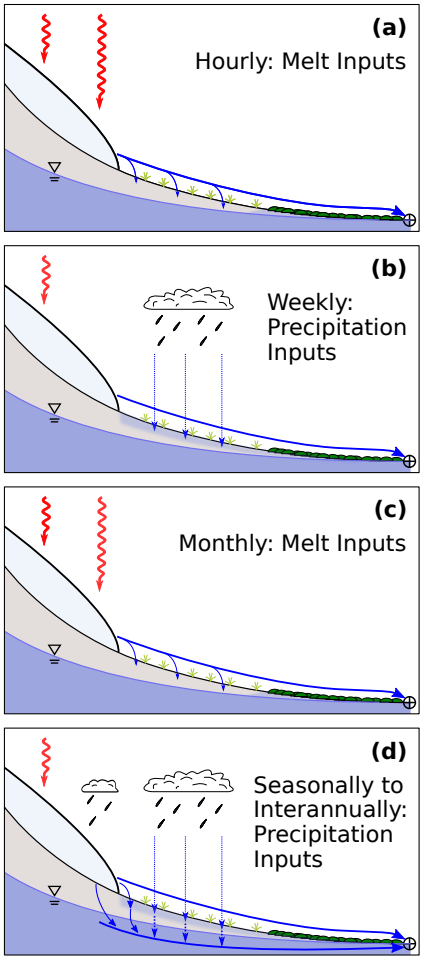

Figure 2.9: Relative melt contributions drive nearly all the variability in discharge in Gavilan Machay, mostly through surface runoff of glacial meltwater. What drives the variability in relative melt contributions to discharge? Our results show that this depends on the timescale. (a) Hourly timescale variability is controlled by radiation-driven (red arrows) melt production (light blue slab at upper left), which readily runs off overland (thick blue arrow) and eventually reaches the watershed's discharge point (circle with cross). (b) Weekly timescale variability is controlled by weekly precipitation events, which likely generate antecedent moisture conditions (light blue shading) that promote greater meltwater runoff. (c) Monthly timescale variability is driven by monthly trends in melt generation, which contributes to discharge mostly through surface runoff. (d) Seasonal to interannual variability is driven by long-term precipitation, which can enhance melt by transferring heat from rain (blue arrows right of glacier tongue), and augment subsurface melt contributions through increased groundwater flow (thick blue arrow below water table).

precipitation events likely generate antecedent wet conditions that facilitate greater amounts of meltwater runoff (Figure 2.9b), while longer-term precipitation patterns appear to drive slow changes in melt additions to groundwater (Figure 2.9d). Most (86%) melt contributions to discharge occurred through surface runoff in the model, but some meltwater recharged to groundwater, helping to support a relatively steady groundwater discharge to the stream that is about 18% greater with glacier melt than without glacier melt. As expected, strong El Niño conditions corresponded to some of the highest simulated melt inputs, but less easy to predict was that Gavilan Machay exhibited its lowest discharge during this time. Melt prevented streamflow from dropping below a baseline level during the warm and dry El Niño event, but discharge was much higher during wetter periods, in part because of the rainfall-enhanced melt contributions described above.

In glacierized watersheds, slower glacier melt contributions through groundwater are poorly constrained. Past studies have identified a component of meltwater in the groundwater (Favier et al., 2008; Lowry et al., 2010; Baraer et al., 2015; Minaya, 2016; Harrington et al., 2018), but to our knowledge, our work is the first to quantify this component. Generally, fractured young volcanic bedrock systems can support extensive groundwater (Tague et al., 2008; Markovich et al., 2016) and may contain similar meltwater fractions as found here. However, meltwater-groundwater interactions may be more ubiquitous. Prominent groundwater pathways have also been identified in fractured crystalline bedrock (Tague & Grant, 2009; Andermann et al., 2012; Pohl et al., 2015), morainic deposits (Favier et al., 2008; Minaya, 2016; Somers et al., 2016), and alpine meadow soils (Loheide et al., 2009; Lowry et al., 2010; Gordon et al., 2015). Even in settings with limited groundwater networks, talus slopes and rock glaciers can serve as localized areas of meltwater recharge (Clow et al., 2003; Baraer et al., 2015; Harrington et al., 2018). More arid settings than the sub-humid Gavilan Machay could have a higher proportion of glacier melt in groundwater due to less precipitation inputs, but our results also indicate that precipitation may serve to enhance meltwater contributions.

The multiscale temporal variability of relative melt contributions to discharge has important implications for how to determine the hydrologic role of glaciers in watersheds, as well as for water resource management in fast-changing glacierized systems.

Care must be taken in the implementation and interpretation of commonly employed tracer analyses. Potentially large diurnal fluctuations make it imperative to collect samples over consistent times of day, and weekly to interannual variability complicate extrapolations from single synoptic sampling estimates. Recharge by glacier melt further confounds the interpretation of groundwater as a source entirely distinct from surficial meltwater. These uncertainties, along with additional errors caused by heterogeneous groundwater chemistry and the choice of sample locations, limit the ability of tracer-based analyses to constrain dynamic melt contributions to discharge. Model simulations provide ideal temporal resolution, but they suffer from their own disadvantages, such as intensive data input requirements and uncertainties in parameter calibration.

For water resources, weekly to multi-year melt contributions to discharge are of greater interest than hourly fluctuations. At those timescales of concern, rain events and wet periods can accentuate relative melt contributions to streamflow in humid glacierized systems. This signifies a bonus in water yield, but it also intensifies discharge variability over weekly and seasonal timescales, which can pose challenges if water storage infrastructure is unavailable. On an interannual basis, melt can augment discharge during warm and dry El Niño events, but glacierized watersheds will likely experience greatest melt contributions during wetter times, when they are under the combined effects of enhanced ablation (due to transfer of heat from rain to ice) and antecedent moist conditions (due to precipitation). Looking at downstream implications, the small (7.5 km^2) Gavilan Machay headwater catchment contributes a range of only 9 to 26% of the discharge to the Boca Toma diversion point, which corresponds to surficial meltwater making up a range of just 4 to 15% of the water to the irrigation system, based on mixing model estimates. However, La Frenierre (2014) showed that farming communities cannot afford to lose any of the water; already, the irrigation system consistently fails to deliver its current allocations. Furthermore, if groundwater at Gavilan Machay also contains meltwater, as our simulations suggest, the actual total amount of meltwater contribution could be even higher than that estimated for surficial runoff of meltwater by the mixing model. Additional downstream monitoring would enable further extensions of the watershed model to investigate how meltwater contributions and temporal discharge variabilities found in Gavilan Machay propagate downgradient

to successively larger watersheds, as non-glacier sourced groundwater contributions increase. Spatial patterns of groundwater contributions within Gavilan Machay reveal sharp increases where geologic features likely create localized discharge points (Figure A12). This indicates that extrapolations downstream will likely depend on geological conditions that control groundwater, in addition to watershed size and climate inputs.

In the future, should Reschreiter Glacier disappear completely, overall discharge in Gavilan Machay could decrease by up to about 50%, even if precipitation and temperature remain the same and relatively constant groundwater flow continues. The exact decrease will depend on how much of our melt estimate may include contributions by snowmelt and melt from freshly accumulated ice that will persist as discharge sources. Overall, our findings suggest that in response to glacier loss in a warming climate, glacierized watersheds in the humid inner tropics may eventually experience steadier discharge, but potentially at significantly decreased rates.

Chapter 3

Spatiotemporal Drivers of Hydrochemical Variability in a Tropical Glacierized Watershed in the Andes

3.1 Introduction

The current retreat of glaciers is one of the most prominent signs of climate change (Stocker et al., 2013). By altering meltwater inputs to watersheds, this exerts a direct control on solute release and transport and influences global geochemical cycling. Tropical glaciers, 99% of which are located in the Andes, already experience year-round ablation (Vuille et al., 2008; Thompson et al., 2011; Huss & Hock, 2018), and they are now undergoing warming at a rate that is twice the global average (Bradley, 2006; Pepin et al., 2015), making them among the most vulnerable systems. However, despite the critical need for data on fast-changing high-elevation mountains (Bales et al., 2006; Barnhart et al., 2016), observations are very limited because of difficulties in access (Mulligan, 2013; Saberi et al., 2019). The resulting data gap urgently calls for extensive and multiple-approach investigations in order to assess the long-term alteration of water quantity and quality in these regions, possibly identifying early signs of thresholds and

tipping points of climate change. While various studies have begun to examine the hydrological impact of glacier retreat in the Andes (Barnett et al., 2005; Ostheimer et al., 2005a; Bradley, 2006; Mark & Mckenzie, 2007; Baraer et al., 2009; Saberi et al., 2019; Somers et al., 2019), little attention has been paid to its implications on geochemical cycling and solute export.

The majority of Andean mountains are located within the Andean volcanic belt (Stern, 2004) and are mainly composed of reactive silicate minerals (Stallard & Edmond, 1983; Ugolini et al., 2002) that weather faster with greater topographic gradients (Torres et al., 2015; Wymore et al., 2017b). Under humid tropical conditions, weathering rates are further accelerated by high temperature and moisture (Ugolini et al., 2002; White et al., 1998). This makes tropical Andean mountains important hotspot sources of solutes, including sodium (Na^{+}), calcium (Ca^{2+}), and magnesium (Mg^{2+}), that support ecological productivity in the Amazon basin (Gibss, 1967; McClain & Naiman, 2008; Moquet et al., 2018; Wymore et al., 2017b), even though they are located thousands of kilometers away from the Amazon river estuary and constitute only about 13% of the basin. Transport of these weathering products off of montane slopes with stream discharge is facilitated by the steep topographic gradients in these watersheds (Dessert et al., 2005; Hartmann et al., 2009; Lloret et al., 2013). Andean tributaries contribute about 50% of the streamflow in the main stem of the Amazon River (Dunne et al., 1998), supplying 82% of the total suspended solids exported by the Amazon River (Gibss, 1967), and presumably also a significant amount of dissolved solids.

Although the tropical Andes are important for the Amazon basin ecosystem, which in turn is a major contributor to global chemical cycling, the role of glacierized tropical mountain watersheds are understudied and poorly characterized (Schlesinger & Bernhardt, 2013). Glaciers cover only 1% of the area of the Andes, but they increase rates of physical erosion, which promotes more rapid silicate mineral weathering by exposing fresh rocks that contain silicates (Torres et al., 2017). Further, meltwater can contribute significantly to streamflow, which additionally facilitates solute export from glacierized slopes (Torres et al., 2017). Quantifying the role of tropical glacierized watersheds to regional solute export is critical because of the fast-changing conditions in these watersheds. This requires an understanding of the factors that control stream chemistry and the effects of changing climate on weathering and solute export in tropical glacierized

watersheds.

Most of our understanding about hydrochemical controls in glacierized mountainous watersheds has come from temperate climates. These controls include meteorological drivers and meltwater contribution to the stream (Brown, 2002; Anderson, 2005; Hindshaw et al., 2011; Lewis et al., 2012; Stachnik et al., 2016; Milner et al., 2017; Kumar et al., 2019; Engel et al., 2019), bedrock and surficial geology (Tranter et al., 1996; Katsuyama et al., 2010; Engel et al., 2019), mixing of water from different flow pathways (Farvolden, 1963; McGuire et al., 2005; Tetzlaff et al., 2009; Maher, 2011; Benettin et al., 2015), and land-cover over different spatial and temporal scales (Williams et al., 2015). Various studies in temperate glacierized watersheds found that solute concentrations are lower during high melt seasons due to the discharge of dilute meltwater into streams (Collins, 1999; Brown, 2002; Hindshaw et al., 2011; Kumar et al., 2019; Engel et al., 2019). However, others found that in-stream silica (SiO_2) (Anderson, 2005) and other major ion concentrations (Lewis et al., 2012; Stachnik et al., 2016) increase during high melt seasons, mainly due to the increase in the hydrological connectivity of the catchment, which accelerates mineral dissolution. In general, the potential for solute concentrations in streams to stay the same (chemostatic) or vary (non-chemostatic) with changes in stream discharge has been found to depend on water transit times through the subsurface (Heidbüchel et al., 2013; Benettin et al., 2015), lithology (Bluth & Kump, 1994; Katsuyama et al., 2010; Ibarra et al., 2016), vertical heterogeneity of weathering fronts (Winnick et al., 2017; Kim et al., 2017), and availability of reactive mineral surface area (Maher & Chamberlain, 2014; West, 2012).

Recently, some hydrochemical studies have focused on tropical montane watersheds, nearly all non-glacierized, and have found factors driving solute concentrations and export to include catchment slope as a proxy for erosion and fluid flow (Torres et al., 2015; Wymore et al., 2017b), geological and climatic heterogeneity within the watershed (Torres et al., 2017; Baronas et al., 2017), and landscape characteristics such as vegetation type (Wymore et al., 2017b; Molina et al., 2019). One study that did consider a glacierized tropical watershed found enhanced weathering due to exposure of fresh bedrock by glacier retreat (Fortner et al., 2011). The lack of other tropical glacier hydrochemical studies represents a major knowledge gap about highly vulnerable systems that may have important controls on critical downstream ecosystems.

It is important noting that most of the findings in tropical mountain watersheds resulted from comparing several watersheds rather than directly examining processes within a watershed (Torres et al., 2015, 2017; Baronas et al., 2017; Wymore et al., 2017b). In fact, regardless of climate and glacier cover, many hydrochemical studies rely on stream outlet concentration (C) and discharge (Q) relationship analysis to indirectly infer processes within the watershed that control stream chemistry and export (e.g., Godsey et al. (2009); Maher (2011); Kirchner & Neal (2013); Benettin et al. (2015); Wymore et al. (2017b)). Watershed processes control whether C of non-reactive and weathering-derived solutes change with Q (Shanley et al., 2011; Stallard et al., 2014) or if they remain relatively time-invariant (chemostatic) (Johnson et al., 1969; Hem, 1985; Godsey et al., 2009; Li et al., 2017b). C and Q at the outlet thus serve as important integrated metrics for constraining dynamic conditions within the watershed, but C-Q analysis alone cannot directly represent the different processes. Due to the lack of explicit, fine-scale process resolution in C-Q analysis, uncertainties persist in describing spatiotemporal hydrologic and geochemical processes that control C-Q behavior (Li et al., 2017b; Wymore et al., 2017a; Zhi et al., 2019).

The uncertainties about detailed watershed controls pose a particularly major obstacle to predicting nutrient and solute export from tropical glacierized mountains under rapid warming. Because tropical glaciers undergo year-round ablation, spatially variable conditions and multiple resolution dynamics within the watershed can be expected to play an important role in modulating hydrochemistry in the absence of a dominant seasonal signal. The influence of some spatiotemporally variable factors will be especially critical to understand, because they are themselves susceptible to rising temperatures. Most obviously, glacier cover will shrink, altering melt contributions to discharge and possibly weathering rates, both of which impact solute concentrations at the stream outlet (Lewis et al., 2012; Stachnik et al., 2016). Additionally, recent studies have documented upslope migration of montane vegetation with warming, with one tropical glacierized watershed exhibiting greater shifts per temperature increase than the global average (Morueta-Holme et al., 2015). Observed relationships between vegetation cover and C-Q behavior (e.g., Williams et al. (2015); Wymore et al. (2017b); Molina et al. (2019)) suggest that changing vegetation distributions within tropical glacierized watersheds could influence hydrochemical conditions. Finally, a number of studies in

tropical glacierized watersheds have found groundwater to contribute a notable fraction of streamflow (Favier et al., 2008; Baraer et al., 2015; Minaya, 2016; Saberi et al., 2019). Given the role of subsurface flow paths and residence times in determining C-Q behavior (Farvolden, 1963; McGuire et al., 2005; Tetzlaff et al., 2009; Maher, 2011; Benettin et al., 2015), constraining interactions among groundwater flow, meltwater inputs, vegetation cover, and mineral reactions will be essential for quantifying solute export in tropical glacierized watersheds.

A recently developed, spatially distributed and physically based model that integrates watershed hydrology and reactive transport, BioRT-Flux-PIHM (Bao et al., 2017; Zhi et al., 2020), is now making it possible to directly evaluate spatiotemporal controls on watershed hydrochemistry (Li et al., 2017b; Zhi et al., 2019). Importantly, this enables detailed hydrochemical analysis without exhaustive measurements that would be difficult to obtain in remote locations such as tropical glaciers. Reactive transport models, including Crunchflow (Steefel & Maher, 2009), HyTech (Van Der Lee et al., 2003), and PHT3D (Prommer et al., 2003), integrate flow, solute transport, and biogeochemical reactions to help us probe biogeochemical processes across scales (Steefel et al., 2015). Even though solute and water quality models have been developed as add-on modules to hydrological models (see reviews by Steefel et al. (2015)), a physics-based model that couples hydrological, land-surface, and geochemical processes has been lacking before the development of BioRT-Flux-PIHM (Li et al., 2017a). Recent applications of the BioRT-Flux-PIHM model at two intensively studied watersheds in the temperate U.S. revealed strong seasonal controls through both hydrologic (surface and subsurface) and geochemical processes across the watershed (Li et al., 2017b; Zhi et al., 2019; Wen et al., 2020). These early applications are paving the way for new questions, such as how other types of climatic patterns (e.g., warmer and wetter tropical conditions with additional snow and ice melt contributions), lithologies (e.g., silicate-dominated volcanic soils underlain by fractured bedrock), and vegetation coverage (e.g., vegetation line threshold in high mountain watersheds) might shape C-Q dynamics of solutes that affect critical downstream ecosystems.

In this study, we leverage BioRT-Flux-PIHM to answer the overarching question of what spatiotemporal processes, including hydrological and geochemical, control the dynamic export of solutes (specifically Na^{+}, Ca^{2+}, and Mg^{2+}) from a tropical glacierized

watershed. In particular, we investigate the interactions and relative roles of the following factors within a study watershed on Volcán Chimborazo in the Ecuadorian Andes: (1) subsurface processes, including silicate weathering and groundwater flow; (2) heterogeneous vegetation coverage on the montane slopes; and (3) year-round glacier melt inputs to the upper watershed. Insights on these processes will provide the baseline understanding needed to make future predictions of solute export under rapidly changing climate conditions, which may have important downstream ecological implications as glaciers retreat.

3.2 Study Site Description

Volcán Chimborazo is a glacierized stratovolcano in Ecuador that supplies water to over 200,000 people (INEC, 2010). Chimborazo experiences an inner tropical climate, characterized by minimal annual temperature variation (∼2 °C variability), and moderately seasonal precipitation with generally two wetter seasons (February-May and October-November) and two drier seasons – though precipitation falls year-round (Clapperton, 1990). Because of the Amazon Basin to the east (Vuille & Keimig, 2004; Smith et al., 2008b), more humid conditions occur on the northeast flank with more precipitation (∼2000 mm/yr) than the southwest (∼500 mm/yr) (Clapperton, 1990). Within the June 2015 to June 2016 time frame of this study, two wetter periods (June - October and February - May) and a dry period (November - January) were observed on Chimborazo due to the influence of an El Niño event. El Niño and La Niña events cause variability in temperature and precipitation, with El Niño generally bringing drier and warmer conditions and La Niña wetter and cooler conditions throughout the Andes (Vuille & Bradley, 2000; Wagnon et al., 2001; Francou, 2004; Smith et al., 2008b). During June 2015-June 2016, a strong El Niño event brought higher temperature, less cloud cover, and below-normal precipitation during November through January. El Niño events have been found to potentially enhance glacier ablation (Wagnon et al., 2001; Francou, 2004; Favier, 2004; Vuille et al., 2008; Veettil et al., 2014a).

Weather stations near the base of Chimborazo, around 2600-3300 masl, show a temperature increase of 0.11 °C /decade over 1986-2011 (Vuille et al., 2008; La Frenierre & Mark, 2017), despite a strong Niña event during 2007-2009, which generally brings

cooler temperatures. Warming rates may be greater at higher glacierized elevations on Chimborazo, considering altitude-dependent warming trends observed in the tropical Andes (Bradley, 2006). This warming has been partially responsible for a 21% reduction in ice surface area and 180 m increase in the mean minimum elevation of clean ice from 1986 to 2013 (La Frenierre & Mark, 2017). Though instrumental data are ambiguous, community members indicate that the local precipitation has also decreased in recent decades (La Frenierre & Mark, 2017). This study focuses on the 7.5 km^2 Gavilan Machay sub-catchment on the sub-humid northeast flank of Chimborazo. Gavilan Machay has an altitude range of 3800 to 6400 m a.s.l. and is 34% glacierized by the Reschreiter Glacier. Water from Gavilan Machay eventually reaches the Amazon below the confluence of Río Maranon, the principal upper tributary of the Amazon River, via the Río Mocha, Río Ambato, Río Chambo, and Río Pastaza. Gavilan Machay is of particular concern because it discharges into the Río Mocha channel immediately upstream of the Boca Toma diversion point (3895 m a.s.l. elevation) for the largest irrigation system on Volcán Chimborazo. Saberi et al. (2019) found that currently, stream discharge from Gavilan Machay may contain up to 50% glacier meltwater, which has significant implications for the downstream irrigation system as the glaciers continue to retreat.

Páramo – the biologically rich grassland ecosystem of the tropical Andes – occupies the watershed below about 4600 m a.s.l. (Figure 3.1a). Páramos have high plant diversity (>5000 species), mainly consisting of tussock grasses, cushion plants, dwarf shrubs, ground rosettes, and giant rosettes. Wet páramos, what is found in Gavilan Machay, are mainly composed of Andosol soils of volcanic origin and have high porosity and water retention capacity (Podwojewski et al., 2002; Buytaert et al., 2006; Buytaert & Beven, 2011; Minaya, 2016). The primary geology of Chimborazo consists of layered lava and pyroclastic flows, overlaid by thick ash deposits and vitric Andosol (Figure 3.1b) (Barba et al., 2008; Samaniego et al., 2012). The geomorphology of the watershed has been influenced largely by glacial deposits and moraines from the Last Glacial Maximum (LGM: 33-14 ka), the Late Glacial (LG: 13-15 ka), and the Neo-Glacial Period (NG: <5 ka). The presence of young volcanic fractured bedrock along with páramo soils and glacial deposits (Barba et al., 2005; Samaniego et al., 2012) facilitates water movement through the subsurface, which enhances both groundwater contribution to streamflow and weathering processes that release ions into the water (Stallard & Edmond, 1983).

Previous hydrochemical observations in the Gavilan Machay watershed by Saberi et al. (2019) found Na^{+}, Ca^{2+}, and Mg^{2+} to be the major ions present in the groundwater and stream water. That previous study used hydrochemical data in a mixing model to help partition hydrological inputs to streamflow in Gavilan Machay, but little is known about the processes controlling different solute concentrations throughout the watershed and the export of solutes at the outlet.

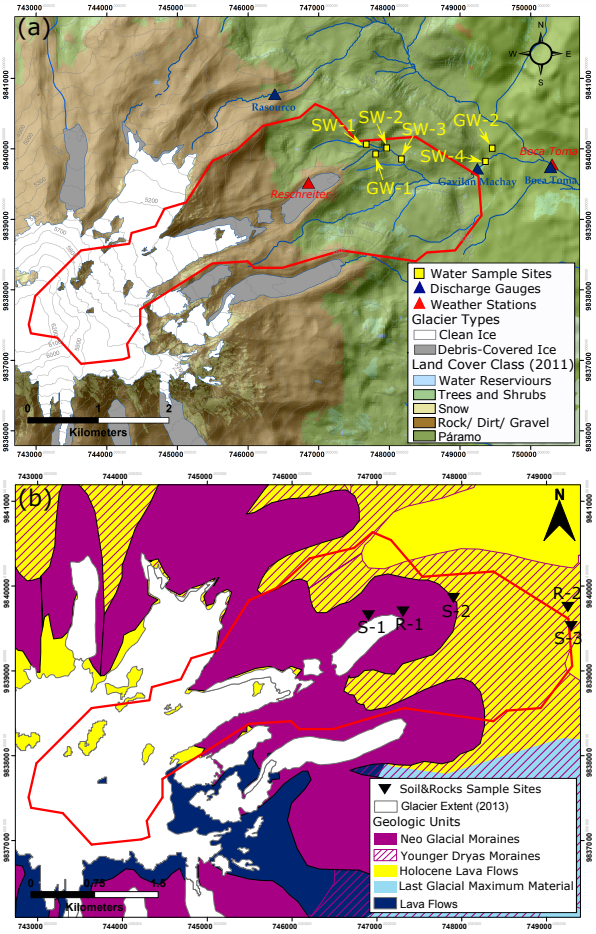

Figure 3.1: (a) Land cover and locations of monitoring stations and water sampling within the Gavilan Machay watershed. (b) Geologic map of Volcán Chimborazo and locations of soil and rock sampling within the Gavilan Machay watershed. The boundary of the Gavilan Machay watershed is outlined in red. Maps were adapted from McLaughlin (2017).

3.3 Geochemical Observations

3.3.1 Sites and Sampling Method

Three locations were selected for soil sampling along an elevation gradient (4510, 4240, and 3990 m a.s.l.) (Figure 3.1b). The highest elevation sample (S-1) was collected from moraine sediments, and the other two (S-2 and S-3) were taken near the stream channel (Figure 3.1b). A 3-inch diameter auger was used for soil profile sampling. At all sampling sites, shallow refusal was hit on buried cobbles, and a single sample was collected from about 4 cm (below the thickest roots) to the depth of shallow refusal on buried cobbles (S-1: 15 cm, S-2: 25 cm, and S-3: 12 cm). Two rock samples were collected at exposed outcrops, at 4950 m a.s.l. and 4000 m a.s.l. (R-1 and R-2, respectively, in Figure 3.1b). The high elevation rock sample (R-1) was collected from Guano lava flows, and the low elevation rock sample was collected from Holocene pyroclastic flow deposits (based on the geologic map by Barba et al. (2008)).

As described in Saberi et al. (2019), we carried out two water sampling campaigns during June 2015 and June 2016. These campaigns took place before and after a warm and dry El Niño event from November 2015 through January 2016. During each campaign, we collected 16 water samples from glacier meltwater, precipitation, four locations along the stream (SW-1 to SW-4), and two springs as a proxy for groundwater (GW-1 and GW-2) (Figure 3.1a). Here, we define groundwater as an unconstrained mix of water from shallow saturated soil and two inferred aquifer units: a morainic debris aquifer and a deeper fractured bedrock aquifer. In each field campaign, we collected one sample per location, as challenging field conditions prevented the collection of replicates. For each sampling site, 30 mL of water were collected, filtered in the field using 0.45 μm filters, and stored in Nalgene bottles that were capped and sealed with electrical tape, and stored near 4 °C. Cations (Na^+, K^+, Mg^{2+}, Ca^{2+}) were measured using an Agilent 7700X Inductively Coupled Plasma-Mass Spectrometer (ICP-MS) and anions (F^-, Cl^-, SO_4^{2-}) were measured using a Dionex ICS1000 Ion Chromatographer (IC) at Gustavus Adolphus College. Stream discharge was measured in the watershed using a discharge gauging station equipped with a Solinst Levelogger Junior pressure transducer from June 2015 to May 2016. Saberi et al. (2019) utilized water chemistry observations

to investigate hydrological inputs to streamflow but did not investigate geochemical processes controlling water chemistry.

3.3.2 XRD Analysis and Results

Soil samples were air-dried and stored in resealable bags. Bulk soil and rock composition was determined using X-ray diffraction (XRD) analysis. For sample preparation, aggregate soil and rock samples were each hand-ground to a fine powder. Organic matter was removed from the samples by the addition of a 3% hydrogen peroxide (H_2O_2) solution following Poppe et al. (2001). Samples were mounted on a glass slide using a smear technique to achieve random orientation. A Rigaku MiniFlex300 X-ray diffractometer was used to scan the samples from 5° to 65° 2θ at 30 kV voltage and 10 mA current with Cr-Kα radiation. XRD patterns were analysed using the Jade software version 7.5.

Results from the XRD analysis indicate that the Gavilan Machay watershed is predominantly composed of aluminosilicate minerals including feldspars, pyroxenes, and amphiboles, which is consistent with most Andosols worldwide (Shoji et al., 1994). Further, XRD analysis of soil samples from different depths suggest that vertically, mineral composition is relatively homogeneous (Appendix B, Section B2, Table B1). Although the humid conditions in Gavilan Machay would generally be expected to promote high rates of weathering that could lead to clay formation, XRD results show no crystalline-clay minerals, and PHREEQC (Parkhurst et al., 1999) equilibrium calculations using observed aluminum and silica concentrations indicate that the groundwater is under-saturated with respect to various crystalline-clay minerals (kaolinite, gibbsite, and halloysite) (Appendix B, Section B3, Table B2). The apparent absence of crystalline clay minerals suggests that they have not yet formed within the young, high-elevation volcanic soils of Volcán Chimborazo, and fine sediments detected in soil samples may instead consist of organo-mineral clays, similar to that previously found on Chimborazo by Bartoli et al. (2007). More details on XRD and grain size analysis can be found in Appendix B (Section B2).

The XRD analysis indicates that the bulk soil mineralogy is primarily dominated by that of the parent bedrock (Table 3.1), with soil sample S-1 resembling the nearby rock sample R-1 based on the presence of andesine, and soil samples S-2 and S-3 resembling the nearby rock sample R-2 based on the presence of albite (see locations in Figure

3.1b). Throughout the watershed, all samples comprised similar classes of minerals (feldspars and pyroxenes), suggesting that the surficial sediments and deeper bedrock aquifers throughout the watershed may share similar geochemical signatures.

	Mineral	Chemical Formula	R-1	S-1	R-2	S-2	S-3
Feldspar	Albite	$Na(AlSi_3O_8)$			✓	✓	✓
	Anorthite	$Ca(Al_2Si_2O_8)$	✓	✓	✓		✓
	Andesine	$Na_{0.685}Ca_{0.347}Al_{1.46}Si_{2.54}O_8$	✓	✓			
	Labradorite	$Na_{0.45}Ca_{0.55}Al_{1.5}Si_{2.5}O_8$		✓			
	Sanidine	$K(Si_3Al)O_8$	✓				✓
	Anorthoclase	$(Na_{0.75}K_{0.25})(AlSi_3O_8)$	✓		✓	✓	✓
Pyroxene	Enstatite ferroan	$Mg_{1.1}Fe_{0.87}Ca_{0.03}Si_2O_6$	✓	✓	✓		
	Diopside	$Ca(Mg,Al)(Si,Al)_2O_6$	✓		✓		✓
Amphibole	Arfvedsonite	$Na_3(Fe,Mg)_4FeSi_8O_{22}(F,OH)_2$	✓				
	Actinolite	$(Fe,Mg,Ca,Na,Mn)_7(Si,Al)_8O_{22}(OH)_{1.9}$	✓				

Table 3.1: XRD Mineral Analysis. S-1, S-2, and S-3 are soil samples. R-1 and R-2 are rock samples from outcrops in the watershed. Sample locations are shown in Figure 3.1b.

3.4 Model Description

3.4.1 BioRT-Flux-PIHM

Spatially distributed watershed models can integrate surface hydrology and groundwater flow through time and space to allow for the evaluation of their joint control on streamflow. Flux-PIHM (Shi et al., 2013) integrates land-surface and hydrologic simulations through a combination of two modules, the Noah land surface model (Noah-LSM) (Ek et al., 2003) and the PIHM hydrological model (Qu & Duffy, 2007). The multicomponent reactive transport module BioRT (previously called in "RT" in earlier publications) is an add-on to Flux-PIHM (Bao et al., 2017). Flux-PIHM employs a semi-discrete finite volume approach on an unstructured grid that performs efficiently on steep topographies. Channel and overland flow in the model are represented by diffusion wave approximations to St. Venant equations, vertical unsaturated zone flow is estimated using a 1D form of Richards equation, and horizontal and vertical shallow groundwater flow follows Darcy's law. For each grid cell, the model tracks water storage

in one vertically integrated unsaturated zone layer and one vertically integrated saturated zone layer, providing a "2.5D" distributed model. Full details about Flux-PIHM can be found in Qu & Duffy (2007) and Shi et al. (2013).

The BioRT module takes calculated water fluxes and storage from Flux-PIHM (i.e. surface runoff, channel routing, infiltration, recharge, and subsurface lateral flow) and simulates hydrochemical processes including solute transport (advection, dispersion, and diffusion) and biogeochemical reactions and outputs aqueous and solid phase geochemical concentrations. In addition to surface and subsurface water flow, evapotranspiration (ET) is simulated in the model as another key hydrologic flux that has a non-geochemical influence on solute concentrations. BioRT can simulate both equilibrium-controlled reactions, including aqueous complexation, ion exchange, and surface complexation, as well as kinetically controlled reactions, including mineral dissolution, precipitation, and redox reactions (Bao et al., 2017). Though not used in this study, the most recent addition to the BioRT module has been biologically mediated reactions, including plant uptake of nutrients, and microbially mediated reactions such as soil respiration and denitrification (Zhi et al., 2020). Reactive transport is modeled in both the unsaturated and saturated zones. It is assumed that the surface runoff water has a short interaction time with minerals and is not considered to undergo geochemical reactions in the BioRT module.

The rate of kinetically controlled mineral dissolution and precipitation is calculated using a transition state theory (TST)-style rate law (Helgeson et al., 1984; Lasaga, 1984):

$$R_m = A_{w,m} k_m (1 - \frac{IAP}{K_{eq}}) \tag{3.1}$$

where R_m is the dissolution rate of the mineral m (mol/s) (or precipitation rate when negative), $A_{w,m}$ is the wetted surface area of mineral m (m^2), k_m is the intrinsic rate constant (mol/(m^2/s)), IAP is the ion activity product, and K_{eq} is the thermodynamic equilibrium constant. BioRT-Flux-PIHM simulates the influence of temperature on kinetic reactions through the following equation for k_m:

$$ln(k_m) = ln(k_{mref}) - \frac{E_a}{R}\left(\frac{1}{T} - \frac{1}{T_{ref}}\right) \tag{3.2}$$

where k_{mref} is the rate constant (mol/(m^2/s)) for mineral m at the reference temperature T_{ref} (298.15K in BioRT-Flux-PIHM), E_a is the activation energy (J/mol), R is

the gas constant (J/mol/K), and T is the soil temperature (K). The wetted surface area depends on groundwater storage through the following equation (Clow & Mast, 2010):

$$A_{w,m} = A_m S_w^n \tag{3.3}$$

where A_m is the total surface area of the mineral m under fully saturated conditions (m^2), S_w is the water saturation (m^3 water per m^3 pore space), and n equals 2/3 to represent the surface area to volume ratio of mineral grains (Mayer et al., 2002). Total surface area of each mineral is estimated using the following equation:

$$A_m = SSA \times (F_m \times V_i) \times D \tag{3.4}$$

where SSA is the specific surface area of the mineral (m^2/g), F_m is the volume fraction

of the mineral m (m^3/m^3), V_i is the total volume of grid cell i (m^3), and D is the solid density (g/m^3). The BioRT module and Flux-PIHM are coupled through the dependence of the wetted surface area ($A_{w,m}$) on soil moisture and groundwater availability.

We assume that groundwater boundaries align with the surface watershed boundary, such that water and solutes do not enter the watershed via regional groundwater, which is typical for headwater watersheds (Dingman, 2015). Another simplification is that this version of the model represents lateral "groundwater" flow as the combination of shallow soil water interflow and deeper groundwater flow. Further, all groundwater is eventually routed laterally into the stream and exits the watershed as surface discharge.

The governing equation for reactive transport of an arbitrary solute m is as follows:

$$V_i \frac{d(S_{w,i}\theta_i C_{m,i})}{dt} = \sum_{j=N_{i,1}}^{N_{i,x}} \left(A_{ij} D_{ij} \frac{C_{m,j} - C_{m,i}}{I_{ij}} - q_{ij} C_{m,j} \right) + S_{m,i} \qquad m = 1, ..., np \tag{3.5}$$

where V_i is the total volume of grid cell i, $S_{w,i}$ is the water saturation (m^3 water per m^3 pore space), θ_i is the porosity (m^3 pore space per m^3 total volume), $C_{m,i}$ is the aqueous concentration of species m (mol/m^3 water); $N_{i,x}$ is the index of the neighboring elements of grid cell i, with the subscript x is set to two for unsaturated zone fluxes (infiltration and recharge) and four for saturated zone fluxes (recharge and lateral flow to the three

neighboring cells), respectively; A_{ij} is the interface area between the grid cell i and its neighbor cell j (m^2); D_{ij} is the dispersion plus diffusion coefficient (m^2/s); I_{ij} is the distance between the center of the neighboring grid cells; q_{ij} is the volumetric flow rate across A_{ij} (m^3/s); $S_{m,i}$ is the additional source or sink, and np is the total number of independent solutes.

Full details about BioRT-Flux-PIHM can be found in Qu & Duffy (2007); Shi et al. (2013); Bao et al. (2017), and Zhi et al. (2020).

3.4.2 Model Setup

3.4.2.1 Hydrological and Transport Processes

The BioRT-Flux-PIHM version 0.10.0 alpha was applied from June 2015 - June 2016. BioRT-Flux-PIHM takes inputs including land cover, hydraulic properties, and climate forcing, in addition to major ion concentrations in precipitation for all times, and in groundwater at initial time. Precipitation, temperature, and relative humidity were measured in the watershed from June 2015 - June 2016 (Figure 3.1a), while other meteorological variables including wind speed, shortwave radiation, longwave radiation, and air pressure were obtained from the Global Land Data Assimilation Systems (GLDAS) database (Rodell et al., 2004). Built-in land cover parameters from Noah-LSM were used for each land-cover type. Leaf area index for the vegetated parts of the watershed were from MODIS (Vermote, 2015). Land-cover was set as grassland at the lowest elevations to represent páramo, barren ground for the mid-altitude, and perennial ice/snow for the ice-covered areas based on the vegetation and land cover mapping by McLaughlin (2017) (Figure 3.1a). We used the PIHMgis software (Bhatt et al., 2014) to discretize the domain into 188 triangular cells using a 30 m resolution Shuttle Radar Topography Mission (SRTM) Digital Elevation Model (DEM) (Farr et al., 2007). To include ice melt in the simulation, a separate temperature-index module was added to the model. Glacial melt was estimated under the assumption that ablation occurs over the glacierized grid cells below the equilibrium line altitude (ELA) at 5050 m a.s.l. (determined using data from La Frenierre (2014)). Further details on the glacier melt rate simulations can be found in Saberi et al. (2019).

3.4.2.2 Geochemical Processes

The RT module was implemented with equilibrium aqueous complexation reactions for major elements (Na^+, Ca^{2+}, Mg^{2+}, and SiO_2) and pH, and with kinetic reactions for the minerals described below. Chloride (Cl^-) was included as a non-reactive tracer. Aqueous chemistry measurements were used to constrain mineral dissolution kinetic and soil hydraulic parameters. Time-averaged chemical concentrations at the GW-1 and GW-2 spring sampling points (Figure 3.1a) were used to establish two different initial groundwater geochemical conditions for the spin-up run, one for the vegetated portion of the watershed and the other for the barren and ice-covered portions of the watershed (Table 3.2). The model was run in a spin-up mode until aqueous species reached a steady state such that their concentrations did not change with time. Due to the approximate nature of the spin-up, averaged steady-state concentrations in groundwater in the vegetated cells and in the barren and ice-covered cells were used as spatially uniform initial conditions for these respective portions of the watershed in the final simulation. As shown in Table 3.2, the measured and initial concentrations were higher in vegetated areas (with páramo, at lower elevations) (Figure 3.1a). Although glacier melt samples had slightly higher concentrations than precipitation samples, they were of similar orders of magnitude that were much lower than that of the groundwater and streamwater samples. This supported the use of the same geochemical composition (that measured for precipitation) for both precipitation and glacial melt in the model in order to simplify the implementation with only one forcing condition for the two types of inputs. Precipitation and glacier melt concentrations were assumed to be constant over space and time.

3.4.2.2.1 Non-reactive Transport of Chloride

With the absence of chloride-containing minerals in the XRD results, we used Cl^- as a non-reactive tracer, which we assume enters the watershed through wet atmospheric deposition and glacial melt inputs. The higher Cl^- concentrations in the groundwater relative to precipitation (Table 3.2) likely occurs due to the concentrating effect of ET. Because this process occurs in the absence of geochemical reactions, we used Cl^- as a tracer to evaluate the hydrological processes controlling the spatio-temporal variability

	Precipitation	Glacial Melt	Páramo (Observed)	Páramo (Initial Condition)	Barren and Ice-covered (observed)	Barren and Ice-covered (initial condition)
Elemental Species (μmol/l except for pH)						
pH	6.3	5.76	5.64	5.5	5.51	5.5
Na^+	27.8	47.1	241	154	194	120
Ca^{2+}	22.7	33.6	211	185	190	131
Mg^{2+}	14.3	74.5	259	245	180	135
Cl^-	37.7	41.2	90.4	62	58.1	51
SiO_2	0	0	254	230	293	280

Table 3.2: Observed and initial chemical composition of groundwater, precipitation, and glacial melt in different portions of the Gavilan Machay watershed. The same chemical composition was applied to both barren and ice-covered areas. Precipitation concentrations were used for both glacial meltwater and precipitation at all times in the simulations.

of hydrochemistry in the watershed.

3.4.2.2.2 Reactive Transport of Sodium, Calcium, and Magnesium

In addition to atmospheric deposition and melt inputs, reactive ions, including Na^+, Ca^{2+}, and Mg^{2+}, are also released into water through weathering, including mineral dissolution from soil and rock containing feldspar and pyroxenes minerals. Albite ($NaAlSi_3O_8$) and diopside ($CaMgSi_2O_6$) were respectively chosen as representative model minerals from these groups because they were prevalent across multiple soil and rock samples, and the choice of two minerals enabled us to most simply produce observed concentrations throughout the watershed (Table 3.1). Despite anorthite being more common than diopside among the different soil samples, diopside was included in the model instead of anorthite, because diopside contains Mg^{2+} and Ca^{2+} and can thus be used alone to efficiently simulate both those major cations in the stream and groundwater (anorthite contains Ca^{2+} but not Mg^{2+}). XRD analysis of soil samples over depth supports the implementation of a vertically homogeneous mineral composition. Other minerals containing elements with very low observed ion concentrations (e.g., Fe^+ and Mn^+) were not considered in order to focus on major elements and reduce computational complexity. We represented kinetic dissolution of albite and diopside using parameters from literature with further calibration via Monte Carlo simulations (100 cases) to reproduce observed streamwater and groundwater solute concentrations and

stream discharge (Table 3.3) (calibration details provided below). Mineral fractions of albite and diopside were set sufficiently high such that their availability for dissolution was not a limiting factor in simulations, based on the ubiquitous observation of silicate minerals throughout all samples.

Mineral Dissolution	$log_{10}K^{a}_{eq}$	$log_{10}k^{b}_{ref}$	SSA(m^s/g)^c
$NaAlSi_3O_{8(s)}$ (Albite) + $4H_2O$ + $4H^+ \rightarrow Na^+ + Al^{3+} + 3H_4SiO_4$	2.74	-10.9 (-9.89 to -11.9)	0.075 (0.02 – 1.09)
$CaMgSi_2O_{6(s)}$ (Diopside) + $2H_2O$ + $4H^+ \rightarrow Ca^{2+} + Mg^{2+} + 2H_4SiO_4$	20.96	-13.2 (-9.95 to -14.24)	0.086 (0.001 – 2.3)

[a] K_{eq} from the database EQ3/6 (Wolery, 1992)
[b] Intrinsic dissolution rate parameter at reference temperature (298.15 K) (k_{mref}) set to values that fall within the range presented in Brantley et al. (2008) (shown in parentheses).
[c] Calibrated soil mineral specific surface area (SSA) values; these fall within the range of values presented in Brantley et al. (2008) (shown in parentheses).

Table 3.3: Dissolution reactions and kinetic and thermodynamic parameters for minerals included in the model. Values in parentheses are the ranges found in Brantley et al. (2008).

3.4.3 Model Scenarios

Following calibration, the model was implemented for two different scenarios. Scenario 1 represents current conditions with accelerated glacier melt. Scenario 2 is identical to scenario 1 except that the model simulation does not include glacial meltwater. Comparison of the hypothetical scenario 2 with scenario 1 allowed us to evaluate the role of glacier melt in controlling geochemical conditions in scenario 1. We chose Na^+ as the representative diagnostic solute among the three dominant reactive ions observed in the watershed (Na^+, Ca^{2+}, and Mg^{2+}); simulation results of the other dominant reactive ions were qualitatively similar to Na^+ results.

3.4.4 Model Calibration

In order to reproduce the observed soil water pH, we simulated a continuous release of aqueous CO_2 at $10^{-2.35}$ M concentration in the vegetated parts of the watershed (Figure 3.1a) to represent the acidity introduced by both CO_2 gas and other organic acids produced through microbial and plant respiration. This aqueous CO_2 concentration is an order of magnitude higher than equilibrium concentrations of $10^{-3.5}$ – $10^{-3.2}$ M for the typical bare soil CO_2 partial pressure range of 1.02 – 2×10^{-2} atm (Hasenmueller et al., 2015). No additional CO_2 was implemented in the barren and ice-covered grid cells, which we assume to have low organic content soils. After adjusting the release rate of aqueous CO_2 in the vegetated areas according to pH observations, we calibrated mineral SSA and hydraulic properties as follows.

Seven key parameters including horizontal and vertical hydraulic conductivity, porosity, van Genuchten water retention curve parameters (α and β), and albite and diopside specific surface areas were calibrated by choosing the parameter set that produced the best fit to observations (available stream discharge data from June 2015 to March 2016, and stream and groundwater chemistry in June 2015 and in June 2016) among 100 Monte Carlo simulations. Note that the intrinsic kinetic dissolution parameter k_{ref} was not further calibrated in order to reduce the calibration complexity; we consider this to be an acceptable simplification because k_{ref} is multiplied by the calibrated parameter SSA when calculating dissolution rates (Eq. 3.1). Although Flux-PIHM (without the BioRT module) has been previously implemented to investigate water balance partitioning in the watershed (Saberi et al., 2019), hydraulic parameters were recalibrated here with hydrochemical observations to further constrain flow pathways (Schilling et al., 2019) and to ensure proper representation of solute transport (further discussion is in Appendix B, Section B4). In this work, the pre-calibration parameter distributions for the 100 Monte Carlo runs were generated using Latin hypercube sampling from ranges based on soil studies in the Ecuadorian Andes (Podwojewski et al., 2002; Minaya, 2016), other volcanic soil studies (Shoji et al., 1994; Célleri & Feyen, 2009; Montzka et al., 2017), and mineral parameter values presented in Brantley et al. (2008). For each Monte Carlo run, the mismatch over time (t=1 to T) between the simulation ($Model$) and corresponding observation (Obs) was quantified by the normalized

root-mean-square deviation ($NRMSD$):

$$NRMSD = \frac{1}{s}\sqrt{\sum_{t=1}^{T}\frac{(Model_t - Obs_t)^2}{T}} \tag{3.6}$$

with s, a measure of observation uncertainty, as the normalization factor. $NRMSD$ was calculated for each measurement type: hourly streamflow from June 2015 to May 2016 and Na^+, Ca^{2+}, Mg^{2+}, and Cl^- concentrations at four stream locations and two springs over the June 2015 and June 2016 field campaigns (separate values were determined for the distinct sampling campaigns). The average $NRMSD$ ($NRMSD_{ave}$) over the 49 different measurement types was used in the assessment of each Monte Carlo run. The Monte Carlo run with the lowest $NRMSD_{ave}$ was chosen for the final calibrated model result, and the subset of Monte Carlo runs with $NRMSD_{ave} \leq 1$ was used to represent the calibration uncertainty. Further details about the calibration procedure are in the Appendix B (Section B5, Table B4).

We relied on the widely used Nash-Sutcliffe efficiency (NSE) approach (Nash & Sutcliffe, 1970) to quantify model performance. Model results are considered satisfactory if 0<NSE<1, with NSE=1 as an indicator of a perfect match between observations and simulations (Moriasi et al., 2007). The traditional NSE is used here, which is calculated as follows (Nash & Sutcliffe, 1970):

$$NSE = 1 - \frac{\sum_{i=1}^{n}(Model_i - Obs_i)^2}{\sum_{i=1}^{n}(Obs_i - Obs_m)^2} \tag{3.7}$$

where Obs_m is the mean of observations over time and n is the number of measurements. NSE was only applied to discharge, because of the sparser availability of solute concentration measurements.

3.4.5 C-Q Power Law Model

In C-Q analysis, the relationship between solute concentrations and stream discharge is often fit to a power law relationship (Godsey et al., 2009):

$$C = aQ^b \tag{3.8}$$

where a and b are fitted parameters. The exponent b has been found to vary from -1 to +0.4 (Godsey et al., 2009; Herndon et al., 2015). The C-Q relationships are often considered chemostatic when b ranges between -0.2 and +0.2, while pure dilution (non-chemostatic end-member) occurs when b is equal to -1.

To investigate the overall influence of glacial melt on the hydrochemistry of the watershed, we compare C-Q power law models fit to simulation results with meltwater and without meltwater. Although C-Q analysis is typically applied to continuous measurements, here we rely on model simulations to overcome data sparsity and to explore different scenarios.

3.5 Results

3.5.1 Calibration Results

Calibrated values for geochemical reaction parameters and hydraulic parameters are shown in Tables 3.3 and B4, respectively. The Monte Carlo-based calibration results indicate that there is a unique set of parameters that produces the best fit to observations (Figure B2), and the calibration uncertainty around the best parameter set is greatly reduced from the full literature-based range (Table B4). Correspondingly, the calibrated simulation has a relatively well-constrained uncertainty around major ion concentration and stream discharge values, compared to the full set of Monte Carlo runs with literature-based parameter ranges (Figures 3.2, 3.3, 3.4, and B3). This reduction in uncertainty suggests that the discharge measurements and relatively sparse hydrochemical observations in this remote study site provide adequate model constraint to draw some meaningful insights about hydrochemical drivers.

With the calibrated model, simulated stream discharge matches observed discharge with an NSE coefficient of 0.87, which indicates that the model performance is satisfactory (Figure 3.2b). The slight lags between the simulated and observed discharge on multi-week and shorter timescales may be due to underrepresented flowpath heterogeneities in the model and uncertainties in calculating melt rates using a simple temperature-index model (Saberi et al., 2019). These discrepancies may affect the model's ability to correctly simulate the timing or magnitude of some short-term solute export events, but we consider the model to be still useful for capturing overall trends

and relationships.

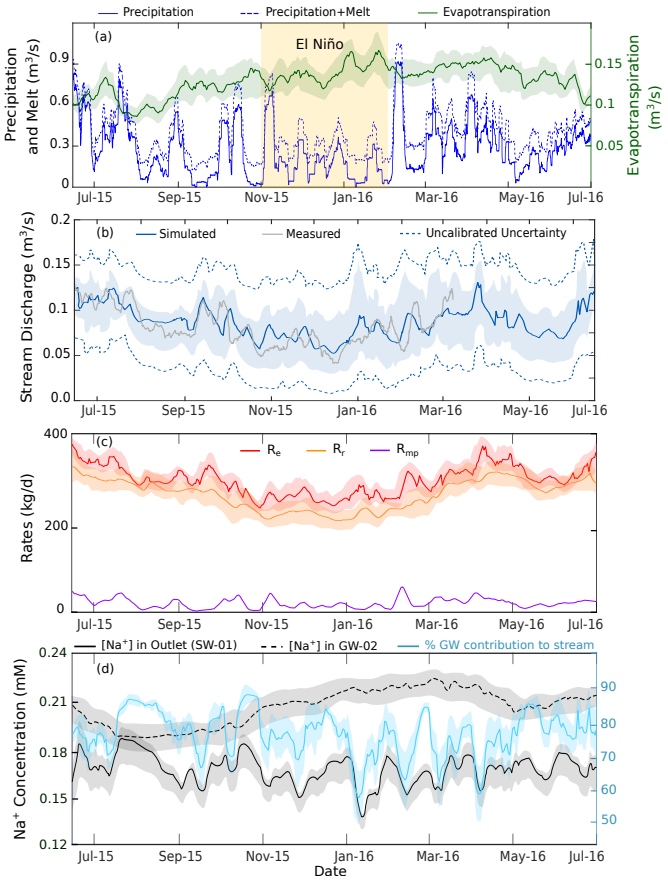

Figure 3.2: Weekly time series of: (a) precipitation (rainfall and snow) model inputs, ice-melt model inputs, and simulated ET over the watershed, with the warm and low-precipitation El Niño period shaded yellow; (b) simulated and observed stream discharge; (c) model input of Na^+ with precipitation and melt events (R_{mp}) to the watershed, simulated Na^+ export rate at the outlet (R_e), and simulated Na^+ release rate by albite dissolution (R_r) over the watershed; and (d) simulated Na^+ concentration in groundwater averaged over grid cells adjacent to the stream, simulated Na^+ concentration in the outlet (sampling site SW-4 shown in Figure 3.1a), and simulated percentage of groundwater contribution to streamflow. X-axis tick marks indicate the first of the month. Shaded areas show the calibration uncertainty, and in (b), the dashed lines indicate the pre-calibration (unconstrained) uncertainty.

Figure 3.3 demonstrates the importance of including mineral dissolution in the calibrated model in order to reproduce observed groundwater concentrations. Not only would groundwater concentrations be significantly lower without mineral dissolution at the two spring sampling locations (GW-1 and GW-2), but the model suggests there would also be a notable difference underneath higher elevation areas (with glaciers and in barren areas), which were not sampled, even with the shorter flow paths and residence times there. Without mineral dissolution, meteoric and melt inputs and ET would account for only 14-16% of the time-average concentrations throughout the watershed.

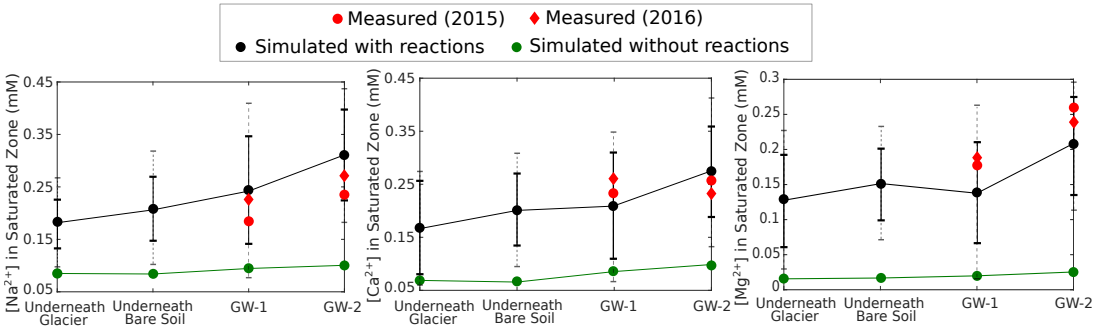

Figure 3.3: Simulated groundwater concentrations, averaged over the simulation year, of Na^+ (left), Ca^{2+} (middle), and Mg^{2+} (right) along an elevation gradient spanning the watershed for two different scenarios, with and without geochemical reactions, along with measured groundwater concentrations. Dashed error bars show the uncertainty boundary of the unconstrained Monte-Carlo simulations and solid error bars show the uncertainty in the calibrated result. Measured concentrations (red dots) at the GW-1 and GW-2 spring locations (map in Figure 3.1a) are compared against simulated groundwater concentrations for the corresponding grid cell. Average simulated groundwater concentrations underneath all glacierized (ranging from 5300 to 6280 m a.s.l.) and all bare soil cells (ranging from 4600 to 4900 m a.s.l.) are also shown to demonstrate the changes in concentrations simulated in the upper and middle parts of the watershed, where we lack spring / groundwater samples.

Correct representation of mineral dissolution effects on groundwater hydrochemistry is necessary for simulating observed stream concentrations (Figure 3.4), because the calibrated model shows that lateral groundwater flow is the major source (on average over time and space 78±7%) of discharge (compare blue lines in Figure 3.5e and g), with surface runoff contributing the remaining amount (22±7%). Figure 3.4 shows that

the calibrated Na^+ concentration simulations in the stream closely capture the observed spatial trends along the channel as well as changes between the two field campaigns in June 2015 and June 2016 (e.g., slightly lower Na^+ concentration at the outlet in June 2015, when discharge was somewhat higher than in June 2016, Figure 3.2b). Similar simulation results for Ca^{2+} and Mg^{2+} concentrations along the stream are included in Appendix B, Figure B3.

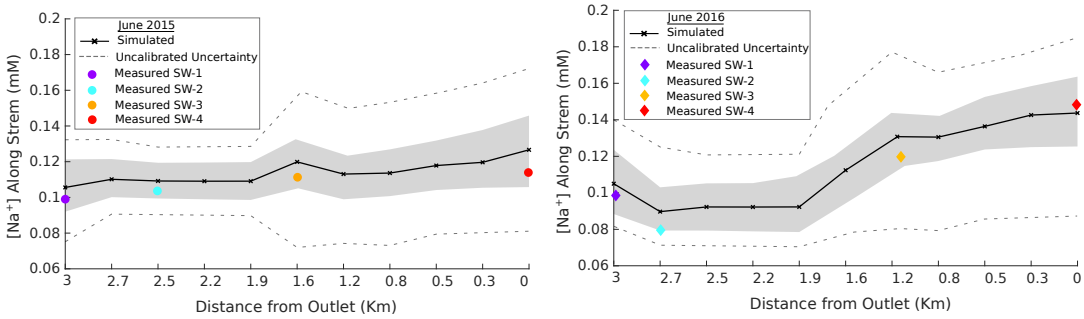

Figure 3.4: Simulated Na^+ at four different locations along the stream compared to the measured concentrations from June 2015 and June 2016. Dashed lines show the uncertainty boundary of the unconstrained Monte-Carlo simulations. Shaded area shows the uncertainty in the calibrated result, which is significantly reduced from the unconstrained range (shown with dashed lines).

3.5.2 Temporally Dynamic Drivers of Hydrochemical Processes

Using our calibrated model results, the Na^+ release rate (R_r) through albite dissolution in a particular grid cell is calculated by:

$$R_r = \left(\frac{C^t_{m,UZ} - C^{t-1}_{m,UZ}}{dt} \times WS_{UZ} + \frac{C^t_{m,SZ} - C^{t-1}_{m,SZ}}{dt} \times WS_{SZ} \right) \times A_g \tag{3.9}$$

where C_m is the mineral concentration of albite (kg/m^3), dt is the time increment of 1 day, the t superscript is the time index, UZ and SZ subscripts respectively indicate the unsaturated and saturated zones, WS is the water storage (m), and A_g is the grid cell area (m^2). The rate of Na^+ input through wet deposition with glacial melt and

precipitation (R_{mp}) is calculated by:

$$R_{mp} = (PrecipitationRate + IceMeltRate) \times C_p \times A_g \tag{3.10}$$

where C_p is the Na^+ concentration measured in precipitation (and is similarly applied to ice melt, see Table 3.2). Watershed-scale values for R_r and R_{mp} were determined by summing over all grid cells. The Na^+ export rate (R_e) is the product of stream discharge and Na^+ concentration at the stream outlet.

As can be seen in Figure 3.2b and c, the simulated export rate of Na^+ (R_e) primarily follows the temporal pattern of simulated stream discharge (correlation coefficient of 0.88), indicating that discharge is the stronger driver of export rate variability over time than the simulated concentration of Na^+ at the outlet (Figure 3.2e). This is because Na^+ concentration at the outlet is relatively constant year-round (coefficient-of-variation of 13%) compared to the variability in discharge (coefficient-of-variation of 44%). Both discharge and Na^+ export are lowest during the El Niño period (November through January), when there is the least precipitation (Figure 3.2a, b, and c).

The lower variability of Na^+ concentration at the outlet is due to the consistently substantial contribution of groundwater to streamflow (55-85%) in the model. Groundwater adjacent to the streams carries high concentrations of Na^+ (simulated 0.19 to 0.22 mM compared to 0.14 to 0.18 mM in the stream, Figure 3.2d) due to the release of Na^+ via albite dissolution (average $2.8 \times 10^2 \pm 6.2 \times 10$ kg/d), which is much higher than calculated meteoric and glacier melt inputs of Na^+ (average 0.3×10^2 kg/d) and accounts for the vast majority of the exported solute (average $2.9 \times 10^2 \pm 1.3 \times 10$ kg/d) (Figure 3.2c). Note that slight excess Na^+ inputs are net additions to groundwater storage of Na^+ over the simulation period.

However, simulated groundwater concentrations of Na^+ are not entirely constant over time (Figure 3.2d). During and just following the El Niño period (November through March), concentrations are higher than during the flanking wetter periods. This occurs despite the lower albite dissolution caused by lower moisture (Figure 3.2c), because high ET during that period (Figure 3.2a) concentrates Na^+ in the groundwater. Note that high ET continues into the months just following the El Niño period (see Figure 3.2a) because of continued warmer temperatures after precipitation resumes (see Appendix B, Figure B1). Interestingly, ET serves to both limit Na^+ release by

decreasing moisture - and thus wetted mineral surface areas - as well as boost Na^+ concentrations by removing water, with the latter having the prevailing control on groundwater concentrations. This counteracting ET effect on groundwater concentrations helps stabilize stream water concentrations, because times of slightly lower average groundwater flow contribution to streamflow (69% in January-March around the dry period, compared to 80% during the rest of the year) coincide with higher groundwater concentrations (Figure 3.2d). As a result, even though stream concentrations at the outlet show some variability on the shorter multi-week time scale (trending with temporal groundwater contributions), it maintains a relatively constant average magnitude around 0.17 mM over the different wetter and drier periods (Figure 3.2d).

As can be seen by comparing the blue lines in Figure 3.5e, g, and h, temporal variability in discharge, which drives the temporal variability in Na^+ export, is controlled by groundwater inputs to the stream in the model. While this might suggest that meltwater inputs play a relatively unimportant role in influencing export dynamics, model results indicate that an estimated 37% of groundwater originates from ice-melt that infiltrates into the ground (see Appendix B, Figure B1). This high estimate of ice-melt moving through the subsurface is constrained by observed reactive solute concentrations. A previous lower estimate from Saberi et al. (2019) of 16%, which was not constrained by hydrochemical data, over-simulated stream dilution from melt-driven surface runoff. Both Saberi et al. (2019) and this study estimated similar overall glacier melt contributions to discharge ($\sim$50%). In the current model, the notable correlation over time between precipitation plus melt and lateral groundwater flow to the stream (correlation coefficient of 0.65) suggests that precipitation and infiltrated ice-melt travel relatively fast to the stream such that their temporal variability is not significantly dampened and lost in the subsurface (blue line in Figure 3.5e).

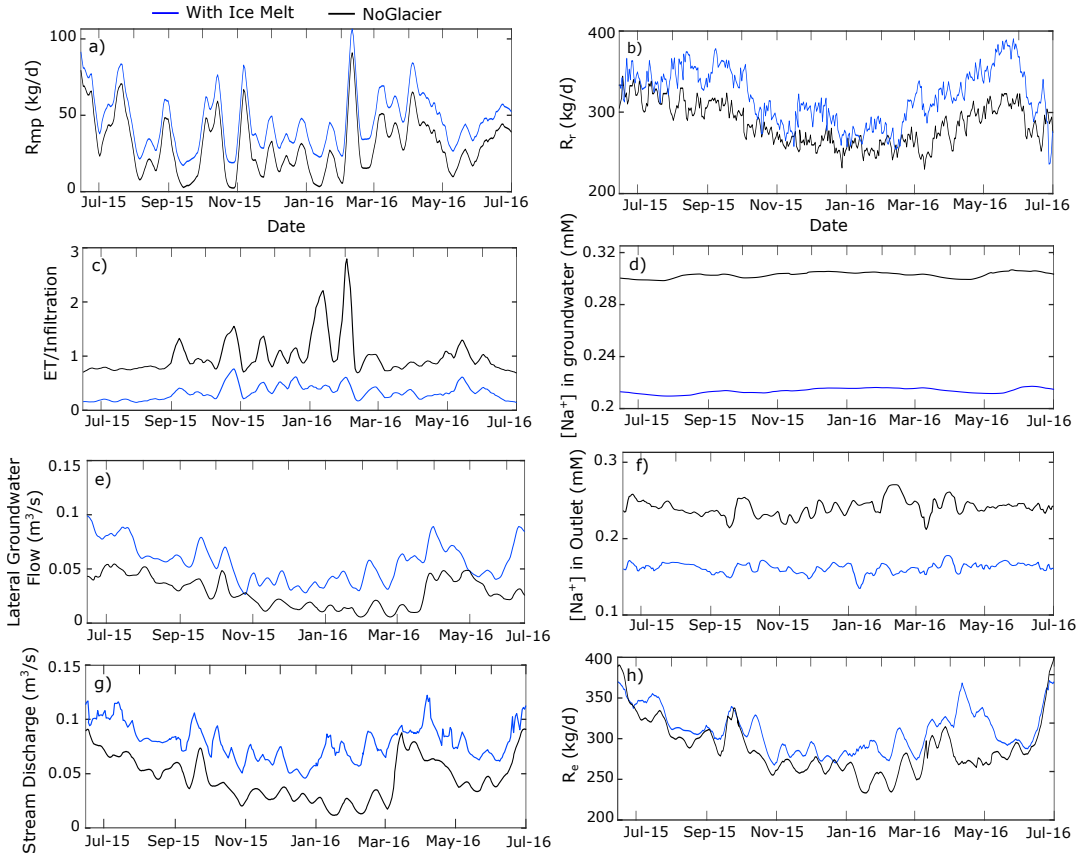

Figure 3.5: Simulated watershed results for (a) Na^+ input via melt and precipitation (R_{mp}), (b) Na^+ release rate via albite dissolution (R_r), (c) the ratio of evapotranspiration to infiltration, (d) Na^+ concentrations in groundwater, (e) groundwater discharge to the stream, (f) Na^+ concentrations in the outlet, (g) stream discharge, and (h) Na^+ export rate (R_e). The blue line represents the scenario with melt and black like the scenario without glacial melt.

The influence of ice melt on groundwater flow and stream discharge is apparent by comparing the calibrated model results with ice melt (blue lines) against the model scenario without ice melt (black lines) in Figure 3.5e and g. Through this influence, glacier melt can be seen to impact the export of weathering solute Na^+ (Figure 3.5h). The impact results from a combination of hydrological and geochemical factors that are

evident throughout the simulation year but are often more pronounced during the dry period of November through January, when water inputs are small without ice melt, and around April, when both high melt and high precipitation are sustained (Appendix B, Figure B4). Relative to the model scenario without ice-melt inputs, ice-melt overall leads to higher Na^+ release rate through albite dissolution because of greater groundwater storage (Figure 3.5b), but lower Na^+ concentrations in groundwater and stream water (Figure 3.5d, f) occur because of dilution. A simple mass balance calculation can show that groundwater concentrations generally scale with the ratio of ET to infiltration (where infiltration is defined as precipitation plus meltwater minus surface runoff) (details in Appendix B, Section B6). Despite similar ET in the two scenarios, this ratio becomes low in the melt scenario because of substantial amounts of meltwater moving into the subsurface (Figure 3.5c). However, even though Na^+ concentrations in streamflow are lower with ice-melt, this is offset by higher discharge when determining impacts on export rates. With ice-melt, export ultimately increases to reach mass balance with greater mineral dissolution triggered by infiltrating meltwater. Without glacier melt, the model predicts an average 23% lower export of Na^+, corresponding to an average 49% decrease in stream discharge. This decrease in the stream discharge offsets an average 53% increase in Na^+ concentration in the stream, resulting in the lower export rate.

3.5.3 Spatially Variable Drivers of Hydrochemical Processes

Distributions across the watershed of simulated hydrologic and geochemical variables in Figure 3.6 can be used to probe spatially variable processes that control hydrochemical conditions. Of particular interest are the processes that give rise to the release of Na^+ and its concentration in groundwater, which were found in Section 3.5.2 to significantly influence stream concentrations and export at the outlet. Na^+ is released with albite dissolution at a rate driven by the wetted surface area of the mineral (Eq 3.1). Within the unsaturated zone, wettest conditions occur where ET/infiltration is lowest (Figure 3.6a, b). The ratio of ET to infiltration, which controls soil water availability and correspondingly influences solute concentrations, mostly follows spatial patterns of ET rather than infiltration (not separately shown here). Infiltration is greatest below the glacier ablation zone and also reflects the precipitation lapse rate, but this has a much

more minor effect than ET on the ratio. ET patterns are ecologically driven, with greatest rates simulated in the vegetated páramo region where temperatures are also warmer. The ET-driven soil moisture distribution drives the highest rates of unsaturated zone Na^+ release in the upper portion of the watershed, above the vegetation line (Figure 3.6e, see caption for note about low concentrations in the ablation zone and adjacent to streams).

Deeper groundwater storage trends differ and instead track ice melt and surface water convergence areas (Figure 3.6c). This results in the highest Na^+ release rates in the saturated zone being simulated below the ablation zone and along the stream channel and tributary (Figure 3.6f). With vertically homogeneous mineral parameters in the model, saturated zone albite dissolution rates generally dominate the total subsurface (saturated plus unsaturated zone, Figure 3.6d) release because of higher water volumes there. However, away from the ablation zone and stream, lower simulated release can be seen at lower elevations because of ET-controlled processes in the unsaturated zone.

The spatial pattern of Na^+ concentration in the subsurface (unsaturated and saturated zones, Figure 3.6g) does not entirely mimic that of the Na^+ release. Elevated concentrations with some dispersion can generally still be detected around the ablation zone and along the stream, resulting in a statistically significant spatial correlation of 0.52 between Na^+ concentration and Na^+ release over the watershed. However, away from the ablation zone and channel, slightly higher concentrations were simulated below the vegetated areas - opposite from the albite dissolution pattern. This reversal can be attributed to ecohydrological processes in the unsaturated zone (Figure 3.6h). Although there is less Na^+ release with albite dissolution below vegetated areas, high ET/infiltration imparts a concentrating effect such that for upland grid cells (defined here as cells not directly adjacent to the stream and not in the ablation zone), there is a spatial correlation of 0.81 between Na^+ concentration and ET/infiltration. This concentrating effect can be clearest seen with the conservative solute Cl^-, which has concentrations that have a strong spatial correlation (0.8) with ET/infiltration over the entire watershed at all depths (Figure 3.6j-l).

The spatial hydrochemical relationships within the watershed affect both solute export and stream concentrations. Because of the glacier melt and steep topography,

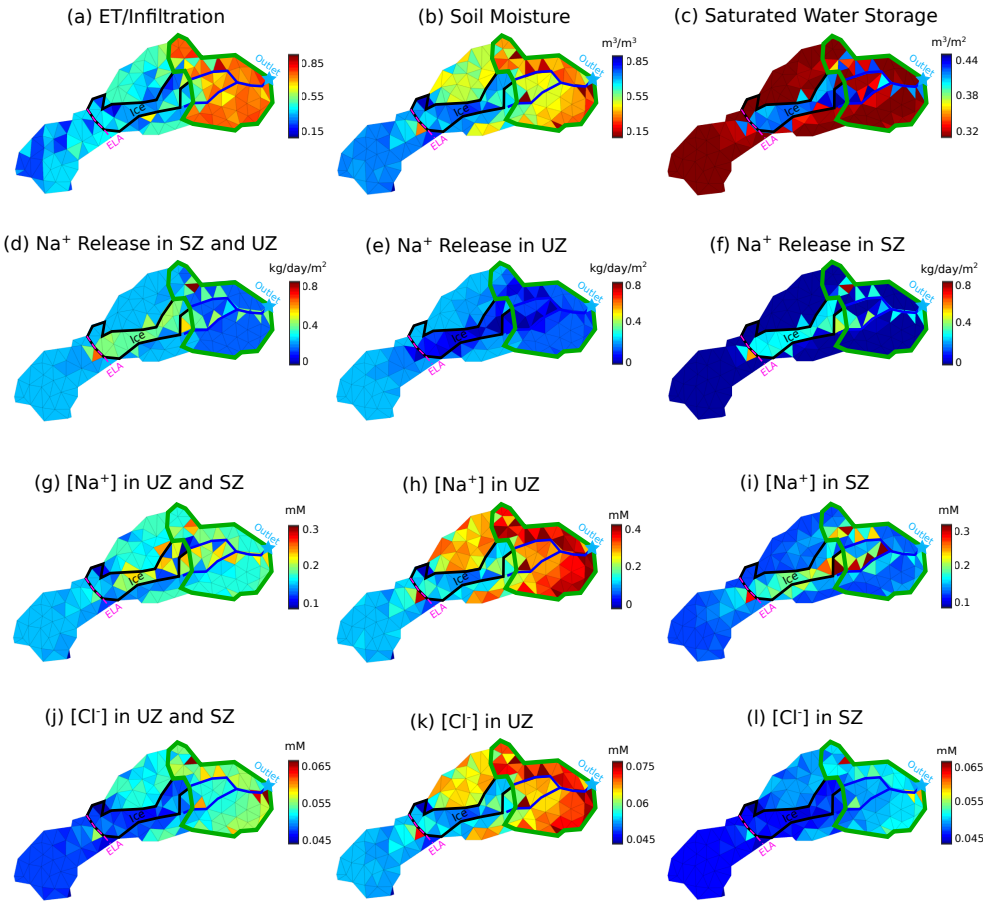

Figure 3.6: Time-averaged simulations of (a) the ratio of evapotranspiration to infiltration, (b) soil moisture, (c) saturated water storage, (d) Na^+ release rate in saturated and unsaturated zones, (e) Na^+ release rate in unsaturated zone (note that low unsaturated zone Na^+ release around the ablation zone and streams is due to the very small unsaturated depth there compared to saturated depth), (f) Na^+ release rate in saturated zone, (g) Na^+ concentration in saturated and unsaturated zones, (h) Na^+ concentration in unsaturated zone, (i) Na^+ concentration in saturated zone, (j) Cl^- concentration in saturated and unsaturated zones, (k) Cl^- concentration in unsaturated zone, and (l) Cl^- concentration in saturated zone. The ELA is shown with a dashed purple line, the ablation zone (glacierized area below the ELA) is outlined with a black line, the vegetated (páramo) area is outlined with a green line, the stream channel and tributary are shown with a blue line, and the outlet is shown with a light blue star.

ablation and convergent areas yield the majority of the total Na^+ release, which comprises most of the exported solute. Upland areas also contribute an appreciable fraction of the total Na^+ release (27%) that will likely increase as ice-melt attenuates. Through the contribution of upland areas, vegetation-driven ET patterns influence solute export by decreasing wetted mineral surface areas. The influence of spatially distributed groundwater concentrations on stream chemistry may be less obvious, given that it is the groundwater concentrations just adjacent to the stream that impart the direct impact. However, resolving the simulated spatial distributions of Na^+ concentrations in groundwater into roughly wetter and drier periods in Figure 3.7c reveals that during December-March, when ET is higher (Figure 3.2a and 3.7a), subsurface concentrations of Na^+ are higher across the watershed compared to wetter (lower ET) periods, despite overall lower Na^+ release (Figure 3.7b). During the dry period, these higher concentrations throughout the watershed move toward the convergence areas, resulting in the most highly elevated groundwater concentrations around the stream of the entire year (Figure 3.7c), despite lower dissolution. As noted in Section 3.5.3, this higher groundwater concentration somewhat buffers against lower groundwater flows to the stream during December-March, thus helping to maintain relatively constant seasonal averages in stream concentrations (Figure 3.2d).

3.5.4 C-Q Relationship

Our model results provide one of the first glimpses at continuous year-long C-Q relationships for tropical glacierized watersheds (Figure 3.8a), which are typically lacking in observations. Although the calibration data included only two observation times for stream outlet concentrations, the calibration uncertainty constrained by the full dataset is sufficiently small such that a characteristic C-Q shape emerges (see error bars in Figure 3.8a, b). For simulations with ice-melt, the relationship between stream discharge and the simulated Na^+ concentrations at the outlet is considered to be chemostatic based on a C-Q power law exponent of -0.08 (using the chemostatic range suggested by Godsey et al. (2009)). However, various dilution events also appear (indicated in red in Figure 3.8), and all of these (especially those with lowest concentrations) occur either during high peaks in surface runoff to discharge (Figure 3.8b), or shortly (usually 1-day) after a high peak due to the time needed for runoff generated in the watershed

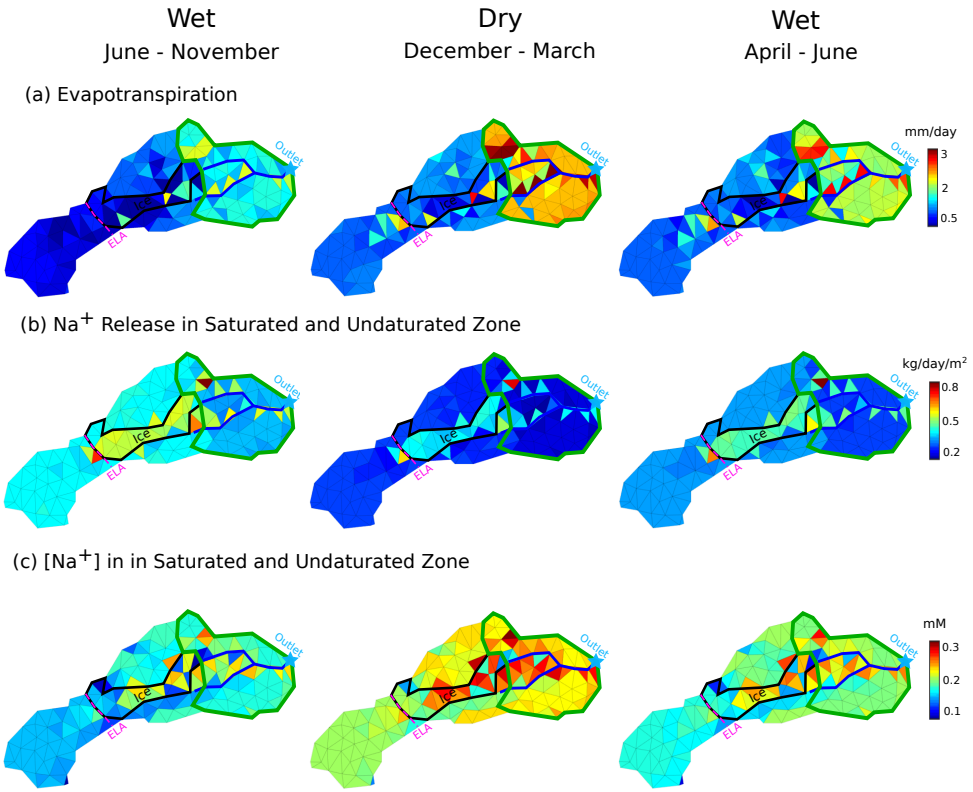

Figure 3.7: Simulations averaged separately over three time periods (June-November, December-March, April-June) of (a) evapotranspiration, (b) Na^+ release in saturated and unsaturated zones, and (c) Na^+ concentration in saturated and unsaturated zones. Note that the drier period (December-March) shown here slightly lags the El Niño months (November-January) in order to coincide with the highest groundwater Na^+ period (see Figure 3.2a, d). The ELA is shown with a dashed purple line, the ablation zone (glacierized area below the ELA) is outlined with a black line, the vegetated (páramo) area is outlined with a green line, the stream channel and tributary are shown with a blue line, and the outlet is shown with a light blue star.

to reach the stream outlet. Thus, large surface runoff contributions to discharge drive these dilution events, and these can occur any time of the year (Figure 3.8c) due to year-round ablation, often when melt events coincide with times of significant rain (see Figure B4 in Appendix B). In simulations without glacier melt, peak discharge (Figure 3.5g) and surface runoff contributions to discharge (compare Figure 3.8c and f) greatly decrease. Overall, Na^+ concentrations in groundwater increase (Figure 3.5d), and almost all of the strongest dilution events disappear (Figure 3.8e, f), making the C-Q relationship even more chemostatic (C-Q power law exponent of -0.01) (Figure 3.8d). The disappearance of most dilution events in the no-ice scenario confirms that it is the combination of melt and precipitation events, and not precipitation peaks alone, that generate the dilution episodes when there is ice-melt.

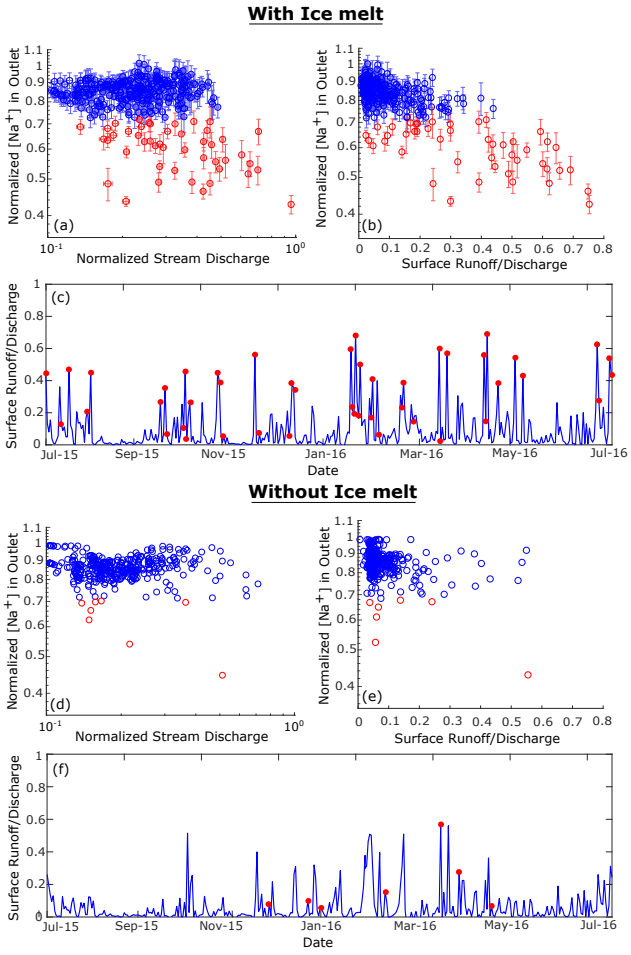

Figure 3.8: The relationship between simulated daily stream discharge and simulated daily Na^+ concentrations at the outlet, with ice melt (a) and without ice melt (d). Error bars show the uncertainty for the calibrated model result. Na^+ concentrations and discharge are normalized by the largest corresponding value at the outlet over the simulation period. The relationship between the surface runoff to stream discharge ratio (fraction of total discharge) and simulated Na^+ concentrations at the outlet, with ice melt (b) and without ice melt (e). The contribution of surface runoff to discharge (fraction of discharge) over time, with melt (c) and without ice melt (f). Red dots in each plot are points for which the normalized Na^+ concentrations in the outlet are less than the threshold of one standard deviation below the mean value in the case with melt water.

Comparison of the two model scenarios suggests that in Gavilan Machay, glacier melt produces many of the major surface runoff events relative to total discharge. These events can produce diluting episodes throughout the year in an otherwise chemostatic environment where groundwater (subsurface lateral flow) mobilizes solutes from reactive subsurface minerals. These results suggest that the C-Q patterns are driven by the relative control of two end-member sources of water with distinct chemistry: surface runoff (which contributes 22% of the stream discharge) with lower Na^+ concentrations and groundwater lateral flow (which contributes 78% of the stream discharge) with higher Na^+ concentrations. Although a notable amount of ice-melt infiltrates and contributes to groundwater, ice-melt inputs lead to more frequent times when the ratio of surface runoff to groundwater contribution to the stream is high, and this produces a diluting effect. A similar behavior was observed in simulations at the Coal Creek study watershed in Colorado, where the C-Q relationship was found to depend on the seasonally switching dominance among two end-members (in their case, shallow groundwater and deeper groundwater) and the distinction among their chemistries (Zhi et al., 2019). An interesting difference in our inner-tropics settings is that the switching happens throughout the year and does not strongly correspond with particular seasons. Without ice-melt, Gavilan Machay is governed by a single end-member, lateral groundwater flow, which results in much more chemostatic conditions; this is similar to BioRT-Flux-PIHM findings by Li et al. (2017b) for the Shale Hills study watershed in Pennsylvania, where groundwater contributions to streamflow generated steadier and higher stream concentrations.

3.6 Discussion

3.6.1 Subsurface Processes Play a Dominant Role in Controlling Solute Export

Based on our model results for glacierized Gavilan Machay, the high groundwater contribution to streamflow (78%), the dominant contribution by albite dissolution to Na^+ inputs to the watershed (87%), and the largely chemostatic stream concentrations (C-Q power law exponent of -0.08) together establish that subsurface processes, including

weathering and fluid flow, serve as major drivers of watershed hydrochemistry and solute export. Chemostatic conditions have been previously observed in steep Andean watersheds without glaciers, and this has been attributed to high erosion rates and/or long fluid transit times (Torres et al., 2015; Bouchez et al., 2017). Our model does not explicitly include erosion, but a ready source of weatherable silicate minerals is an important aspect of our model. Our implementation of a non-limiting concentration of dissolvable silicate minerals could implicitly represent a rapidly replenishing supply due to erosion along steep slopes and/or subglacial erosion. In fact, our estimated area-normalized Na^+ flux from Gavilan Machay (10.6 t/km^2/y) falls within the range of those found in watersheds with similar glacier coverage where relatively high erosion rates have been attributed to snow and ice melt and sub-glacial weathering (e.g., 8 t/km^2/y for the Thjorsda glacier in Iceland with 35% glacier coverage (Gislason et al., 1996), and 17 t/km^2/y from the Scott Turnerbreen glacier in Norway with 32% glacier coverage (Hodgkins et al., 1997)). Thus, although erosion quantification was beyond the scope of our study, it is likely that the unlimited supply of reactive minerals in the model includes contributions from erosion occurring at the site.

We further note that at our site, the young volcanic parent material also supports the model implementation of unexhausted reactive silicate minerals, even without considering high erosion rates. Roadcut outcrops reveal ash layers that represent fresh weatherable and conductive material delivered by earlier Chimborazo eruptions, as well as by modern activity on nearby Volcán Tungurahua (Appendix B, Figure B5), including its recent eruption in 2014 (ash in farther away watersheds around Cuenca, Ecuador has been attributed to Tungurahua (Buytaert et al., 2006)). Further, bedrock outcrops are well-fractured, suggesting that the soil zone is underlain with permeable volcanic rocks that XRD results show to contain silicate minerals. This observation supports a conceptual model of fracture flow weathering the bedrock, which matches that proposed by Torres et al. (2015) for their Andean study catchments, and is consistent with studies that similarly noted active weathering zones in fractured bedrock of diverse lithologies (Anderson et al., 1997; Tipper et al., 2006; Calmels et al., 2011; Andermann et al., 2012; Salve et al., 2012; Kim et al., 2014). Although we lack direct evidence about the weathering zone thickness at Gavilan Machay, the presence of weatherable silicate minerals in both upper soil and lower bedrock units is supported by our XRD analysis of soil

and rock samples and by our ability to match observed hydrochemical and hydrological conditions with this assumption in the model.

Our large simulated groundwater contribution to discharge (78%) implies that most flow paths and transit times through the thick weathering zone are long compared to an alternate case in which there is significant surface runoff. During the model calibration, this longer contact time was in fact needed to reproduce the observed weathering solute concentrations in the simulations. In general, a long transit time can be responsible for chemostatic conditions when it approaches the time needed to reach geochemical equilibrium with the mineral (Maher, 2011; Maher & Chamberlain, 2014; Wlostowski et al., 2018). However, in our case, observed concentrations are undersaturated with respect to albite and diopside (see Appendix B, Table B2), which is consistent with field observations and model outputs that indicate progressively increasing Na^+ concentrations in groundwater as one moves downgradient in the watershed (Figure 3.3). This suggests an intermediary travel time at our site that is longer than that of surface runoff but shorter than chemical equilibration times in the subsurface. Undersaturated geochemical conditions may suggest non-chemostatic behavior, contrary to our model results, because drier periods have slower groundwater flow and longer contact times for dissolution. However, less moisture during dry periods also lowers the wetted surface area of the minerals, which can slow dissolution rates (Figure 3.2c). Ultimately, our model shows that subsurface transit times less than equilibrium times may be adequate for maintaining relatively chemostatic conditions, because variable wetness conditions can offset differences in mineral contact times for determining total released solute mass from dissolution. Additionally, groundwater concentrations can be further modulated by ET (discussed more below), and temporally variable groundwater contributions to discharge can affect the impact of groundwater concentrations on stream concentrations (as discussed in Section 3.5.2).

While the pre-calibration uncertainty in flow pathways and geochemical processes are notably reduced using currently available data in our Monte Carlo-based model calibration (Section 3.5.1), we acknowledge that higher temporal resolution C-Q measurements and borehole observations would improve our proposed conceptual model of the subsurface. Collecting more frequent samples would enable us to constrain model simulations and the C-Q analysis during times of low-flow, in addition to the high flow

times captured in the previous field campaigns. Furthermore, obtaining samples from shallow and deep groundwater across the watershed and with denser coverage with elevation would allow us to more confidently constrain the rate at which groundwater concentrations increase from higher to lower altitudes (Figure 3.7c).

3.6.2 Vegetation Drives Spatiotemporal Variability in Groundwater Concentrations Through ET

Although previous studies have drawn connections between hydrochemical conditions and vegetation, most either focus on biogeochemical interactions with nutrients or organic compounds (Hood et al., 2003; Zakharova et al., 2007; Hood & Scott, 2008; Romero-Mujalli et al., 2019; Molina et al., 2019) or they do not identify specific processes responsible for observed correlations (Nédeltcheva et al., 2006; Hood & Scott, 2008; Williams et al., 2015; Wymore et al., 2017b). Few studies have examined ecohydrological controls such as ET on hydrochemical conditions. Our modeling study shows that altitude-controlled land cover is an important driver of the spatial variability of solute concentrations in the subsurface through ET. The spatial correlation between ET and subsurface concentrations is strongest for non-reactive solutes, because the only process altering their concentration after meteoric deposition is moisture removal via ET. Reactive solutes are affected by ET in two counteracting ways that ultimately result in a more complex relationship. Spatially and temporally, higher ET (in vegetated areas and during drier periods, respectively) decrease wetted mineral surface areas in the unsaturated zone and thus decrease Na^+ release rates with dissolution. However, at the same time, ET has the same concentrating effect as clearly seen with non-reactive solutes, and in our simulations, this effect dominates such that drier time periods and vegetated upland (away from stream channel) areas experience higher concentrations of weathering solutes in groundwater. This finding about ET controls on solute release and concentrations suggests that there may be ecohydrologically driven changes in watershed hydrochemistry as vegetation shifts upslope in mountainous watersheds. Upslope migration due to warming temperatures has already been noted in various mountainous catchments across the globe (Walther et al., 2005; Neilson et al., 2005; Feeley et al., 2011), including on Chimborazo, though migration rate estimates remain uncertain there (Morueta-Holme et al., 2015; Moret et al., 2019).

Further ecological factors may include land-use change (Ochoa-Tocachi et al., 2016a), changes in rooting depth and its impact on weathering rates (Morueta-Holme et al., 2015; Brantley et al., 2017), accelerated erosion and soil development with vegetation (Viles, 1990; Merritts et al., 1992; Drever, 1994; Brantley et al., 2012; Amundson et al., 2015), modified pH through increases in organic content and weathering agents such as organic acids (Drever, 1994; Zakharova et al., 2007; Finke et al., 2013), and biocycling of cations and removal of nutrients from soil by plant uptake or leaching (Trudgill et al., 1977). Our model results suggest that holding all other variables constant, higher ET with expanded vegetated areas could cause export rates of weathering solutes to decrease while stream concentrations increase. This could mean that ecosystems within Andean watersheds may receive a nutrient boost by increased solute concentrations in groundwater and streamflow, but delivery may be exhausted at farther downgradient locations due to decreased export.

Importantly, the páramo is a unique, high-altitude ecosystem that encompasses distinct growth forms that may not all be fully represented by default grassland plant-functional-type parameters in land-surface models (Minaya, 2016). Because migration patterns on Chimborazo affect plant type distributions in addition to vegetation line elevation (Morueta-Holme et al., 2015), resolving canopy and biochemical properties within páramo communities may be necessary for robustly predicting future ecohydrological changes and their geochemical implications.

3.6.3 Glacier Melt Increases Solute Export and Produces Episodic Dilution Events

Consistent with a previous global study on glacierized catchments by Torres et al. (2017), our model results for Gavilan Machay showed that glacial melt increases the export of weathering solutes by increasing stream discharge and weathering rates, despite lowering solute concentrations. Some studies have attributed this increase in export to higher erosion rates in glacierized watersheds - often subglacial erosion (Tranter, 2006; Herman et al., 2013). As discussed above (Section 3.6.1), erosion is not explicitly represented in the model but could be implied by the implementation of a non-limiting supply of reactive silicate minerals. In addition to possible erosional processes, we argue that the large amount of ice-melt that infiltrates in Gavilan Machay is key to both the increased

export rates and the simulated C-Q behavior in the watershed. Infiltrated meltwater follows a relatively long flow path starting at high altitudes in the watershed and continues through our proposed conceptual model of a thick weathering zone (comprising both a soil and fractured bedrock layer). As discussed in Section 3.5.2, the infiltrated ice-melt increases water storage in the weathering zone, thereby accelerating silicate dissolution rates, and ultimately driving higher export of weathering solutes.

For C-Q behavior, without ice melt, the model shows very strong and clear chemostastic conditions, which is consistent with field-observations by Torres et al. (2015) for non-glacierized Andean catchments. With ice, because a notable amount of meltwater infiltrates and moves through weatherable soil and fractured bedrock, the C-Q exponent still falls within the general chemostatic range. However, an aseasonal two end-member system emerges that is marked by episodic dilution events superimposed on a chemostatic C-Q background (Section 3.5.4). This C-Q pattern is unique compared to previously studied temperate glacierized systems. Many temperate studies showed clear non-chemostatic dilution behavior during the melt season (e.g., Collins (1979, 1983, 1999); Brown (2002); Hindshaw et al. (2011); Kumar et al. (2019)), while others showed strong chemostatic (Clow & Mast, 2010; Wlostowski et al., 2018) or mobilizing (Lewis et al., 2012; Stachnik et al., 2016) behavior during melt seasons due to accelerated mineral dissolution and increased hydrological connectivity. At Gavilan Machay, because of the year-round ablation and humid conditions, solute mobilization by melt inputs is subtle relative to discharge variability; instead, melt coinciding with large precipitation events produce peak surface runoff contributions throughout the year that generate episodic dilution.

Though a growing number of studies have investigated groundwater processes in glacierized watersheds across climates (Clow et al., 2003; Liu et al., 2004; Huth et al., 2004; Hood et al., 2006; Tague et al., 2008; Favier et al., 2008; Tague & Grant, 2009; Baraer et al., 2009; Andermann et al., 2012; Cauvy-Fraunié et al., 2013; Baraer et al., 2015; Pohl et al., 2015; Somers et al., 2016; Minaya, 2016; Schmieder et al., 2018; Harrington et al., 2018; Saberi et al., 2019; Somers et al., 2019), most have not quantified the contribution of ice-melt to groundwater nor examined possible ice-melt interactions with precipitation. Given that tropical Andean watersheds together supply $\sim$50% of the mean annual flow of the main stem of the Amazon River (Dunne et al., 1998), expanding

our findings on the hydrochemical effects of infiltrating meltwater – from glaciers and snow – to other tropical Andean water sheds will be important for characterizing and ultimately quantifying their regional-scale influence on critical downstream ecosystems. Our results suggest that some of the disproportionate solute inputs from the Andes to the Amazon could be driven by meltwater and subsurface interactions, and these will change as ice and snowpacks diminish in the future.

The importance of meltwater infiltration likely also applies to other settings within and outside the Andes, including not only fractured volcanic mountains, but also locations with sedimentary and metamorphic lithologies, where weathering in fractured media has similarly been observed (Tipper et al., 2006; Calmels et al., 2011; Andermann et al., 2012; Salve et al., 2012; Kim et al., 2014). Further, our model results may become relevant for glacierized watersheds with current dry-season melt periods if they shift to warmer and wetter conditions in the future. Overall, our work suggests that under warming conditions, as ice-melt contributions attenuate with glacier retreat, fractured systems may see the greatest decreases in the export of weathering solutes, even as concentrations of these solutes increase and stabilize. The decrease in solute export may be exacerbated by increases in vegetation cover and ET, though exact changes will also depend on future precipitation and temperature conditions.

It should be noted that our model relies on a temperature-index parameterization for glacier melt that was calibrated to field observations (Saberi et al., 2019), but simplifies the influence of other climatic factors. Therefore, in addition to higher resolution C-Q observations to confirm simulated dilution episodes, our conceptual model of ice-melt processes would also be improved with a more mechanistic ice melt module, which was not possible in the current study due to data limitations.

3.7 Summary and Conclusion

Due to difficult access and data sparsity in tropical glacierized watersheds, there is a critical knowledge gap about their hydrochemical response to rapidly retreating glaciers under climate change. This study addressed this challenge by applying the recently developed BioRT-Flux-PIHM model to probe spatiotemporally variable physical, ecological, and geochemical processes within a tropical glacierized watershed in order to

determine drivers of solute concentrations and export. Calibrated to hydrochemical and discharge measurements from the Gavilan Machay watershed on Volcán Chimborazo, the model also provided one of the first continuous C-Q relationships in a tropical glacierized watershed, which we were able to relate to the simulated processes within the watershed.

We found that unlike canonical flushing/chemostatic/dilution behavior, glacierized Gavilan Machay simulations exhibit a unique C-Q pattern that comprises a mostly chemostatic graph, but superimposed by melt-driven dilution events. The unique C-Q pattern with ice-melt was found to be controlled by the interacting effects of subsurface flow through young volcanic soils and fractured bedrock, altitude-controlled vegetation and ET, and year-round glacier melt in a sub-humid climate (Figure 3.9a). The mostly chemostatic background with ice-melt was attributed to the large contribution of groundwater to streamflow (78%), which moves through weatherable volcanic soils and fractured volcanic bedrock and has a notable fraction (37%) consisting of infiltrated ice-melt. Model simulations suggest that subsurface transit times at Gavilan Machay may not be as long as mineral equilibrium times, often a requirement for chemostatic behavior. However, relatively constant stream water concentrations were nonetheless maintained, because in higher ET times and locations, slower dissolution rates with lower moisture were offset by the concentrating effects of ET. Ice-melt did not all infiltrate; especially during times when ice-melt events coincided with large precipitation peaks, they triggered high contributions of low-concentration surface runoff to discharge, driving episodic dilution events to occur.

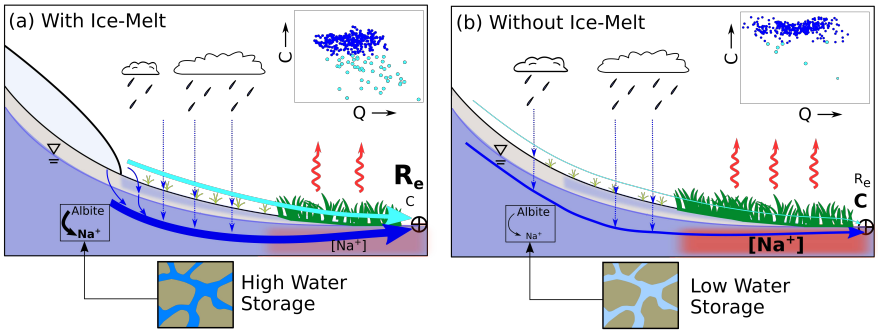

Figure 3.9: Schematic diagrams showing inferred controls on the hydrochemistry of a tropical montane watershed for (a) the present-day scenario with ice-melt and (b) a scenario without ice-melt, capturing potential changes after glaciers fully retreat. The presence of glaciers allows for higher solute export (R_e) when ice-melt infiltrates, because this raises groundwater storage and accelerates mineral dissolution in a weathering zone of soil overlying fractured bedrock. Both scenarios exhibit some degree of chemostatic behavior (dark blue points on the log C-log Q inset graphs), because lower dissolution rates in drier times and locations are offset by the concentrating effect of greater ET (red arrows). With ice-melt, coincident ice-melt and precipitation events further trigger surface runoff events (light blue arrow) that produce dilution episodes any time of the year (light blue points in C-Q inset). These dilution events mostly disappear without ice-melt, causing the watershed to shift to much more chemostatic conditions with higher solute concentrations (C) at the outlet. As glaciers fully retreat, the increase in solute concentrations and decrease in solute export will likely be exacerbated by higher ET as warming conditions also cause vegetation to migrate upslope.

Our findings have important implications for vulnerable tropical environments in which glaciers are fast-retreating and vegetation is shifting upslope - possibly at above-average rates - due to warming temperatures (Figure 3.9b). Our results suggest that attenuating ice-melt inputs will decrease groundwater storage, and thus lower weathering rates and solute export. These effects may be compounded by expanding areas of vegetation on the montane slopes, which will increase ET, thereby further reducing wetted mineral surfaces and weathering, while also increasing stream water concentrations. While these changes may allow for a shift to much more chemostatic behavior with

higher concentrations of solutes such as Na^+, Ca^{2+}, and Mg^{2+}, the overall decrease in solute export (by 23% in the model scenario without ice-melt) will limit the transport and delivery of solutes to farther away areas in the Amazon Basin. This could have implications for downstream ecological productivity, given the role of these solutes as plant macro- and micronutrients.

Our work identifies features of tropical glacierized watersheds like Gavilan Machay that are important drivers of hydrochemical behavior but may be distinct from other more intensively studied temperate glacierized watersheds. While the combination of these physical, ecological, and geochemical factors may be unique to certain tropical glacierized watersheds, our findings prompt further evaluation in other settings of currently understudied processes, including subsurface flow paths of meltwater, ecohydrological controls on hydrochemistry, and interactions between snow and ice melt and changing precipitation regimes.

Chapter 4

Evaluating the Hydrological Response of a Tropical Glacierized Mountainous Watershed to Upslope Vegetation Migration

4.1 Introduction

Under warmer conditions, vegetation cover is expected to change, particularly in mountainous watersheds (Walther et al., 2005; Colwell et al., 2008; Feeley et al., 2011; Jump et al., 2012; Morueta-Holme et al., 2015; Pribulick et al., 2016), and this may affect hydrological processes by altering evapotranspiration (Neilson & Marks, 1994; Beniston, 2003; Goulden & Bales, 2014; Rasouli et al., 2019). Observations in mountain slopes across the world reveal that as temperature increases, it provides a suitable environment for plants growth in higher altitudes, resulting in an upslope migration of vegetation (Clow et al., 2003; Walther et al., 2005; Lenoir et al., 2008; Breshears et al., 2008; Morueta-Holme et al., 2015; Lamprecht et al., 2018). Vegetation lines have shifted upwards by an average 29.5 meters per decade altitudinally across mountains in Western

Europe (Lenoir et al., 2008). The same trend has been observed in tropical mountainous regions (Colwell et al., 2008; Chen et al., 2009; Feeley & Silman, 2010; Feeley et al., 2011; Morueta-Holme et al., 2015), with montane species migrating upslope by an average of 25–35 vertical meters upslope per decade (Feeley et al., 2011; Morueta-Holme et al., 2015).

In addition to altitudinal shift of vegetation lines in mountainous regions, warming also alters the composition of the montane vegetation in mountainous watersheds, such that plant communities with shallow-rooted high elevation species turn over to taller and deeper-rooted species (Huxman et al., 2005; Darrouzet-Nardi et al., 2006; Fadrique et al., 2018). This means that in the Andean páramos, which are high alpine grassland ecosystems, shallow-rooted plants such as cushion plants and herbaceous plants may be replaced with shrubs and tussock grass with deeper roots. Upslope migration of vegetation and conversion of shallow-rooted species to deeper-rooted species has the potential to reduce surface-water supply (Zhang et al., 2001; Beniston, 2003; Huxman et al., 2005; Darrouzet-Nardi et al., 2006; Goulden & Bales, 2014; Ochoa-Tocachi et al., 2016b; Rasouli et al., 2019), primarily through increase in evapotranspiration (Huxman et al., 2005; Zhang et al., 2001). Upslope migration of vegetation in temperate and humid mountainous regions may result in 7% to up to 26% reduction of stream discharge by increasing evapotranspiration (Goulden & Bales, 2014; Rasouli et al., 2019). One region that could be particularly susceptible to ecohydrological impacts of climate-driven vegetation shifts is the tropical Andes, because the fastest rates of warming in the world have been predicted in low latitudes and high altitudes (Bradley, 2006). However, there have been no previous studies that have evaluated the hydrologic response of tropical mountainous watersheds to changes in vegetation.

While there have been many studies in tropical glacierized mountainous watersheds on the impact of climate change on hydrology (Barnett et al., 2005; Ostheimer et al., 2005a; Bradley, 2006; Mark & Mckenzie, 2007; Baraer et al., 2009; Saberi et al., 2019; Somers et al., 2019), these have not considered the concomitant effects of vegetation change. The lack of studies on the impact of upslope migration of vegetation on hydrologic systems of tropical glacierized watersheds represents a major knowledge gap about these highly vulnerable systems. Hydrological impacts have important implications for

local communities who rely on the water from these catchments for domestic and irrigation purposes (La Frenierre, 2014). Hydrological processes in landscapes dominated by subsurface flow are particularly prone to change by alteration in vegetation distribution (Wilcox, 2002; Huxman et al., 2005). Several studies in tropical glacierized mountainous watersheds have found groundwater to contribute a notable fraction of stream discharge (Favier et al., 2008; Baraer et al., 2015; Minaya, 2016; Saberi et al., 2019), making these watersheds potentially highly susceptible to upslope migration of vegetation.

This study examines the hydrological response of a tropical glacierized mountainous watershed to the combination of climate and vegetation change. This study builds on our recent understanding of the hydrological response of a tropical glacierized mountainous watershed in the Ecuadorian Andes to climate change, where currently, glacier melt significantly contributes to the stream discharge (∼50%) (Saberi et al., 2019). We thus expect that stream discharge will decrease after glaciers fully retreat under warming temperatures, and that these effects will be exacerbated with the upslope migration of vegetation. We implemented a spatially distributed and physically based model that integrates watershed hydrology and reactive transport, BioRT-Flux-PIHM (Bao et al., 2017; Zhi et al., 2020) to address the following questions in a sub-humid, tropical glacierized watershed: 1) Will upslope migration of vegetation decrease stream discharge, and by how much? and 2) How do interactions among climate, vegetation, and hydrological processes control the changes in discharge?

4.2 Study Site Description

Volcán Chimborazo (6268 m a.s.l.), is a dormant glacierized volcano with its summit covered by a ∼55 m-thick ice cap (Ginot et al., 2002). Chimborazo's tropical climate is characterized by minimal interannual variability (∼2 °C) and noticeable variability in seasonal precipitation (La Frenierre, 2014). There are typically two wet seasons (February-May and October-November) that are separated by two drier seasons. During the June 2015 to June 2016 study period considered in this work, a strong El Niño event occurred from November 2015 to May 2016. In this part of the Andes, El Niño events generally bring drier and hotter than normal conditions (Vuille et al., 2000; Wagnon et al., 2001; Francou, 2003; Bradley et al., 2003; Vuille & Keimig, 2004;

Smith et al., 2008b), which can significantly enhance ablation due to the higher temperature (Wagnon et al., 2001; Favier, 2004; Francou, 2004; Veettil et al., 2014a). Records from 1986 to 2011 show a local temperature increase of 0.11 °C /decade around Volcán Chimborazo (Vuille et al., 2008), which resulted in 21% reduction in ice surface area during this time (La Frenierre & Mark, 2017). Our study focuses on the 7.5 km^2 Gavilan Machay sub-catchment on the sub-humid northeast flank of Chimborazo. Gavilan Machay has an altitude range of 3800 to 6268 m a.s.l. and is currently 34% covered by the Reschreiter Glacier (Figure 4.1). We previously showed that stream discharge from Gavilan Machay may contain up to ∼50% glacier melt (Saberi et al., 2019), which has significant implications for the people living in the agrarian communities at the foot of the mountain, as the glaciers continue to retreat.

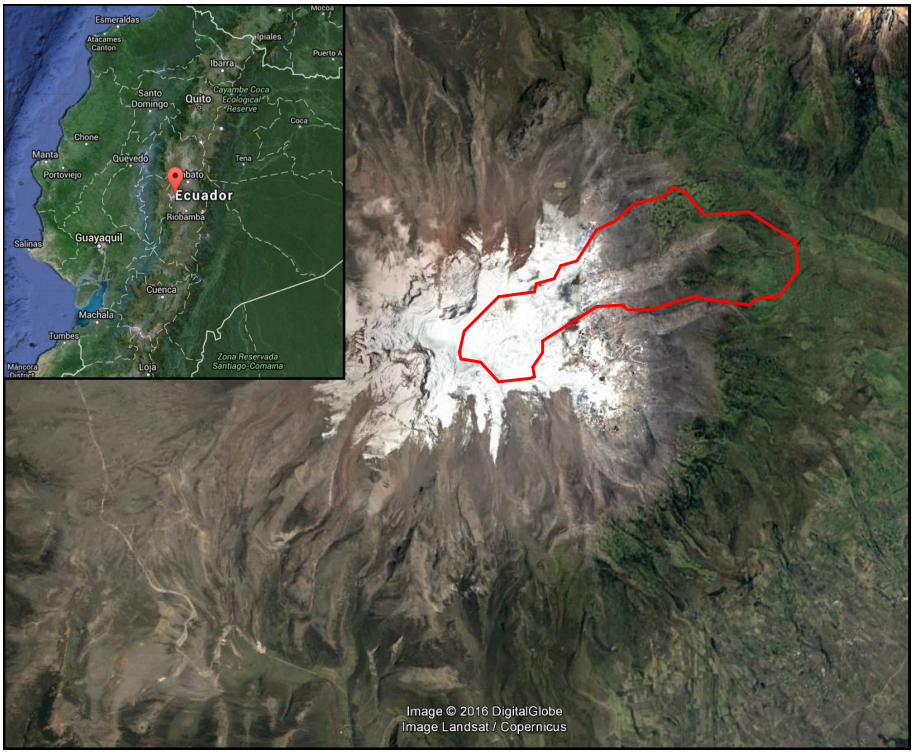

Figure 4.1: Satellite image of Volcán Chimborazo, with the Gavilan Machay watershed outlined in red, and its location in Ecuador shown in the insert map.

Volcán Chimborazo is predominantly covered with "páramo" grasslands, which are native to the high-elevation tropical Andes, occupying habitats between 3000 and 4700

m a.s.l. (Lauer, 1981). Páramo is composed of many different types of vegetation and exhibits different climate, soil, and hydrology at local scales (Luteyn & Balslev, 1992). As a high-elevation ecosystem, the páramo is adapted to low atmospheric pressure, intense solar radiation, and the drying effect of wind (Cuatrecasas, 1968). The páramo has high plant diversity (>5,000 species), including bunchgrasses (*Calamagrostis* and *Festuca*), shrubs, tussock grass, giant rosettes, and small mat-forming plants such as lichens, cushion plants, ground rosettes (Luteyn & Balslev, 1992). Elevation is the main driver of páramo vegetation, resulting in an internal vertical structure with three main altitudinal belts: the subpáramo, páramo, and superpáramo (Cuatrecasas, 1968). The subpáramo sits above the upper Andean forest and usually contains shrubs, small trees, and tussock grasses. Generally, spanning from 3500 to 4500 m a.s.l., the páramo is dominated by shrubs, tussock grass, and trees along the stream. At about 4400 to 4500 m a.s.l., the páramo transitions into sparsely vegetated conditions, primarily dominated by mosses and bare soil, until glaciers or permanent snow is reached.

The primary geology of Chimborazo consists of layered lava and pyroclastic flows, overlaid by thick ash deposits (Barba et al., 2008; Samaniego et al., 2012). Páramo soils are rich in organic matter and can be characterized by their high infiltration rates and water storage capacity, which are considered to be key in sustaining river discharge throughout the year (Podwojewski et al., 2002; Buytaert et al., 2006). The Gavilan Machay soil and bedrock is predominantly composed of reactive aluminosilicate minerals including felspars, pyroxenes, and amphiboles (Saberi et al., 2020). Weathering of these minerals results in Na^{+}, Ca^{2+}, Mg^{2+} comprising the major ions found in the stream water (Saberi et al., 2020).

4.3 Vegetation Shift Analysis

To assess upslope migration of the vegetation line and vegetation composition in Gavilan Machay watershed, we developed a land cover classification map based on the most recent publicly available imagery from 2011. We then compared the newly developed map with a 1978 historical land-cover map to estimate the recent vegetation migration rate.

4.3.1 Land-Cover Classification

Object Based Image Analysis (OBIA) was applied to remote sensing data to develop a land cover classification map for the Gavilan Machay watershed. The OBIA technique involves a preliminary image segmentation step in which pixel-based features are used to produce statistically homogeneous image objects (Benz et al., 2004). The image objects, also known as geo-objects, are then classified as land cover classes based on their spectral, textural, and shape attributes (Burnett & Blaschke, 2003; Hay & Castilla, 2008). The Cognition Network Language (CNL) within the software package eCognition Developer version 9.0 by Trimble was used for the work.

4.3.1.1 Data Retrieval and Pre-eCognition Processing

OBIA analysis was conducted using high-resolution (30 cm) orthorectified digital aerial photography containing four multispectral bands (red, green, blue, and near infrared), vector layers delineating the 2013 extent of clean and debris-covered ice and stream line (La Frenierre & Mark, 2017), and a 3-meter Digital Terrain Model (DTM). The high resolution orthophoto, collected between March and October 2011 at Volcán Chimborazo, was obtained from the Sistema Nacional de Información de Tierras Rurales e Infrastructura Tecnológica (SIGTIERRAS: http://www.sigtierras.gob.ec/descargas/) initiative of the Ecuadorian Ministry of Agriculture, Livestock, Aquaculture and Fisheries. The high resolution DTM was created by SIGTIERRAS using the orthophotos (http://www.sigtierras.gob.ec/descargas). ERDAS imagine software was used to create a mosaic of the aerial photography and DTM.

4.3.1.2 Development of eCognition Rule Set

Land cover classification in eCognition is based on an iterative process of segmentation and classification (O'Neil-Dunne et al., 2013), with the goal of achieving the highest level of accuracy of the desired land cover classes. In segmentation, the spectral similarities of neighboring pixels are used to define image objects. Different types of segmentation algorithms with parameters such as shape, weight, and compactness can be used to create image objects. Additionally, vector layers, also referred to as thematic layers, can be used during this step to create image objects outlining features such as lakes and

streams. Classification is implemented based on sets of characteristics including geometry, Normalized Difference Vegetation Index (NDVI), and slope defined for each image object. A simple classification method based on defining multiple feature thresholds (e.g., 4200 m a.s.l. $<$ elevation $<$ 4400 m a.s.l. & $0.0163 <$ NDVI < 0.018) was used in this study to classify the objects.

The set of segmentation and classification algorithms used to produce a classified image is referred to as a rule set. In order to develop the rule set for this study, the orthophoto and the DTM of the region were used to generate an NDVI and a slope raster layer. The NDVI layer was used primarily for identification of vegetation-covered areas versus barren areas. Two vector layers delineating the clean and debris-covered ice were used to classify the ice-covered areas. The final rule set involves three levels of segmentation and classification for identifying nine land cover types (clean ice, debris-covered ice, trees and shrubs, stream, pond, grassy páramo, mixed páramo, upper páramo, and moss-rock). Field observations of altitudinal vegetation distribution in the watershed were incorporated in the level 2 segmentation of the classification. Figure 4.2 illustrates the entire land cover classification process that we developed with the eCognition Software.

4.3.2 Updated Land-Cover Classification

Figure 4.3a shows the resulting land cover classification map for Gavilan Machay watershed from our eCognition rule set. The results were verified using observations and plants sampling points from the field. We aimed to classify semi-permanent land-cover types over the entire watershed, yet it should be noted that the extents of the ponds can be highly dynamic throughout the year. The páramo ecosystem in Gavilan Machay catchment is divided into three zones based on our field observations and land cover classification: grassy páramo (Figure 4.3b), mixed páramo (Figure 4.3c), and upper páramo (Figure 4.3d). The rest of the non-glacierized catchment is composed of rocks, cushions, and mosses, which we called the moss zone (Figure 4.3e). The grassy páramo, which sits below 4200 m a.s.l., is dominated by tussock grass. The mixed páramo, which spans the watershed between 4200 - 4400 m a.s.l., primarily contains dwarf shrubs and shrubs, with a few trees along the stream. Above the grassy páramo lies the upper páramo, which is composed of dwarf shrubs, herbaceous plants and sedges, and mosses.

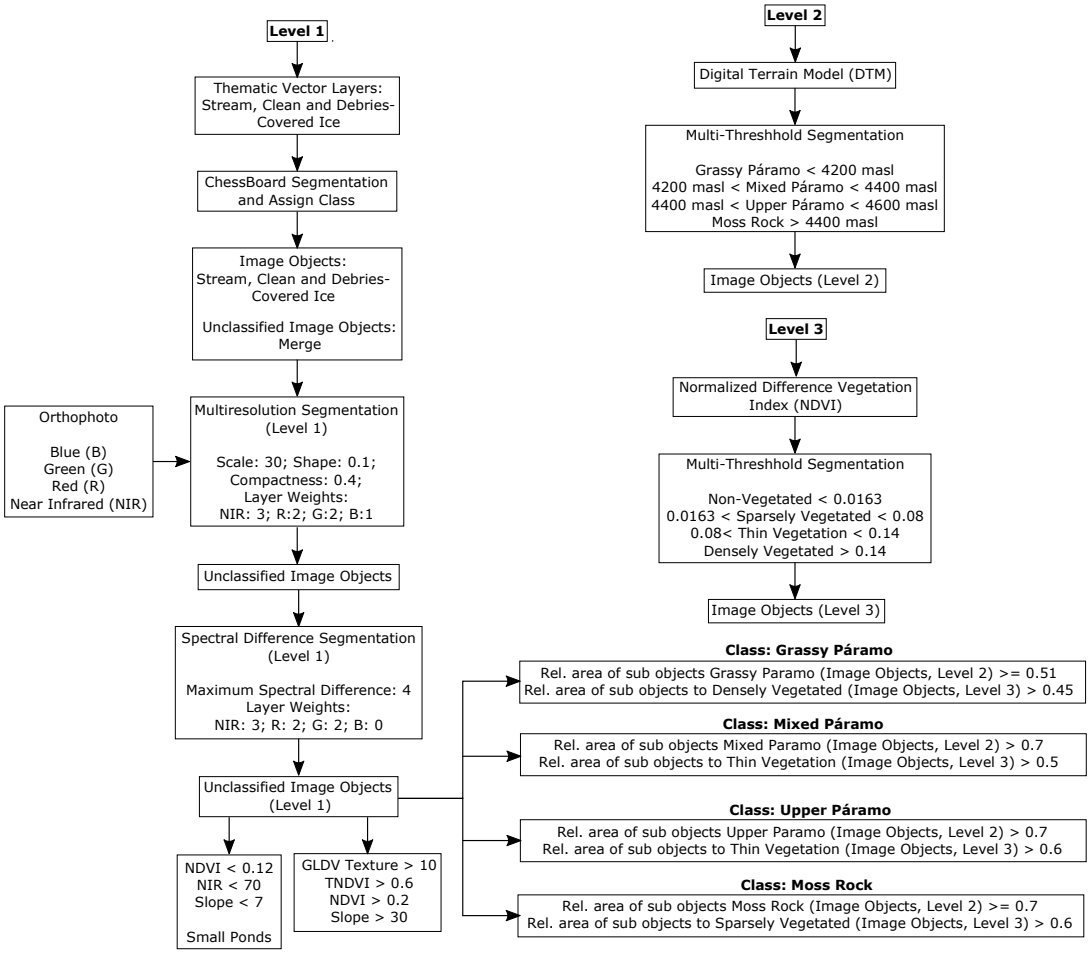

Figure 4.2: Flowchart representing the workflow for segmentation and classification applied in the eCognition Software to develop the land cover classification map for Gavilan Machay watershed, Volcán Chimborazo.

The rest of the catchment, if not covered with ice, is dominated by bare soil, mosses, cushions, and lichens. The plant composition of the classes with vegetation is described in detail in Table 4.1.

Land Cover Type	**Altitudinal Range**	**Dominant Growth Forms (Species)**
Grassy Páramo (Pajonal Paramuno)	<4200 m a.s.l.	• Tussock Grass (*Calamagrostis species*)
Mixed páramo (Pajonal Arbustivo)	4200 to 4400 m a.s.l.	• Tussock Grasses (*Calamagrostis sp.* and *Stipa sp.*) • Shrubs (*Hypericum sp., Diplostephium sp., Baccharis sp., Chuquiragua sp.,* and *Loricaria sp.*) • Trees (*Gynoxys sp.* and *Polylepis sp.*) • Herbaceous Plants (*Acaena sp., Arenaria sp., Castilleja sp.,* and *Lachemilla sp.*) • Cushions (Plantago rigida, and *Azorella sp.*) • Mosses (*Racomitrium sp.* and *Breutelia sp.*)
Upper Páramo (Superpáramo)	4400 to 4600 m a.s.l.	• Cushions (*Plantago sp., Azorella sp.,* and *Distichia sp.*) • Sedges and Grasses (*Carex sp, Festuca sp.,* and *Calamagrostis sp.*) • Herbaceous Plants (*Senecio sp., Werneria sp.,* and *Lachemilla sp.*) • Mosses (*Racomitrium sp.,* and other *Grimmiaceae*)
Moss zone (Zona de Musgos)	>4600 & Non-glacierized	• Mosses (*Racomitrium sp., Andreaea sp.,* and *Polytrichastrum sp.*) • Lichens (*Bryoria sp.,* and *Rhizocarpon sp.*) • Cushions (*Azorella sp.*) • Acaulescent rosettes (*Senecio sp.*)

Table 4.1: Plant composition of each land cover class not covered by ice identified in Gavilan Machay watershed at Volcán Chimborazo.

4.3.3 Upslope Migration of Vegetation

A digitized version of the land-cover map developed in 1978 for this region by the Ecuadorian Department of Geography (Departamento de Geografia) is shown in Figure

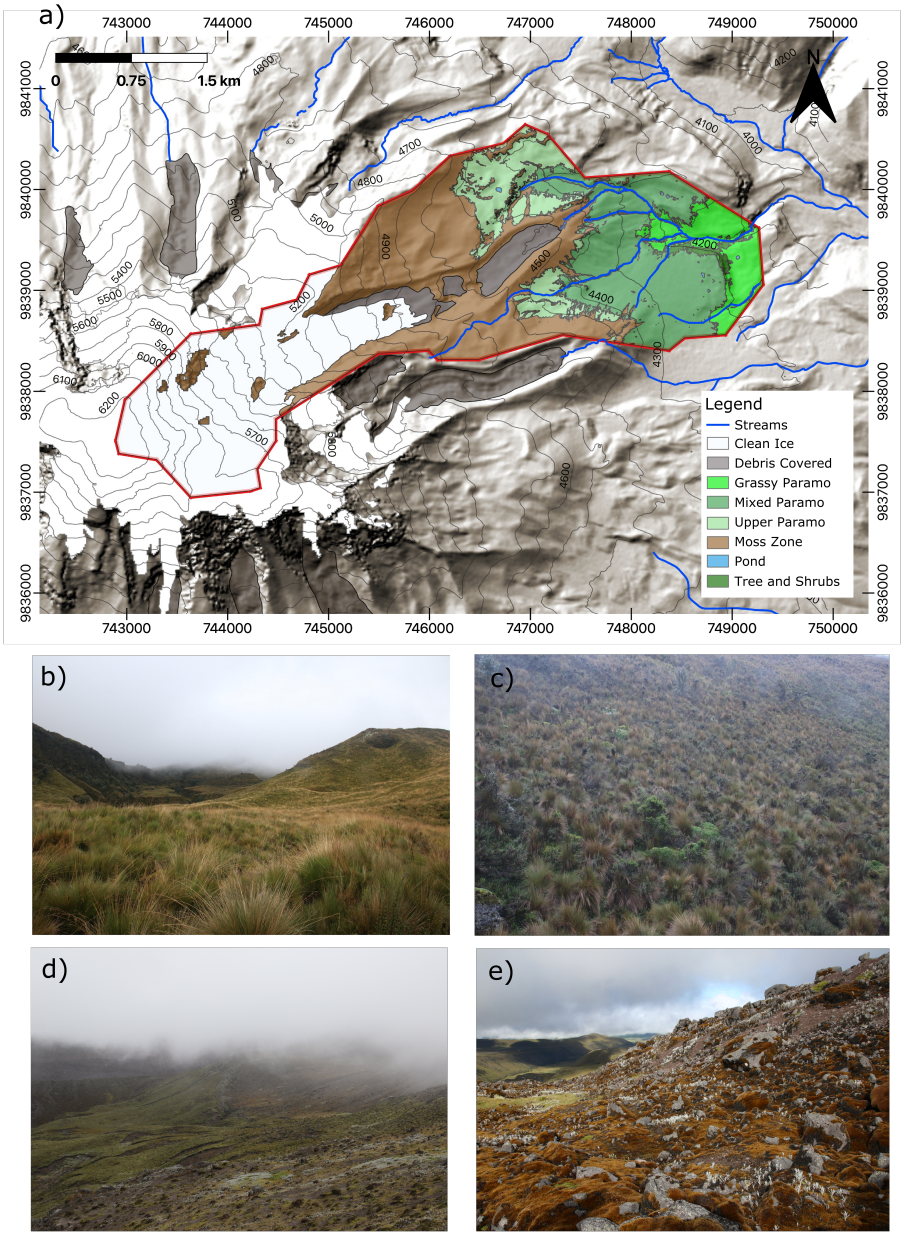

Figure 4.3: (a) Updated land cover classification using OBIA approach. We consider the vegetation line to be the transition from Upper Páramo to Moss Zone. The Gavilan Machay watershed is divided into nine different land cover classes. Photos represent the main classes, including (b) Grassy Páramo, (c) Mixed Páramo, (d) Upper Páramo, and (e) Moss Zone in Gavilan Machay catchment at Volcán Chimborazo.

4.4. This land cover map is based on land surveys conducted from 1976 to 1978, landsat images, and topographic data from the Instituto Geográfico Militare del Ecuador (IGM). Although this map was developed through a different procedure and includes somewhat different classes than those defined in the updated land cover map, it is still possible to qualitatively approximate upslope migration of the vegetation line between 1978 and 2011 by comparing the two land cover maps. In the 1978 map, we considered the transition from "Perennial bunchgrass" to "Sand/Gravel" to be the vegetation line, and in the 2011 map, we considered the transition from "Upper Páramo" to the sparsely vegetated "Moss Zone" to be the vegetation line.

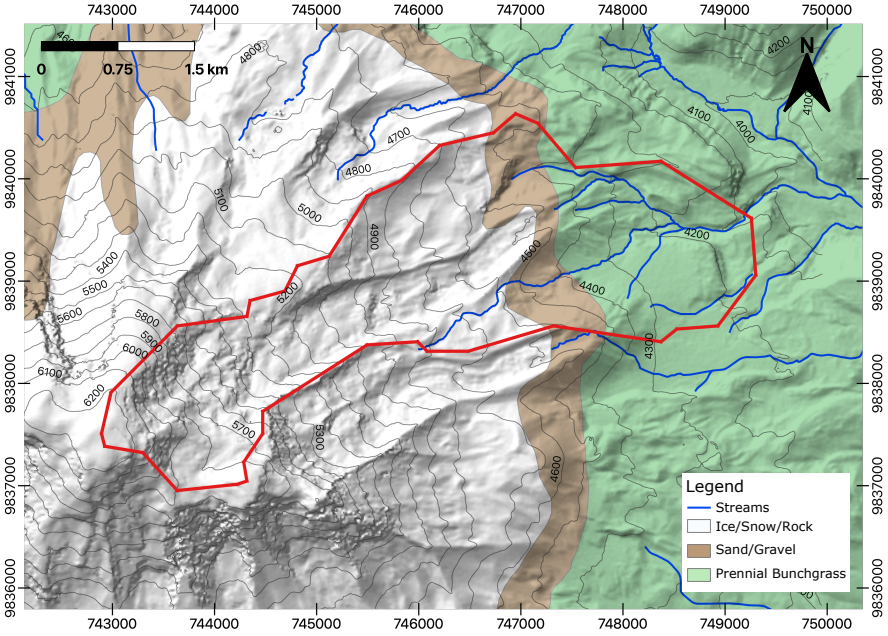

Figure 4.4: 1978 land cover classification for the Volcán Chimborazo, with the Gavilan Machay watershed outlined in red. This classification was developed by the Ecuadorian Department of Geography based on land surveys conducted between 1976-1978 and topographic data from the Instituto Geográfico Militare del Ecuador (IGM) and was digitized by La Frenierre (2014). We consider the vegetation line to be the transition from Perennial Bunchgrass to Sand/Gravel.

The upper elevation limit migration of vegetation from 1978 to 2011 is shown in Figure 4.5. The limit of vegetation appears to have moved upslope by approximately 1.5

to 150 meters in elevation, depending on the location in the watershed, which is equivalent to up to 45 m/decade. Morueta-Holme et al. (2015) found more than 500 meters of upslope vegetation migration from 1802 to 2012 on the southeast slope of Volcán Chimborazo. This equates to a conservative average of 24 m/decade, although it is likely that most of the migration occurred in more recent decades that have experienced accelerated warming.

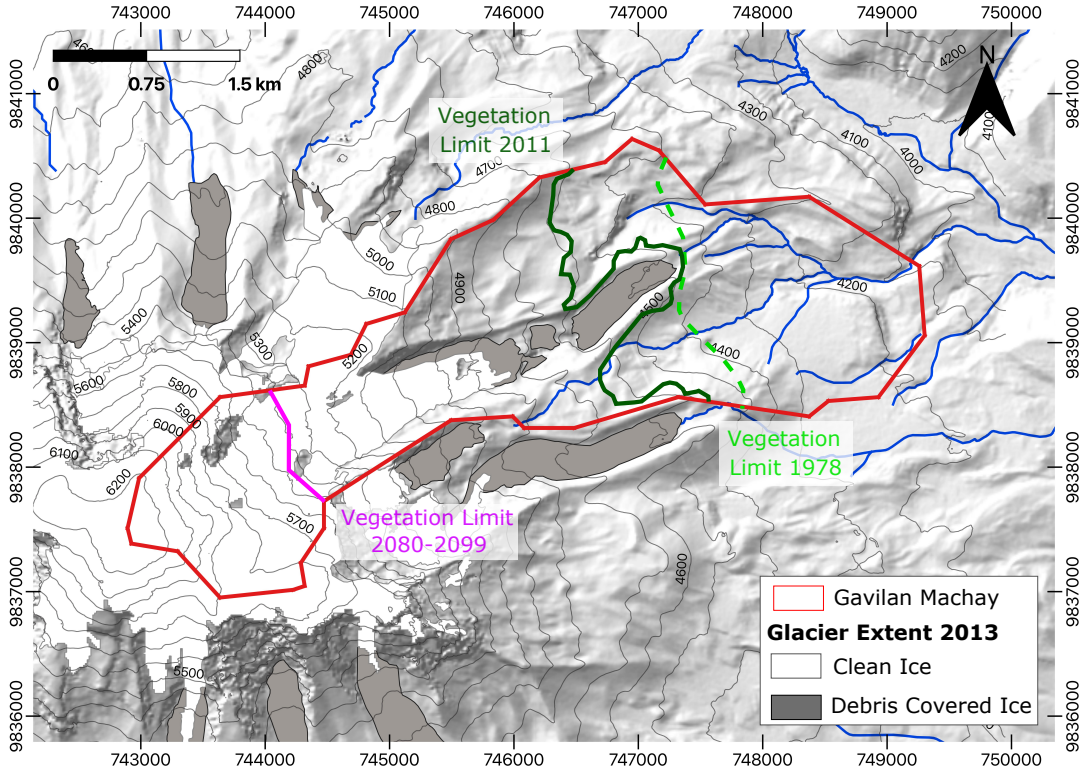

Figure 4.5: Comparison of 1978 (dashed line) and 2011 (solid line) boundaries of vegetation limit on Chimborazo. The upper limit of vegetation migrated upslope from 1.5 to 150 meter within the Gavilan Machay watershed. The projected vegetation line for 2088-2099 is shown with the pink line.

The estimated upslope migration rates from both our land cover map comparison and the analysis by Morueta-Holme et al. (2015) on Volcán Chimborazo are higher than the reported median of 11 m/decade across plant species worldwide (Chen et al., 2011). This larger shift at Chimborazo is most likely linked to higher rates of warming in the

tropical Andes compared to the global average (Bradley, 2006) as well as decrease in precipitation in the area, which contributes to glacier recession (La Frenierre & Mark, 2017; Morueta-Holme et al., 2015).

We expect that potential future vegetation shifts in Gavilan Machay will depend on changes in temperature. For the northern part of South America, the latest climate projection scenarios predict an increase in temperature between 3±1.5 °C for 2080-2099 (IPCC, 2007). Following the approach of Feeley et al. (2011) to predict the corresponding vegetation shift, we assume that temperature will increase uniformly over the entire watershed, and that the future vegetation line and spatial distribution will follow its current-day relationship with the temperature. This allows us to apply the current temperature lapse rate (0.7 °C with 100 m) with a projected 4.5 °C increase in air temperature to estimate that vegetation will shift upslope by about 650 m in the future (Figure 4.5).

It is possible that the future vegetation line shift may be even greater than we projected, because warmer temperatures and greater evapotranspiration will produce higher humidity, and this is expected to lower the temperature lapse rate (Buytaert & Beven, 2011). This would result in even stronger warming at higher altitudes than expected with the current temperature lapse rate (Urrutia & Vuille, 2009), which may lead to even farther upslope migration of the vegetation line.

Beside the possibility of all plant types shifting upslope by 650 m, previous studies indicate that warming may result in shallow-rooted high elevation plants to be replaced by taller-stature and deeper-rooted species from lower elevations (Huxman et al., 2005; Darrouzet-Nardi et al., 2006; Fadrique et al., 2018). On Chimborazo, this could correspond to tussock grasses that are currently prevalent at lower elevations (Grassy Páramo in Figure 4.3) replacing lower-statured and shallower-rooted species within the Upper Páramo class. On the southeast slope of Chimborazo, Morueta-Holme et al. (2015) found most plant taxa to be shifting upslope, but with differences in movement among species. Although tussock grass was observed at higher elevations than historically noted, most of its expansion was actually into lower elevations, possibly because of land-use practices or changes in atmospheric nitrogen deposition. Although the possibility of upslope encroachment of tussock grass is unknown, we also consider a future condition with deeper-rooted tussock grass distributed up to the vegetation line, in order

to assess a more extreme scenario in terms of potential ecohydrological impacts.

Hydrological consequences of the projected upslope shift in vegetation - all plant types and with tussock grass encroachment - are evaluated using the watershed model described next in Section 4.4.

4.4 Model Description

4.4.1 BioRT-Flux-PIHM

BioRT-FluxPIHM is a spatially distributed and physically based watershed model consisting of three modules: a land-surface interaction Flux module (Ek et al., 2003; Shi et al., 2013), a hydrologic PIHM module (Qu & Duffy, 2007), and a multi-component biogeochemical reactive transport module (Bao et al., 2017; Zhi et al., 2020). To implement the model, the PIHMgis software (Bhatt et al., 2014) was used to discretize the watershed into triangular grid cells based on the topography. Channel routing and overland flow in the model are determined using 1D and 2D St. Venant equations. Subsurface flow in the unsaturated and saturated zones of each cell are calculated using 1D and 2D forms, respectively, of Richards equation. Potential evapotranspiration in the model is calculated using a modified form of Penman Monteith equation, which depends on meteorological inputs, albedo, and surface roughness (Mahrt & Ek, 1984). Actual evapotranspiration in the model is determined from potential evapotranspiration and comprises three components: soil evaporation, canopy transpiration, and canopy evaporation. Full details about Flux-PIHM can be found in Qu & Duffy (2007). In the following, we provide further information about evapotranspiration calculations, because the effects of vegetation shifts occur mainly through these processes.

Soil evaporation in the model is estimated through the following equation:

$$E_{soil} = E_p(1 - \sigma_f)(\frac{\theta_1 - \theta_w}{\theta_{ref} - \theta_w}) \tag{4.1}$$

where σ_f is the green vegetation fraction, θ_1 is the simulated soil moisture in top layer, θ_{ref} is the soil field capacity, θ_w is the soil wilting point, and E_p is the potential evapotranspiration. θ_w and θ_{ref} are calculated based on van Genuchten parameters.

Canopy evaporation in the model is simulated through:

$$E_c = E_p \sigma_f (\frac{W_c}{W_{cmax}})^{f_{xc}} \tag{4.2}$$

where W_c is the simulated storage for canopy interception, W_{cmax} is the maximum canopy water capacity, and f_{xc} is the canopy evaporation coefficient, which is set by default to 0.5. W_{cmax} changes seasonally and is a function of leaf area index (LAI):

$$W_{cmax} = S.LAI \tag{4.3}$$

where S is the reference canopy water capacity (set as 0.2 mm).

Canopy transpiration in the model is determined through:

$$E_t = E_p \sigma_f B_c (1 - \frac{W_c}{W_{cmax}})^{f_{xc}} \tag{4.4}$$

B_c is calculated using:

$$B_c = \frac{1 + \frac{\Delta}{\gamma+1}}{1 + R_c C_h + \frac{\Delta}{\gamma+1}} \tag{4.5}$$

where Δ is the rate of change of saturation specific humidity with air temperature, γ is the psychrometric constant, R_c is the canopy resistance, and C_h is the surface exchange coefficient for heat and moisture (which depends on surface roughness). Canopy resistance in the model is a function of minimum stomatal resistance, LAI, and four factors, F_1, F_2, F_3, and F_4, each of which represents the effects of solar radiation, vapor pressure deficit, air temperature, and soil moisture, respectively:

$$R_c = \frac{R_{cmin}}{LAI.F_1F_2F_3F_4} \tag{4.6}$$

R_{cmin} is the minimum stomatal resistance (depends on vegetation type), and F_1, F_2, F_3, and F_4 are estimated through equations 4.7 to 4.10, respectively:

$$F_1 = \frac{\frac{R_{cmin}}{R_{cmax}} + f}{1 + f} \quad where \quad f = 1.1 \frac{S}{R_{gl}.LAI} \tag{4.7}$$

(where R_{cmax} is the maximum stomatal resistance (5000 s/m), S is the downward solar radiation, and R_{gl} is the reference visible solar radiation, which primarily depends on the type of vegetation),

$$F_2 = \frac{1}{1 + h_s(q_s - q)} \tag{4.8}$$

(where h_s is the water vapor exchange coefficient, q_s is the saturation specific humidity, and q is the specific humidity of the air),

$$F_3 = 1 - 0.0016(T_{ref} - T_a)^2 \tag{4.9}$$

(where T_{ref} is the reference temperature (24.85 °C) and T is the air temperature), and

$$F_4 = \sum_{i}^{N_{root}} \frac{(\theta_i - \theta_w)d_{zi}}{(\theta_{ref} - \theta_w)d_{root}} \tag{4.10}$$

(where θ_i is the simulated soil moisture at layer i, θ_{ref} is the soil field capacity, θ_w is the soil wilting point, d_{zi} is the depth of soil layer, and d_{root} is the total depth of root zone). In the above evapotranspiration equations, soil moisture in different layers and canopy water storage are dynamically simulated model states, meteorological variables are time-varying inputs, and all other variables are inputted as vegetation or soil parameters.

4.4.2 Model Setup

4.4.2.1 Soil Parameter Calibration

The soil hydraulic properties for different soil zones, which were spatially distributed along the elevations based on the mapped land-cover zones, were calibrated using both hydrological and hydrochemical observations. The calibrated soil hydraulic parameters included horizontal and vertical hydraulic conductivity, porosity, and van Genuchten water retention curve parameters. Details on the calibration are provided in Saberi et al. (2020).

4.4.2.2 Vegetation Parameterization

Land cover types in the model are represented and linked to hydrological and land surface processes through parameters such as green vegetation fraction, rooting depth, leaf area index, albedo, and surface roughness. We developed a new set of PFT parameterizations corresponding to the páramo categories in our land-classification map (Table 4.2, Figure 4.3) based on field observations of vegetation during August 2018 and January 2019 and literature descriptions of páramo systems. Because many of the land classes comprise multiple plant forms, for the parameter values, we implemented abundance-weighted averages over the different plant forms. Whenever possible, we built off parameter values for pre-existing Flux-PIHM PFTs that most closely resemble our páramo plant forms. Some páramo plant forms, such as moss, sedges/herbaceous plants, and shrubs, correspond with pre-existing PFTs in FluxPIHM. Cushion plants (e.g. *Azorella spp., Plantago rigida, Distichia spp*) and acaulescent rosettes (e.g. *Senecio spp*) have no direct equivalent in pre-existing PFTs, and so we implemented the pre-existing "dwarf shrub" parameter values as closest approximations in stature and physiology. For tussock grass, we started with the pre-existing grassland PFT and made with the modification of increased stomatal resistance and roughness to reflect the tall, tough leaves that characterize tussock grass, including *Calamagrostis* and similar genera. Plant form abundances for the new PFT categories were based on in situ surveys of relative cover as well as published classifications of Ecuadorian páramos (Beltrán et al., 2009; Minaya, 2016). Mixed páramo ("Pajonal arbustivo altimontano paramuno") contains a mix of tussock grass, low shrubs, cushion plants, and other low-statured vegetation, and we parameterized this as 30% shrub, 30% grass, 20% dwarf shrub, and 20% moss. Because trees and shrubs cover only a very small area along streams around the grassy páramo and mixed páramo transition (Figure 4.3), these areas were coded under the mixed páramo class for the model implementation. Upper páramo ("Matorrales Edafoxerófilos en Cojín Altoandinos Paramunos") is even lower in stature, and we implemented this as 40% dwarf shrub, 35% sedge/herbaceous plants, and 25% moss. Lastly, the Moss zone ("Vegetación subnival") is sparsely vegetated and primarily moss and lichen-dominated, with some cushion plants and acaulescent rosettes, and it is parameterized as 20% dwarf shrub, 20% moss, and 60% barren (Flux-PIHM has a pre-existing "barren" land-cover

PFT). For the ice-covered zone, we implemented the pre-existing Perennial Ice and Snow land-cover class.

The vegetation parameterization in this study is more detailed than what was implemented in Saberi et al. (2019) and Saberi et al. (2020), which enables us to evaluate different vegetation shift scenarios in the watershed.

	$SHDFAC$	D_{root}	R_S	R_{gl}	LAI_{min}	LAI_{max}	$EMISS_{min}$	$EMISS_{max}$	ALB_{min}	ALB_{max}	$Rough$
Grassy Parámo	0.8	0.7	150	80	0.52	4	0.92	0.96	0.19	0.23	0.04
Mixed Parámo	0.71	0.61	177	94	0.71	0.35	0.93	0.95	0.2	0.27	0.04
Upper Parámo	0.64	0.43	92	100	1.17	4.07	0.94	0.95	0.17	0.23	0.04
Moss Zone	0.27	0.22	641.4	639.4	0.46	1.65	0.91	0.92	0.31	0.34	0.04

Table 4.2: $SHDFAC$ (σ_f): green vegetation fraction (m^2/m^2), D_{root}: rooting depth (m), R_S: minimum stomatal resistance (s/m), R_{gl}: parameter used in radiation stress function (W/m^2), LAI_{min}: minimum leaf area index through the year (m^2/m^2), LAI_{max}: maximum leaf area index through the year (m^2/m^2), $EMISS_{min}$: minimum background emissivity through the year (-), $EMISS_{max}$: maximum background emissivity through the year (-), ALB_{min}: minimum background albedo through the year (-), ALB_{max}: maximum background albedo through the year (-), $Rough$: Manning's roughness coefficient ($s/m^{(-1/3)}$).

4.4.2.3 Model Scenarios

The BioRT-Flux-PIHM model was run for three change scenarios, relative to a "Base case" representing current conditions, to differentiate the individual and combined effects of full retreat of glaciers, increase in air temperature, upslope migration of all vegetation types, and upslope vegetation migration with tussock encroachment. Specifically, the effects of changes in climate and vegetation on hydrological variables were evaluated under 1) future conditions with total glacier depletion, warming by 4.5 °C according to projections of temperature increase for the tropical Andes (IPCC, 2007), and unchanged vegetation distribution ("NoGlacier+ΔT"); 2) future conditions with total glacier depletion, 4.5 °C warming, and 650 m upslope shift of all vegetation types (specifically, land cover classes below our designated vegetation line: Grassy Páramo, Mixed Páramo, and Upper Páramo) corresponding to the increase in temperature ("+AllPlantsUp"); and 3) future conditions with total glacier depletion, 4.5 °C warming, and 650 m upslope vegetation migration with tussock grass encroachment, such that the entire vegetated area

(defined as the area below the vegetation line) is covered with tussock grass ("+TussockUp). In all the scenarios without glaciers, the areas above the vegetation line are covered with the "Moss Zone" PFT. The "Base case" scenario uses meteorological inputs from June 2015 to June 2016. For the change scenarios, we applied an additive 4.5 °C air temperature increment to the same June 2015-June 2016 meteorological inputs, because of the major challenges and consequent uncertainties in spatially downscaling climate model simulations in very high relief settings (Buytaert et al., 2010). The model was run in a spin-up mode until stream discharge and aqueous species reached a steady state such that they did not change with time. The Base case and three change scenarios are conceptualized in Figure 4.6 to show the applied changes in vegetation and glacier for each scenario, which are summarized in Table 4.3.

Temperature	**Vegetation**	**Glacier Melt**	**Notation**
Current	Current	Current	Base
+4.5 °C	Current	None	NoGlacier+ΔT
+4.5 °C	Upslope Migration of All Vegetation Types	None	+AllPlantsUp
+4.5 °C	Upslope Migration with all Tussock Grass	None	+TussockUp

Table 4.3: Description of the four cases of change in climate, glacier, and vegetation.

4.5 Results and Discussion

By comparing the simulated scenarios of temperature, glacier, and vegetation change with the "Base case", we evaluated both individual and combined impacts of these changes on the hydrology of the watershed. Our assessment focused on simulated responses in stream discharge and evapotranspiration in the watershed.

4.5.1 Stream Discharge

Stream discharge and groundwater flux in Gavilan Machay are highly sensitive to changes in precipitation and glacier meltwater input to the watershed. Assuming no changes in precipitation or vegetation, simulated stream discharge was reduced by 58% from the Base case when glacier melt was removed and temperature was increased by

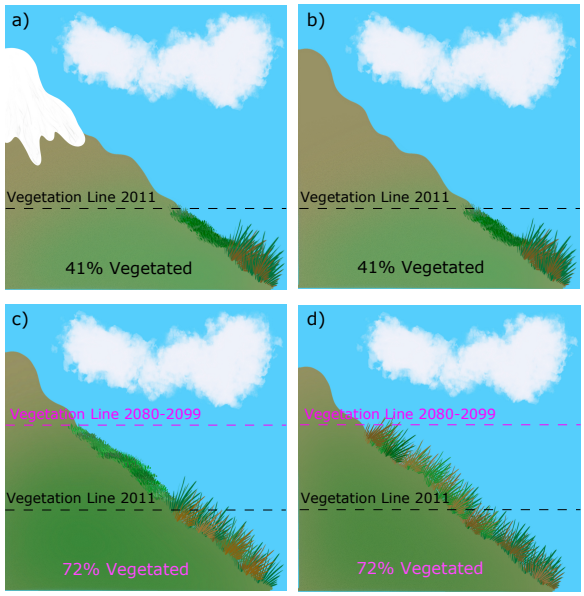

Figure 4.6: Schematic illustration of the vegetation and glacier cover under the a) Base case, b) NoGlacier+T scenario, c) +AllPlantsUp Scenario, and d) +TussockUp scenario.

4.5 °C. The glacier removal alone led to a 52% reduction in stream discharge (Saberi et al., 2019, 2020), while the additional 4.5 °C warming and associated increase in ET only added on a further reduction of 6% from the Base case. This result indicates that an increase in temperature without expansion of vegetation will not significantly impact ET and the overall water budget. Adding upslope migration of vegetation and tussock grass encroachment to the glacier melt removal and 4.5 °C warming reduced stream discharge by 74% and 78% relative to the Base case [Figure 4.7a and b]. The additional 16% and 20% further reduction (from the Base case) in stream discharge imposed by upslope migration of vegetation and tussock encroachment results in no-flow or very low-flow conditions, particularly during El Niño months (November-January), when precipitation is lowest and evapotranspiration is the highest. This poses a major problem for agrarian communities who depend on this water for irrigation. The comparison of the simulated stream discharge in NoGlacier+ΔT and +AllPlantsUp scenarios highlights the importance of including changes in vegetation in addition to increase in temperature in future water availability predictions.

It has been previously noted in the Sierra Nevada Mountains (California) that the

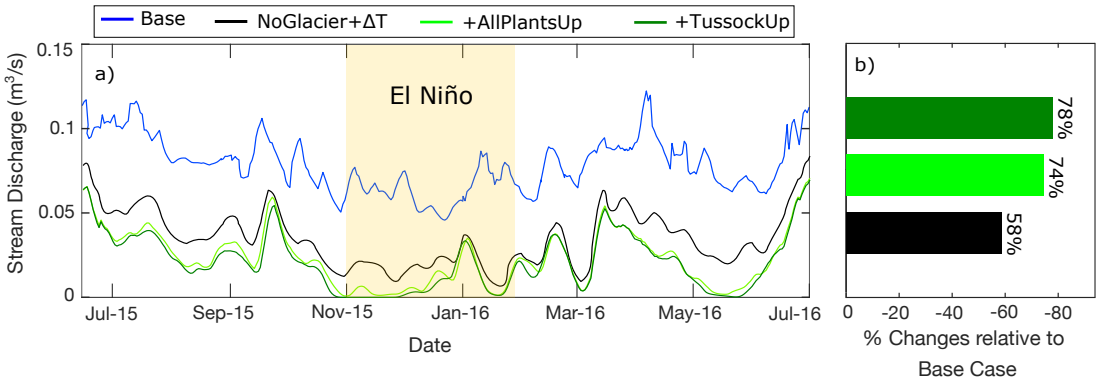

Figure 4.7: (a) weekly moving average time series of simulated stream discharge. The blue line represents the scenario with melt, black line the scenario without glacial melt, light green the scenario with all plants shifting upslope, and dark green the scenario with tussock encroachment. (b) Percent changes of stream discharge compared to Base case for the scenario without glacial melt in black, scenario with all plants shifting upslope in light green, and the scenario with tussock encroachment in dark green.

hydrological impacts of climate change on mountain slopes have been underestimated when changes in vegetation are not represented (Goulden & Bales, 2014). In modeling studies in the Sierra Nevada Mountains (which is not glacierized), ET was predicted to increase by only 5% with a 4.1 °C increase in temperature when the plant distribution was expected to remain static (Miller et al., 2003), and this ET increase dramatically rose to 28% when upslope vegetation migration was also considered, leading to a notable 26% reduction in stream discharge relative to current conditions (Goulden & Bales, 2014). We saw a similar trend with even greater changes in our simulations in Gavilan Machay. Comparing against a scenario with no glaciers and current temperatures (like the Sierra Nevada case), a 4.5 °C increase in temperature results in 21% higher ET and 6% lower stream discharge for constant vegetation, and adding upslope migration of vegetation leads to 47% higher ET and 22% lower stream discharge. Our analysis shows that the vulnerability of montane hydrologic systems to upslope migration of vegetation and increase in temperature, which was previously noted for the Sierra Nevada Mountains, may extend to other regions of the world.

The relatively minor hydrological impact of tussock grass encroachment compared

to the scenario of all plants shifting upslope in Gavilan Machay was somewhat unexpected, given previous studies in North America that found that woody plant encroachment may have a substantial impact on ET (e.g., 30% increase in the Chihuahuan Desert, Schreiner-McGraw et al. (2020)) and stream discharge (e.g., 27% decrease in the Northern Canadian River Basin, Starks & Moriasi (2017)). In the case of woody plant encroachment, substantial increases in T/ET are expected when woody plants replace more shallow-rooted plants with smaller leaf areas, and specifically in places with large subsurface flows to streams, this would significantly decrease stream discharge (Huxman et al., 2005). In Gavilan Machay, the simulated effect of tussock grass encroachment is likely more subtle, because the difference in rooting depth with the smaller-statured plants it replaces is small (<30 cm difference, see Table 4.2) compared to the rooting depth differences with woody plant encroachment (Knoop & Walker, 1985). However, as further discussed below, our results depend strongly on the model parameterizations of ET, and while we formulated new PFT classifications based on in situ surveys and páramo literature descriptions (Section 4.4.2.2), it is possible that they do not fully capture unique physiological characteristics of páramo plants. Further work to develop parameters for individual páramo PFTs may lead to improved constraints on the ecohydrological effects of upslope vegetation migration and tussock grass encroachment.

Further model tests indicate that the notable predicted decrease in discharge in Gavilan Machay with upslope vegetation migration occurs only in combination with a temperature increase. Simulations with the cooler Base case temperatures show a sharp decline in ET above ∼4600 m a.s.l., even when plants are shifted upslope to ∼5400 m a.s.l. (Appendix C, Figure C1), and this corresponds to a temperature limitation on plant stomatal conductance (Eq 4.6) at these cold, upper elevations. In fact, No-Glacier model test shows that without the temperature increase, upslope migration of vegetation would only generate a 7% increase in ET and 4% reduction in stream discharge, compared to the 22% decrease in stream discharge seen for the case of upslope vegetation migration plus temperature increase. This findings demonstrates the interacting effect of climate and vegetation on hydrology and underscores the importance of considering both simultaneously. Our results also agree with a couple of modeling studies in temperate and boreal mountain watersheds in North America, which indicated that ET

and stream discharge would be relatively insensitive to upslope migration of vegetation without an increase in temperature at higher elevations (Goulden & Bales, 2014; Rasouli et al., 2019). Our work demonstrates that temperature limitations seen in higher latitude climates can also be relevant at high elevations in the tropics.

4.5.2 Changes in Evapotranspiration

Evaluating the changes in ET enables us to understand the different stream discharge responses among the scenarios. Our model simulations indicate that with just the removal of glacier melt and 4.5 °C warming, total ET increases by 25%, despite less water inputs to the watershed. After the upslope shift of all plant types and with tussock encroachment, total ET further increases to 43% and 46% more than the Base case. The 25% increase in total ET from the Base case to NoGlacier+ΔT scenario is due to the 4.5 °C increase in temperature, while the >40% increase in ET for the two vegetation migration scenarios reflects the effect of both warming and vegetation expansion, as described above.

Total ET in the model comprises three components: soil evaporation, canopy evaporation, and canopy transpiration. The response of total ET to changes in temperature and vegetation distribution and composition can be understood by examining the changes to each of the different components, because these show different responses among the scenarios.

The 25% increase in total ET in the NoGlacier+ΔT scenario occurs primarily due to increase in canopy transpiration (84%) and soil evaporation (21%) compared to the Base case (Figure ET-Components a). Canopy evaporation remains essentially unchanged in the NoGlacier+ΔT scenario compared to the Base case, which is due to lower sensitivity of canopy evaporation to temperature (Eq. 4.2) relative to canopy transpiration (Eq 4.4) and soil evaporation (Eq 4.1). The strong temperature dependence of canopy transpiration, which comprised the largest part of the ET change, is due to the quadratic reliance of canopy resistance on temperature (Eq. 4.9). It was less expected that soil evaporation showed more sensitivity to temperature than canopy evaporation in the NoGlacier+ΔT scenario. This was likely because soil evaporation dominates in the upper watershed above the vegetation line, where the colder temperatures more

significantly reduce potential evaporation due to nonlinear relationships in the Penman-Monteith equation.

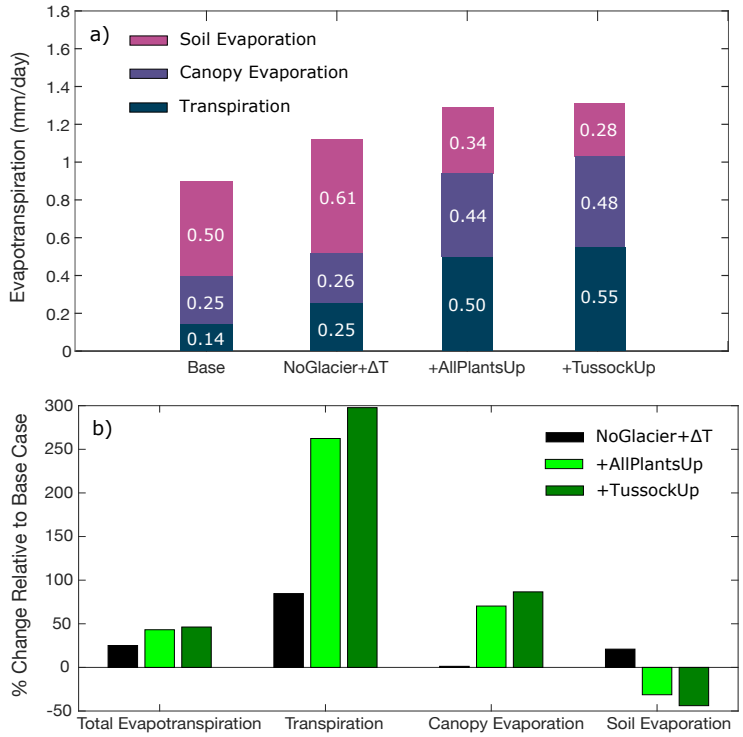

Figure 4.8: (a) Bar plots of proportional contribution of different components of total ET including canopy transpiration, canopy evaporation, and soil evaporation for Base, NoGlacier+ΔT, +AllPlantsUp, and +TussockUp scenarios and (b) percent changes of total evapotranspiration, canopy transpiration, canopy evaporation, and soil evaporation relative to for NoGlacier+ΔT, +AllPlantsUp, and +TussockUp scenarios.

Comparison of ET for the two upslope vegetation migration scenarios versus ET for the NoGlacier+ΔT scenario can demonstrate the effect of the 75% expansion in vegetation cover (from 41% to 72% of the total watershed, considering the area below the vegetation line). The +AllPlantsUp scenario yielded a 14% increase in total evapotranspiration compared to the NoGlacier+ΔT scenario, indicating that the ET change is considerably lower than proportional to the vegetation cover change. This can be explained by examining changes in the three components of ET. For +AllPlantsUp, canopy transpiration and canopy evaporation increase respectively by 96% and 68%

relative to NoGlacier+ΔT, which is much more commensurate with the 75% expansion in vegetation coverage. (Note that the somewhat higher canopy transpiration – 96% increases versus 75% expansion – results from the expansion of deeper rooted plants even without full tussock encroachment, while the somewhat lower canopy evaporation – 68% versus 75% – results from the lower water availability at higher elevations to where the vegetation is expanding.) However, the relative change in total ET with +AllPlantsUp (14%) is so much lower than the 75% vegetation expansion, because soil evaporation decreases notably from the NoGlacier+ΔT scenario. With the increase in vegetation cover as plants migrate upslope, the bare ground area decreases, leading to a 43% lower soil evaporation in the +AllPlantsUp scenario, compared to NoGlacier+ΔT scenario (Figure 4.8a and b).

This counteracting effect of decreased soil evaporation and increased canopy transpiration and evaporation can also be seen when comparing the scenario with tussock encroachment with the scenario of all plant types shifting upslope. Because of its deeper roots and other physiological differences (Table 4.2), when tussock grass encroaches into the areas with Upper Páramo plant forms, there is notably greater canopy transpiration and canopy evaporation compared to +AllPlantsUp (increases of 10% and 9%, respectively). However, higher ground surface coverage of tussock grass compared to other plants found in the watershed results in greater shading and a sizable reduction in soil evaporation of 18% compared to the +AllPlantsUp scenario (SHDFAC in Table 4.2). As a result, despite the greater canopy ET components, +TussockUp has only a very small 3% higher total ET than +AllPlantsUp.

Studies in arid to semi-arid parts of the southwest US (Schlesinger et al., 1990) have also noted a decrease in soil evaporation with the increased shading under expanded vegetation cover. In fact, in the cases of woody plant encroachment into grasslands, the deeper-rooted woody plants also have greater leaf areas compared with grasses, and the shading-induced reduction in soil evaporation has been found to lessen the hydrological response to woody encroachment (Huxman et al., 2005).

Overall, despite the counteracting effects among ET components, our simulations show that as long as temperature is sufficiently warm at Gavilan Machay, total ET and stream discharge can nonetheless be appreciably influenced by the upslope migration of vegetation, although the additional impact by tussock grass encroachment is very

small. The simulated increases in canopy transpiration plus evaporation with upslope shift of all plant types is responsible for a 16% decrease in stream discharge relative to the NoGlacier+ΔT scenario (Figure 4.7), and this slightly increases to 20% for the case of tussock grass encroachment.

It is important to note that our interpretations are highly dependent on whether individual ET components are correctly simulated in the model. ET model results can be affected by uncertainties in the climate inputs used for their calculations (including temperature, solar radiation, precipitation, wind, and relative humidity), as well as uncertainties in the ET parameterization equations summarized in Section 4.4.1. Climate forcings are highly variable along steep altitudinal gradients such as in Gavilan Machay. The precipitation and temperature lapse rates for the watershed were estimated using the limited available data at this remote site (see Saberi et al. (2019) for details), which may not fully capture the spatial variability of meteorological conditions in the watershed. Additionally, solar radiation and wind data were obtained from the Global Land Data Assimilation Systems (GLDAS) (Rodell et al., 2004) and assumed to be constant over the space. In terms of ET parameterizations, previous studies show considerable ranges in ET partitioning results among different models, which indicate that model parameterization can be a major source of uncertainty (Kumar et al., 2018).

Although field validation of our modeled ET components was not possible at our remote field site, our simulated ET partitioning does fall within observed ranges of T/ET in related settings. Our model simulations indicate that soil evaporation is the major component of total watershed ET in the Base and NoGlacier+ΔT scenarios, comprising $\sim$55% of total ET, and this number decreases to 26-20% after plants migrate upslope (Figure 4.8a). Within the vegetated part of the watershed, the ratio of transpiration to evapotranspiration (T/ET) increases from 36% in the Base case to 52-54% in all three scenarios with increased temperature (NoGlacier+ΔT, +AllPlantsUp, +TussockUp), making transpiration the major contributor to total evapotranspiration with the warmer temperatures. Schlesinger and Jasechko (2013) showed based on 84 study sites across the globe that the ratio of T/ET depends on precipitation, temperature, and biome, with values varying from 36% in deserts to 84% in tropical rainforests, covering the range of 36%-54% simulated at Gavilan Machay. Individual ET components have not previously been measured in páramo settings, but ET partitioning has been

measured in a warm, tropical montane grassland in Hawaii by Hsieh et al. (1998). They found that the T/ET ratio along an arid to humid transect ranging from 185 m a.s.l. (average 180 mm/yr precipitation and 23 °C) to 1200 m a.s.l. (average 2500 mm/yr precipitation and 17 °C) varied from 32% to 72%. These results of increasing T/ET with greater precipitation at higher elevation suggests that there is a plant water limitation at lower elevations. In contrast to the Hawaii site, Gavilan Machay is overall much cooler (watershed average of 6.8 °C in the Base case and 11.3 °C in the scenarios with warming), and as discussed earlier, transpiration here exhibits a temperature limitation under the Base case scenario. However, simulations at Gavilan Machay show a similar notable increase in T/ET (36% to ∼54%) as in the Hawaii observations (32% to 72%) when the limiting condition becomes relaxed (warming and greater precipitation). These comparisons with observed ET partitioning provide some confidence that our simulated ET components at Gavilan Machay correspond to physically reasonable values and trends. However, our study underscores the importance of understanding and parameterizing ET partitioning for predicting impacts of temperature and vegetation change on discharge.

4.6 Conclusions

There is a critical knowledge gap about how climate-driven glacier retreat together with upslope vegetation migration will impact stream discharge in rapidly warming tropical mountainous watersheds, and this has crucial implications for local communities who rely on these watersheds for their water resources. In this study we estimated changes in vegetation cover due to warming and implemented this with a fully distributed and integrated watershed model, BioRT-Flux-PIHM, in order to evaluate the ecohydrologic response of an Ecuadorian tropical glacierized mountainous watershed to glacier and vegetation cover change under warming temperatures.

Combined removal of glacier melt, upslope migration of vegetation, and a 4.5 °C increase in temperature results in a substantial reduction in simulated stream discharge by 74% from current conditions, mainly due to an increase in evapotranspiration. Further, under this scenario, the model shows that near no-flow conditions can occur in the stream during drought times, which has dire consequences for local communities living

nearby the mountain. Underscoring the importance of evaluating interactions among climate and vegetation, our model tests showed that upslope vegetation shift only has a notable impact on stream discharge when there are sufficiently warmer conditions, because otherwise cool temperatures limit transpiration at high elevations. Model simulations also show that potential encroachment of deeper-rooted tussock grass into the other upward migrating plant types could slightly exacerbate the situation, causing an additional 4% decrease in stream discharge. The response of stream discharge to changes in plant cover and composition is particularly sensitive to ET partitioning. Model simulations indicate that as plants migrate upslope and cover the bare ground, canopy evaporation plus transpiration increases; however, soil evaporation reduces due to shading effects, which somewhat mitigates the impact of vegetation expansion on water fluxes. Despite this counteracting effect, upslope migration of vegetation and tussock encroachment respectively lead to 16% and 20% lower stream discharge compared to the case where only glacier retreat under warming conditions are considered.

It is important to note that our results and estimates strongly depend on ET simulations, which are highly sensitive to climate inputs and vegetation parameterizations. A more robust and accurate estimate of ET and its components require high resolution measurements of meteorological forcings across space and time, particularly in a watershed with a steep topographic gradient such as Gavilan Machay. Another factor controlling ET estimations is the vegetation parameterization in the model. Even though we established new PFTs for different páramo classes across the watershed, it is likely that the parameter values and/or parameterization structures do not fully capture the unique characteristics of páramo species. Our work calls for further investigation on ET estimates in páramo environments, which include unique plant forms that may have different physiological characteristics than many other plant types globally, as well as highly variable meteorological conditions over steep topographic gradients.

Chapter 5

Conclusions and Future Research Directions

Due to difficult access and data sparsity in tropical glacierized watersheds, there is a critical knowledge gap about their hydrological and hydrochemical response to rapid glacier retreat and upslope migration of vegetation under climate change. This research addressed these challenges using a recently developed integrated watershed model with reactive transport, BioRT-Flux-PIHM, which represents interactions among surface energy fluxes, surface and subsurface hydrology, solute movement, and geochemical reactions (Qu & Duffy, 2007; Bao et al., 2017; Shi et al., 2013; Zhi et al., 2020). Implementation of BioRT-Flux-PIHM enabled us to extend available observations in order to evaluate the hydrological and hydrochemical response of a tropical glacierized mountainous watershed in the Ecuadorian Andes to combined climate and vegetation changes. Calibrated to hydrochemical and discharge measurements from a sub-humid watershed on Volcán Chimborazo, the model provides one of the first results for the following: estimate of glacier melt contributions to stream discharge via groundwater pathways, examination of ecohydrolgical impacts of vegetation shift in a tropical glacierized watershed, and continuous solute concentration-stream discharge (C-Q) relationships in a tropical glacierized watershed.

We found through simulations that at our sub-humid study watershed, Gavilan Machay, glacier melt contributes an annual average of ∼50% of discharge. Most melt

contributions to discharge occurred through surface runoff in the model, but some meltwater recharged to groundwater, helping to support a relatively steady groundwater discharge to the stream that is about 37% greater with glacier melt than without glacier melt.

Upslope migration of vegetation under warmer temperatures can further exacerbate decreases in stream discharge after glaciers retreat. Our model simulations indicate that upslope migration of all vegetation types, along with 4.5 °C increase in temperature, leads to 43% higher evapotranspiration (ET) and 74% lower stream discharge compared to current conditions. Upslope migration of vegetation with tussock grass encroachment only further increases ET by 3% and reduces streamflow by another 4% relative to the scenario with all plant types shifting upslope, indicating that changing plant type distributions in páramo settings may not be as hydrologically impactful as observed in temperate grasslands experiencing woody plant encroachment. Demonstrating the need to consider the interacting effects of vegetation and climate change, model simulations indicate the reduction in streamflow under vegetation expansion is dependent on sufficiently warmer temperatures, because otherwise there is a temperature limitation on plant transpiration at high elevations. Additionally, changes in stream discharge caused by upslope migration of vegetation and tussock encroachment is highly sensitive to ET partitioning. Model simulations show that as plants migrate upslope, canopy evapotranspiration increases; however, the vegetation cover at the same time reduces soil evaporation, and this counteracting effect mitigates the impact of vegetation expansion on water resources.

Further, our results when considering reactive transport indicate that the stream outlet concentration (C) and discharge (Q) pattern in the Gavilan Machay watershed comprises a mostly chemostatic graph (concentration stays mostly stable with changing discharge), imposed by melt-driven dilution events. The chemostatic background was attributed to the large contribution of groundwater to streamflow (78%), which collects solutes as it moves through weatherable volcanic soils and fractured volcanic bedrock and is high in part because of the notable fraction (37%) consisting of infiltrated ice-melt. During ice-melt events, the high contribution of low-concentration surface runoff, especially during melt events coinciding with large precipitation peaks, was the main driver of dilution events at the watershed outlet.

Our results suggest that attenuating ice-melt inputs will decrease groundwater storage and stream discharge, and thus lower weathering and solute export rates. While these changes may allow for a more chemostatic behavior with higher concentrations of solutes such as Na^{+}, Mg^{2+}, and Ca^{2+}, the overall decrease in solute export (by 23% in the model scenario without ice-melt and 44% after plants migrate upslope) will limit the delivery of solutes to downstream areas in the Amazon Basin, which could have crucial implications for downstream ecological productivity, considering the role of these solutes as plants macro- and micronutrients.

Future Research Directions

To further understand the impact of climate change and upslope migration of vegetation on Volcán Chimborazo's water availability and solute export rate, there are several areas where additional research is needed. So far, our tests have covered only one simulation year due to the lack of available in-situ climate observations. This greatly limits our ability to assess hydrological and hydrochemical processes under conditions outside of the drier- and warmer-than-usual year captured in our simulations, and it prevents any evaluation of interannual variability. Simulations over a longer historical time period can be possible through meteorological reconstructions that build off different regional meteorological stations and coarse-scale global remote sensing products.

Another important need is to incorporate General Circulation Model (GCM) climate projection scenarios to extend beyond the simple no-glacier step warming tests that we explored thus far. Not only would GCM inputs make it possible to consider changes in other climate variables, such as precipitation and humidity, but we would also be able to generate transient hydrological and hydrochemical predictions with the model as glaciers retreat. With full meteorological inputs, transient glacier conditions can be simulated with the new Glacier-Flux-PIHM model, which was recently developed with collaborators (L. Li and Y. Shi, Penn State) to simulate glacier melt using an energy balance approach.

To enhance our understanding on the rate at which vegetation shifts upslope at Volcán Chimborazo, there is a need for a more comprehensive analysis of historical satellite imagery in order to delineate the historical vegetation changes. For example, comparing more recent high resolution imagery (e.g., using a drone) with a historical

Landsat image from 1980 would further serve to test and constrain our current estimate of vegetation response to climate change, which is based on a 1978 land-cover map developed through surveys by the Ecuadorian government. This will enable us to fully understand the response of vegetation to changes in climate, which will lead into more accurate predictions of the response of vegetation in Gavilan Machay watershed to climate change in the future.

Gaps also remain in our understanding about the subsurface hydrogeology, which we know from outcrops to include both heterogeneous moraine sediments and fractured volcanic bedrock, but until now we have only indirectly inferred their bulk properties from tracer data. Incorporating geophysical methods such as Ground Penetrating Radar (GPR) would allow us to potentially constrain water table depths or other subsurface characteristics to help us more accurately simulate groundwater flow.

Further, extending the study to cover other tropical glacierized watersheds in the Andes can allow us to assess whether findings at Gavilan Machay apply more generally. It can also enable us to upscale results to determine regional hydrochemical impacts of changing glacierized Andean watersheds - which we hypothesize serve as hotspot sources of solutes and nutrients - on the Amazon basin ecosystem.

Lastly, considering the urgent implications that changing glacierized watersheds have on water resources, our nascent interactions with local Indigenous communities around Chimborazo could be further developed, with guidance from our Ecuadorian university collaborators. Good communication with local agrarian communities can ensure that our findings are useful for water resource planning for irrigation. Further, a strong collaboration can improve our models by adding important knowledge about environmental conditions (including land-use changes), which we struggle to observe at these remote locations.

References

Amundson, R., Heimsath, A., Owen, J., Yoo, K., & Dietrich, W. E. (2015). Hillslope soils and vegetation. *Geomorphology*, *234*, 122–132.

Andermann, C., Longuevergne, L., Bonnet, S., Crave, A., Davy, P., & Gloaguen, R. (2012). Impact of transient groundwater storage on the discharge of Himalayan rivers. *Nature Geoscience*, *5*(2), 127–132.

Anderson, S. P. (2005). Glaciers show direct linkage between erosion rate and chemical weathering fluxes. *Geomorphology*, *67*(1-2), 147–157.

Anderson, S. P., Drever, J. I., & Humphrey, N. F. (1997). Chemical weathering in glacial environments. *Geology*, *25*(5), 399–402.

Andrews, E. D. (1981a). Measurement and computation of bed-material discharge in a shallow sand-bed stream, Muddy Creek, Wyoming. *Water Resources Research*, *17*(1), 131–141.

Andrews, E. D. (1981b). Measurement and computation of bed-material discharge in a shallow sand-bed stream, Muddy Creek, Wyoming. *Water Resources Research*, *17*(1), 131–141.

Bales, R. C., Molotch, N. P., Painter, T. H., Dettinger, M. D., Rice, R., & Dozier, J. (2006). Mountain hydrology of the western united states. *Water Resources Research*, *42*(8).

Bao, C., Li, L., Shi, Y., & Duffy, C. (2017). Understanding watershed hydrogeochemistry: 1. development of rt-flux-pihm. *Water Resources Research*, *53*(3), 2328–2345.

Baraer, M., Mark, B. G., McKenzie, J. M., Condom, T., Bury, J., Huh, K.-I., Portocarrero, C., Gómez, J., & Rathay, S. (2012). Glacier recession and water resources in Peru's Cordillera Blanca. *Journal of Glaciology*, *58*(207), 134–150.

Baraer, M., McKenzie, J., Mark, B. G., Gordon, R., Bury, J., Condom, T., Gomez, J., Knox, S., & Fortner, S. K. (2015). Contribution of groundwater to the outflow from ungauged glacierized catchments: a multi-site study in the tropical Cordillera Blanca, Peru. *Hydrological Processes*, *29*(11), 2561–2581.

Baraer, M., McKenzie, J. M., Mark, B. G., Bury, J., & Knox, S. (2009). Characterizing contributions of glacier melt and groundwater during the dry season in a poorly gauged catchment of the Cordillera Blanca (Peru). *Advances in Geosciences*, *22*, 41–49.

Barba, D., Robin, C., Samaniego, P., & Eissen, J.-P. (2008). Holocene recurrent explosive activity at chimborazo volcano (ecuador). *Journal of Volcanology and Geothermal Research*, *176*(1), 27–35.

Barba, D., Samaniego, P., Eissen, J.-p., Robin, C., Fornari, M., Cotten, J., & Beate, B. (2005). Geology and structure of the late Pleistocene to Holocene Chimborazo stratovolcano (Ecuador). *6th International Symposium on Andean Geodynamics (ISAG 2005, Barcelona)*, (January), 90–93.

Barnett, T. P., Adam, J. C., & Lettenmaier, D. P. (2005). Potential impacts of a warming climate on water availability in snow-dominated regions. *Nature*, *438*(7066), 303–309.

Barnhart, T. B., Molotch, N. P., Livneh, B., Harpold, A. A., Knowles, J. F., & Schneider, D. (2016). Snowmelt rate dictates streamflow. *Geophysical Research Letters*, *43*(15), 8006–8016.

Baronas, J. J., Torres, M. A., Clark, K. E., & West, A. J. (2017). Mixing as a driver of temporal variations in river hydrochemistry: 2. major and trace element concentration dynamics in the andes-amazon transition. *Water Resources Research*, *53*(4), 3120–3145.

Bartoli, F., Poulenard, A., & Schouller, B. (2007). Influence of allophane and organic matter contents on surface properties of andosols. *European journal of soil science*, *58*(2), 450–464.

Beltrán, K., Salgado, S., Cuesta, F., León-Yánez, S., Romoleroux, K., Ortiz, E., Cárdenas, A., & Velástegui, A. (2009). Distribución espacial, sistemas ecológicos y caracterización florística de los páramos en el ecuador. *EcoCiencia, Proyecto Páramo Andino y Herbario QCA. Quito*, (pp. 14–150).

Benettin, P., Bailey, S. W., Campbell, J. L., Green, M. B., Rinaldo, A., Likens, G. E., McGuire, K. J., & Botter, G. (2015). Linking water age and solute dynamics in streamflow at the h ubbard b rook e xperimental f orest, nh, usa. *Water Resources Research*, *51*(11), 9256–9272.

Beniston, M. (2003). Climatic change in mountain regions: a review of possible impacts. *Climate variability and change in high elevation regions: Past, present & future*, (pp. 5–31).

Benz, U. C., Hofmann, P., Willhauck, G., Lingenfelder, I., & Heynen, M. (2004). Multi-resolution, object-oriented fuzzy analysis of remote sensing data for gis-ready information. *ISPRS Journal of photogrammetry and remote sensing*, *58*(3-4), 239–258.

Bhatt, G., Kumar, M., & Duffy, C. J. (2014). A tightly coupled GIS and distributed hydrologic modeling framework. *Environmental Modelling & Software*, *62*, 70–84.

Bluth, G. J., & Kump, L. R. (1994). Lithologic and climatologic controls of river chemistry. *Geochimica et Cosmochimica Acta*, *58*(10), 2341–2359.

Bouchez, J., Moquet, J.-S., Espinoza, J. C., Martinez, J.-M., Guyot, J.-L., Lagane, C., Filizola, N., Noriega, L., Hidalgo Sanchez, L., & Pombosa, R. (2017). River mixing in the amazon as a driver of concentration-discharge relationships. *Water Resources Research*, *53*(11), 8660–8685.

Bradley, R. S. (2006). CLIMATE CHANGE: Threats to Water Supplies in the Tropical Andes. *Science*, *312*(5781), 1755–1756.

Bradley, R. S., Vuille, M., Hardy, D., & Thompson, L. G. (2003). Low latitude ice cores record Pacific sea surface temperatures. *Geophysical Research Letters*, *30*(4), 2–5.

Brantley, S. L., Eissenstat, D. M., Marshall, J. A., Godsey, S. E., Balogh-Brunstad, Z., Karwan, D. L., Papuga, S. A., Roering, J., Dawson, T. E., Evaristo, J., et al. (2017). Reviews and syntheses: on the roles trees play in building and plumbing the critical zone. *Biogeosciences (Online)*, *14*(22).

Brantley, S. L., Kubicki, J. D., & White, A. F. (2008). Kinetics of water-rock interaction.

Brantley, S. L., Lebedeva, M., & Hausrath, E. M. (2012). A geobiological view of weathering and erosion. *Fundamentals of geobiology*, (pp. 205–227).

Braun, L. N., Weber, M., & Schulz, M. (2000). Consequences of climate change for runoff from Alpine regions. *Annals of Glaciology*, *31*(1), 19–25.

Breshears, D. D., Huxman, T. E., Adams, H. D., Zou, C. B., & Davison, J. E. (2008). Vegetation synchronously leans upslope as climate warms. *Proceedings of the National Academy of Sciences*, *105*(33), 11591–11592.

Brown, G. H. (2002). Glacier meltwater hydrochemistry. *Applied Geochemistry*, *17*(7), 855–883.

Burnett, C., & Blaschke, T. (2003). A multi-scale segmentation/object relationship modelling methodology for landscape analysis. *Ecological modelling*, *168*(3), 233–249.

Bury, J., Mark, B. G., Carey, M., Young, K. R., McKenzie, J. M., Baraer, M., French, A., & Polk, M. H. (2013). New Geographies of Water and Climate Change in Peru: Coupled Natural and Social Transformations in the Santa River Watershed. *Annals of the Association of American Geographers*, *103*(2), 363–374.

Bury, J. T., Mark, B. G., McKenzie, J. M., French, A., Baraer, M., Huh, K. I., Zapata Luyo, M. A., & Gómez López, R. J. (2011). Glacier recession and human vulnerability in the Yanamarey watershed of the Cordillera Blanca, Peru. *Climatic Change*, *105*(1-2), 179–206.

Buytaert, W., & Beven, K. (2011). Models as multiple working hypotheses: hydrological simulation of tropical alpine wetlands. *Hydrological Processes*, *25*(11), 1784–1799.

Buytaert, W., Célleri, R., De Bièvre, B., Cisneros, F., Wyseure, G., Deckers, J., & Hofstede, R. (2006). Human impact on the hydrology of the Andean páramos. *Earth-Science Reviews*, *79*(1-2), 53–72.

Buytaert, W., Vuille, M., Dewulf, A., Urrutia, R., Karmalkar, A., & Célleri, R. (2010). Uncertainties in climate change projections and regional downscaling in the tropical andes: implications for water resources management. *Hydrology and Earth System Sciences*, *14*(7), 1247–1258.

Caceres, B., Francou, B., Favier, V., Bontron, G., Tachker, P., Bucher, R., Taupin, J.-D., Vuille, M., Maisincho, L., & Delachaux, F. (2006). Glacier 15, Antisana, Ecuador: its glaciology and relations to water resources.

Calmels, D., Galy, A., Hovius, N., Bickle, M., West, A. J., Chen, M.-C., & Chapman, H. (2011). Contribution of deep groundwater to the weathering budget in a rapidly eroding mountain belt, taiwan. *Earth and Planetary Science Letters*, *303*(1-2), 48–58.

Carey, M., Molden, O. C., Rasmussen, M. B., Jackson, M., Nolin, A. W., & Mark, B. G. (2017). Impacts of Glacier Recession and Declining Meltwater on Mountain Societies. *Annals of the American Association of Geographers*, *107*(2), 350–359.

Cauvy-Fraunié, S., Condom, T., Rabatel, A., Villacis, M., Jacobsen, D., & Dangles, O. (2013). Technical Note: Glacial influence in tropical mountain hydrosystems evidenced by the diurnal cycle in water levels. *Hydrology and Earth System Sciences*, *17*(12), 4803–4816.

Célleri, R., & Feyen, J. (2009). The hydrology of tropical andean ecosystems: importance, knowledge status, and perspectives. *Mountain Research and Development*, *29*(4), 350–355.

Chen, I.-C., Hill, J. K., Ohlemüller, R., Roy, D. B., & Thomas, C. D. (2011). Rapid range shifts of species associated with high levels of climate warming. *Science*, *333*(6045), 1024–1026.

Chen, I.-C., Shiu, H.-J., Benedick, S., Holloway, J. D., Chey, V. K., Barlow, H. S., Hill, J. K., & Thomas, C. D. (2009). Elevation increases in moth assemblages over 42 years on a tropical mountain. *Proceedings of the National Academy of Sciences*, *106*(5), 1479–1483.

Chen, J., Knight, R., & Zebker, H. A. (2017). The Temporal and Spatial Variability of the Confined Aquifer Head and Storage Properties in the San Luis Valley, Colorado Inferred From Multiple InSAR Missions. *Water Resources Research*, *53*(11), 9708–9720.

Christophersen, N., Neal, C., Hooper, R. P., Vogt, R. D., & Andersen, S. (1990). Modelling streamwater chemistry as a mixture of soilwater end-members: a step towards second-generation acidification models. *Journal of Hydrology*, *116*(1-4), 307–320.

Clapperton, C. M. (1990). Glacial and volcanic geomorphology of the Chimborazo-Carihuairazo Massif, Ecuadorian Andes. *Transactions of the Royal Society of Edinburgh: Earth Sciences*, *81*(02), 91–116.

Clow, D., & Mast, M. A. (2010). Mechanisms for chemostatic behavior in catchments: implications for co2 consumption by mineral weathering. *Chemical Geology*, *269*(1-2), 40–51.

Clow, D., Schrott, L., Webb, R., Campbell, D., Torizzo, A., & Dornblaser, M. (2003). Ground Water Occurrence and Contributions to Streamflow in an Alpine Catchment, Colorado Front Range. *Ground Water*, *41*(7), 937–950.

Collins, D. N. (1979). Hydrochemistry of meltwaters draining from an alpine glacier. *Arctic and Alpine Research*, *11*(3), 307–324.

Collins, D. N. (1983). Solute yield from a glacierized high mountain basin.

Collins, D. N. (1999). Solute flux in meltwaters draining from a glacierized basin in the karakoram mountains. *Hydrological processes*, *13*(18), 3001–3015.

Colwell, R. K., Brehm, G., Cardelús, C. L., Gilman, A. C., & Longino, J. T. (2008). Global warming, elevational range shifts, and lowland biotic attirition in the wet tropics. *Science*, *322*(October), 258–261.

Crossman, J., Bradley, C., Boomer, I., & Milner, A. M. (2011). Water Flow Dynamics of Groundwater-Fed Streams and Their Ecological Significance in a Glacierized Catchment. *Arctic, Antarctic, and Alpine Research*, *43*(3), 364–379.

Cuatrecasas, J. (1968). Páramo vegetation and its life forms. In *Colloquium Geographicum*, vol. 9.

Darrouzet-Nardi, A., D'Antonio, C. M., & Dawson, T. E. (2006). Depth of water acquisition by invading shrubs and resident herbs in a sierra nevada meadow. *Plant and Soil*, *285*(1), 31–43.

Dessert, C., Dupre, B., Gaillardet, J., Godderis, Y., Francois, L., & Shott, J. (2005). Basalt weathering laws and the impact of basalt weathering on the global carbon cycle. *GeCAS*, *69*(10), A687.

Dingman, S. L. (2015). *Physical hydrology*. Waveland press.

Drever, J. I. (1994). The effect of land plants on weathering rates of silicate minerals. *Geochimica et Cosmochimica Acta*, *58*(10), 2325–2332.

Duffy, C., Shi, Y., Davis, K., Slingerland, R., Li, L., Sullivan, P. L., Goddéris, Y., & Brantley, S. L. (2014). Designing a Suite of Models to Explore Critical Zone Function. *Procedia Earth and Planetary Science*, *10*, 7–15.

Dunne, T., Mertes, L. A., Meade, R. H., Richey, J. E., & Forsberg, B. R. (1998). Exchanges of sediment between the flood plain and channel of the amazon river in brazil. *Geological Society of America Bulletin*, *110*(4), 450–467.

Ek, M. B., Mitchell, K. E., Lin, Y., Rogers, E., Grunmann, P., Koren, V., Gayno, G., & Tarpley, J. D. (2003). Implementation of Noah land surface model advances in the National Centers for Environmental Prediction operational mesoscale Eta model. *Journal of Geophysical Research: Atmospheres*, *108*(D22).

Engel, M., Penna, D., Bertoldi, G., Dell'Agnese, A., Soulsby, C., & Comiti, F. (2016). Identifying run-off contributions during melt-induced run-off events in a glacierized alpine catchment. *Hydrological Processes*, *30*(3), 343–364.

Engel, M., Penna, D., Bertoldi, G., Vignoli, G., Tirler, W., & Comiti, F. (2019). Controls on spatial and temporal variability of streamflow and hydrochemistry in a glacierized catchment.

Escher-Vetter, H., Reinwarth, O., & Rentsch, H. (1994). Two decades of runoff measurements (1974 to 1993) at the pegelstation Vernagtbach/Oetztal alps. *Zeitschrift für Gletscherkunde und Glazialgeologie*, *30*(August 1992), 99–107.

Fadrique, B., Báez, S., Duque, Á., Malizia, A., Blundo, C., Carilla, J., Osinaga-Acosta, O., Malizia, L., Silman, M., Farfán-Ríos, W., et al. (2018). Widespread but heterogeneous responses of andean forests to climate change. *Nature*, *564*(7735), 207–212.

Farr, T. G., Rosen, P. A., Caro, E., Crippen, R., Duren, R., Hensley, S., Kobrick, M., Paller, M., Rodriguez, E., & Roth, L. (2007). The shuttle radar topography mission. *Reviews of Geophysics*, *45*(2).

Farvolden, R. (1963). Geologic controls on ground-water storage and base flow. *Journal of hydrology*, *1*(3), 219–249.

Favier, V. (2004). Glaciers of the outer and inner tropics: A different behaviour but a common response to climatic forcing. *Geophysical Research Letters*, *31*(16), L16403.

Favier, V., Coudrain, A., Cadier, E., Francou, B., Ayabaca, E., Maisincho, L., Praderio, E., Villacis, M., & Wagnon, P. (2008). Evidence of groundwater flow on Antizana ice-covered volcano, Ecuador / Mise en évidence d'écoulements souterrains sur le volcan englacé Antizana, Equateur. *Hydrological Sciences Journal*, *53*(1), 278–291.

Feeley, K. J., & Silman, M. R. (2010). Land-use and climate change effects on population size and extinction risk of andean plants. *Global change biology*, *16*(12), 3215–3222.

Feeley, K. J., Silman, M. R., Bush, M. B., Farfan, W., Cabrera, K. G., Malhi, Y., Meir, P., Revilla, N. S., Quisiyupanqui, M. N. R., & Saatchi, S. (2011). Upslope migration of Andean trees. *Journal of Biogeography*, *38*(4), 783–791.

Fernández, A., & Mark, B. G. (2016). Modeling modern glacier response to climate changes along the Andes Cordillera: A multiscale review. *Journal of Advances in Modeling Earth Systems*, *8*(1), 467–495.

Finke, P., Vanwalleghem, T., Opolot, E., Poesen, J., & Deckers, J. (2013). Estimating the effect of tree uprooting on variation of soil horizon depth by confronting pedogenetic simulations to measurements in a belgian loess area. *Journal of Geophysical Research: Earth Surface*, *118*(4), 2124–2139.

Fortner, S. K., Mark, B. G., McKenzie, J. M., Bury, J., Trierweiler, A., Baraer, M., Burns, P. J., & Munk, L. (2011). Elevated stream trace and minor element concentrations in the foreland of receding tropical glaciers. *Applied Geochemistry*, *26*(11), 1792–1801.

Fountain, A. G., & Tangborn, W. V. (1985). The Effect of Glaciers on Streamflow Variations. *Water Resources Research*, *21*(4), 579–586.

Francou, B. (2003). Tropical climate change recorded by a glacier in the central Andes during the last decades of the twentieth century: Chacaltaya, Bolivia, 16S. *Journal of Geophysical Research*, *108*(D5), 4154.

Francou, B. (2004). New evidence for an ENSO impact on low-latitude glaciers: Antizana 15, Andes of Ecuador. *Journal of Geophysical Research*, *109*(D18), D18106.

Gabbi, J., Carenzo, M., Pellicciotti, F., Bauder, A., & Funk, M. (2014). A comparison of empirical and physically based glacier surface melt models for long-term simulations of glacier response. *Journal of Glaciology*, *60*(224), 1140–1154.

Gibss, R. (1967). The geochemistry of the amazon river system: Part 1. *The factors that control the salinity and the composition and concentration of the suspended solids. Geological Society of American Bulletin*, *78*, 1203–1232.

Ginot, P., Schwikowski, M., Schotterer, U., Stichler, W., Gäggeler, H. W., Francou, B., Gallaire, R., & Pouyaud, B. (2002). Potential for climate variability reconstruction from andean glaciochemical records. *Annals of Glaciology*, *35*, 443–450.

Gislason, S. R., Arnorsson, S., & Armannsson, H. (1996). Chemical weathering of basalt in southwest iceland; effects of runoff, age of rocks and vegetative/glacial cover. *American Journal of Science*, *296*(8), 837–907.

Godsey, S. E., Kirchner, J. W., & Clow, D. W. (2009). Concentration–discharge relationships reflect chemostatic characteristics of us catchments. *Hydrological Processes: An International Journal*, *23*(13), 1844–1864.

Gordon, R. P., Lautz, L. K., McKenzie, J. M., Mark, B. G., Chavez, D., & Baraer, M. (2015). Sources and pathways of stream generation in tropical proglacial valleys of the Cordillera Blanca, Peru. *Journal of Hydrology*, *522*, 628–644.

Goulden, M. L., & Bales, R. C. (2014). Mountain runoff vulnerability to increased evapotranspiration with vegetation expansion. *Proceedings of the National Academy of Sciences*, *111*(39), 14071–14075.

Harden, D. R. (2004). *California geology*. Prentice Hall.

Harpold, A. A., & Brooks, P. D. (2018). Humidity determines snowpack ablation under a warming climate. *Proceedings of the National Academy of Sciences*, *115*(6), 1215–1220.

Harrington, J. S., Mozil, A., Hayashi, M., & Bentley, L. R. (2018). Groundwater flow and storage processes in an inactive rock glacier. *Hydrological Processes*, *32*(20), 3070–3088.

Hartmann, J., Jansen, N., Dürr, H. H., Kempe, S., & Köhler, P. (2009). Global co2-consumption by chemical weathering: What is the contribution of highly active weathering regions? *Global and Planetary Change*, *69*(4), 185–194.

Hasenmueller, E. A., Jin, L., Stinchcomb, G. E., Lin, H., Brantley, S. L., & Kaye, J. P. (2015). Topographic controls on the depth distribution of soil co2 in a small temperate watershed. *Applied Geochemistry*, *63*, 58–69.

Hay, G. J., & Castilla, G. (2008). Geographic object-based image analysis (geobia): A new name for a new discipline. In *Object-based image analysis*, (pp. 75–89). Springer.

He, Z., Vorogushyn, S., Unger-Shayesteh, K., Gafurov, A., Kalashnikova, O., Omorova, E., & Merz, B. (2018). The value of hydrograph partitioning curves for calibrating hydrological models in glacierized basins. *Water Resources Research*, (pp. 1–52).

Heidbüchel, I., Troch, P. A., & Lyon, S. W. (2013). Separating physical and meteorological controls of variable transit times in zero-order catchments. *Water Resources Research*, *49*(11), 7644–7657.

Helgeson, H. C., Murphy, W. M., & Aagaard, P. (1984). Thermodynamic and kinetic constraints on reaction rates among minerals and aqueous solutions. ii. rate constants, effective surface area, and the hydrolysis of feldspar. *Geochimica et Cosmochimica Acta*, *48*(12), 2405–2432.

Hem, J. D. (1985). *Study and interpretation of the chemical characteristics of natural water*, vol. 2254. Department of the Interior, US Geological Survey.

Herman, F., Seward, D., Valla, P. G., Carter, A., Kohn, B., Willett, S. D., & Ehlers, T. A. (2013). Worldwide acceleration of mountain erosion under a cooling climate. *Nature*, *504*(7480), 423–426.

Herndon, E. M., Dere, A. L., Sullivan, P., Norris, D., Rynolds, B., & Brantley, S. L. (2015). Landscape heterogeneity drives contrasting concentration–discharge relationships in shale headwater catchments.

Hindshaw, R. S., Tipper, E. T., Reynolds, B. C., Lemarchand, E., Wiederhold, J. G., Magnusson, J., Bernasconi, S. M., Kretzschmar, R., & Bourdon, B. (2011). Hydrological control of stream water chemistry in a glacial catchment (damma glacier, switzerland). *Chemical Geology*, *285*(1-4), 215–230.

Hock, R. (1999). A distributed temperature-index ice- and snowrnelt model including potential direct solar radiation. *Journal of Glaciology*, *45*(149).

Hock, R. (2005). Glacier melt: a review of processes and their modelling. *Progress in physical geography*, *29*(3), 362–391.

Hodgkins, R., Tranter, M., & Dowdeswell, J. A. (1997). Solute provenance, transport and denudation in a high arctic glacierized catchment. *Hydrological Processes*, *11*(14), 1813–1832.

Hood, Eran, Williams, M. W., & Caine, N. (2003). Landscape controls on organic and

inorganic nitrogen leaching across an alpine/subalpine ecotone, green lakes valley, colorado front range. *Ecosystems*, *6*(1), 0031–0045.

Hood, E., & Scott, D. (2008). Riverine organic matter and nutrients in southeast alaska affected by glacial coverage. *Nature Geoscience*, *1*(9), 583–587.

Hood, J. L., Roy, J. W., & Hayashi, M. (2006). Importance of groundwater in the water balance of an alpine headwater lake. *Geophysical Research Letters*, *33*(13), 1–5.

Hooper, R. P. (2003). Diagnostic tools for mixing models of stream water chemistry. *Water Resources Research*, *39*(3).

Hooper, R. P., & Shoemaker, C. A. (1986). A Comparison of Chemical and Isotopic Hydrograph Separation. *Water Resources Research*, *22*(10), 1444–1454.

Huss, M., Bauder, A., Funk, M., & Hock, R. (2008). Determination of the seasonal mass balance of four Alpine glaciers since 1865. *Journal of Geophysical Research*, *113*(F1), F01015.

Huss, M., Funk, M., & Ohmura, A. (2009). Strong Alpine glacier melt in the 1940s due to enhanced solar radiation. *Geophysical Research Letters*, *36*(23), L23501.

Huss, M., & Hock, R. (2018). Global-scale hydrological response to future glacier mass loss. *Nature Climate Change*, *8*(2), 135–140.

Huth, A. K., Leydecker, A., Sickman, J. O., & Bales, R. C. (2004). A two-component hydrograph separation for three high-elevation catchments in the Sierra Nevada, California. *Hydrological Processes*, *18*(9), 1721–1733.

Huxman, T. E., Wilcox, B. P., Breshears, D. D., Scott, R. L., Snyder, K. A., Small, E. E., Hultine, K., Pockman, W. T., & Jackson, R. B. (2005). Ecohydrological implications of woody plant encroachment. *Ecology*, *86*(2), 308–319.

Ibarra, D. E., Caves, J. K., Moon, S., Thomas, D. L., Hartmann, J., Chamberlain, C. P., & Maher, K. (2016). Differential weathering of basaltic and granitic catchments from concentration–discharge relationships. *Geochimica et Cosmochimica Acta*, *190*, 265–293.

Immerzeel, W. W., van Beek, L. P. H., & Bierkens, M. F. P. (2010). Climate Change Will Affect the Asian Water Towers. *Science*, *328*(5984), 1382–1385.

INEC (2010). Cencos de Poblacion y Vivienda 2010. *Quito, Ecuador*.

IPCC, C. C. (2007). Impacts, adaptation and vulnerability. contribution of working group ii to the fourth assessment report of the intergovernmental panel on climate change. *Intergovernmental Panel on Climate Change (IPCC), Cambridge University Press, New York*.

James, A. L., & Roulet, N. T. (2006). Investigating the applicability of end–member mixing analysis (EMMA) across scale: A study of eight small, nested catchments in a temperate forested watershed. *Water Resources Research*, *42*(8).

Jansson, P., Hock, R., & Schneider, T. (2003). The concept of glacier storage: a review. *Journal of Hydrology*, *282*(1-4), 116–129.

Johnson, N. M., Likens, G. E., Bormann, F., Fisher, D., & Pierce, R. (1969). A working model for the variation in stream water chemistry at the hubbard brook experimental forest, new hampshire. *Water Resources Research*, *5*(6), 1353–1363.

Juen, I., Kaser, G., & Georges, C. (2007). Modelling observed and future runoff from a glacierized tropical catchment (Cordillera Blanca, Perú). *Global and Planetary Change*, *59*(1-4), 37–48.

Jump, A. S., Huang, T. J., & Chou, C. H. (2012). Rapid altitudinal migration of mountain plants in Taiwan and its implications for high altitude biodiversity. *Ecography*, *35*(3), 204–210.

Kaser, G. (1999). A review of the modern fluctuations of tropical glaciers. *Global and Planetary Change*, *22*(1-4), 93–103.

Kaser, G., & Osmaston, H. (2002). *Tropical glaciers*. Cambridge University Press.

Katsuyama, M., Tani, M., & Nishimoto, S. (2010). Connection between streamwater mean residence time and bedrock groundwater recharge/discharge dynamics in weathered granite catchments. *Hydrological Processes*, *24*(16), 2287–2299.

Kendall, C., Doctor, D., Drever, J., Holland, H., & Turekian, K. (2003). Stable isotope applications in hydrological studies. (pp. 319–364).

Kim, H., Bishop, J. K., Dietrich, W. E., & Fung, I. Y. (2014). Process dominance shift in solute chemistry as revealed by long-term high-frequency water chemistry observations of groundwater flowing through weathered argillite underlying a steep forested hillslope. *Geochimica et Cosmochimica Acta*, *140*, 1–19.

Kim, H., Dietrich, W. E., Thurnhoffer, B. M., Bishop, J. K., & Fung, I. Y. (2017). Controls on solute concentration-discharge relationships revealed by simultaneous hydrochemistry observations of hillslope runoff and stream flow: The importance of critical zone structure. *Water Resources Research*, *53*(2), 1424–1443.

Kirchner, J. W., & Neal, C. (2013). Universal fractal scaling in stream chemistry and its implications for solute transport and water quality trend detection. *Proceedings of the National Academy of Sciences*, *110*(30), 12213–12218.

Knoop, W., & Walker, B. (1985). Interactions of woody and herbaceous vegetation in a southern african savanna. *The Journal of Ecology*, (pp. 235–253).

Kumar, N., Ramanathan, A., Tranter, M., Sharma, P., Pandey, M., Ranjan, P., & Raju, N. J. (2019). Switch in chemical weathering caused by the mass balance variability in a himalayan glacierized basin: a case of chhota shigri glacier. *Hydrological sciences journal*, *64*(2), 179–189.

Kumar, S., Holmes, T., Mocko, D. M., Wang, S., & Peters-Lidard, C. (2018). Attribution of flux partitioning variations between land surface models over the continental us. *Remote Sensing*, *10*(5), 751.

La Frenierre, J. (2014). Assessing the Hydrologic Implications of Glacier Recession and the Potential for Water Resources Vulnerability at Volcán Chimborazo, Ecuador. *Ph.D. dissertation, Ohio State University*.

La Frenierre, J., & Mark, B. G. (2017). Detecting Patterns of Climate Change at Volcán Chimborazo, Ecuador, by Integrating Instrumental Data, Public Observations, and Glacier Change Analysis. *Annals of the American Association of Geographers*, *107*(4), 979–997.

Lamprecht, A., Semenchuk, P. R., Steinbauer, K., Winkler, M., & Pauli, H. (2018). Climate change leads to accelerated transformation of high-elevation vegetation in the central alps. *New Phytologist*, *220*(2), 447–459.

Lang, H. (1986). Forecasting Meltwater Runoff from Snow-Covered Areas and from Glacier Basins. (pp. 99–127). Dordrecht: Springer Netherlands.

Lasaga, A. C. (1984). Chemical kinetics of water-rock interactions. *Journal of geophysical research: solid earth*, *89*(B6), 4009–4025.

Lauer, W. (1981). Ecoclimatological conditions of the paramo belt in the tropical high mountains. *Mountain Research and Development*, (pp. 209–221).

Lenoir, J., Gégout, J.-C., Marquet, P., De Ruffray, P., & Brisse, H. (2008). A significant upward shift in plant species optimum elevation during the 20th century. *science*, *320*(5884), 1768–1771.

Lewis, T., Lafrenière, M. J., & Lamoureux, S. F. (2012). Hydrochemical and sedimentary responses of paired high arctic watersheds to unusual climate and permafrost disturbance, cape bounty, melville island, canada. *Hydrological Processes*, *26*(13), 2003–2018.

Li, Li, Bao, C., Sullivan, P. L., Brantley, S., Shi, Y., & Duffy, C. (2017b). Understanding watershed hydrogeochemistry: 2. synchronized hydrological and geochemical processes drive stream chemostatic behavior. *Water Resources Research*, *53*, 2346–2367.

Li, Li, Maher, K., Navarre-Sitchler, A., Druhan, J., Meile, C., Lawrence, C., Moore, J., Perdrial, J., Sullivan, P., Thompson, A., et al. (2017a). Expanding the role of reactive transport models in critical zone processes. *Earth-science reviews*, *165*, 280–301.

Liu, F., Williams, M. W., & Caine, N. (2004). Source waters and flow paths in an alpine catchment, Colorado Front Range, United States. *Water Resources Research*, *40*(9), 1–16.

Lloret, E., Dessert, C., Pastor, L., Lajeunesse, E., Crispi, O., Gaillardet, J., & Benedetti, M. (2013). Dynamic of particulate and dissolved organic carbon in small volcanic mountainous tropical watersheds. *Chemical Geology*, *351*, 229–244.

Loheide, S. P., Deitchman, R. S., Cooper, D. J., Wolf, E. C., Hammersmark, C. T., & Lundquist, J. D. (2009). A framework for understanding the hydroecology of impacted wet meadows in the Sierra Nevada and Cascade Ranges, California, USA. *Hydrogeology Journal*, *17*(1), 229–246.

Lowry, C. S., Deems, J. S., Loheide II, S. P., & Lundquist, J. D. (2010). Linking snowmelt-derived fluxes and groundwater flow in a high elevation meadow system, Sierra Nevada Mountains, California. *Hydrological Processes*, *24*(20), 2821–2833.

Lowry, C. S., Loheide, S. P., Moore, C. E., & Lundquist, J. D. (2011). Groundwater controls on vegetation composition and patterning in mountain meadows. *Water Resources Research*, *47*(10), 1–16.

Luce, C. H. (2018). Effects of Climate Change on Snowpack, Glaciers, and Water Resources in the Northern Rockies. (pp. 25–36). Cham: Springer International Publishing.

Luteyn, J. L., & Balslev, H. (1992). *Páramo: an Andean ecosystem under human influence*. Academic Press London, UK.

Mackay, A. (2008). Climate Change 2007: Impacts, Adaptation and Vulnerability. Contribution of Working Group II to the Fourth Assessment Report of the Intergovernmental Panel on Climate Change. *Journal of Environment Quality*, *37*(6), 2407.

Maher, K. (2011). The role of fluid residence time and topographic scales in determining chemical fluxes from landscapes. *Earth and Planetary Science Letters*, *312*(1-2), 48–58.

Maher, K., & Chamberlain, C. (2014). Hydrologic regulation of chemical weathering and the geologic carbon cycle. *science*, *343*(6178), 1502–1504.

Mahrt, L., & Ek, M. (1984). The influence of atmospheric stability on potential evaporation. *Journal of Applied Meteorology and Climatology*, *23*(2), 222–234.

Manciati, C., Villacís, M., Taupin, J.-D., Cadier, E., Galárraga-Sánchez, R., & Cáceres,

B. (2014). Empirical mass balance modelling of South American tropical glaciers: case study of Antisana volcano, Ecuador. *Hydrological Sciences Journal*, *59*(8), 1519–1535.

Mark, B. G. (2008). Tracing tropical Andean glaciers over space and time: Some lessons and transdisciplinary implications. *Global and Planetary Change*, *60*(1-2), 101–114.

Mark, B. G., & Mckenzie, J. M. (2007). Tracing Increasing Tropical Andean Glacier Melt with Stable Isotopes in Water. *Environmental Science & Technology*, *41*(20), 6955–6960.

Mark, B. G., McKenzie, J. M., & Gómez, J. (2005). Hydrochemical evaluation of changing glacier meltwater contribution to stream discharge: Callejon de Huaylas, Peru / Evaluation hydrochimique de la contribution évolutive de la fonte glaciaire à l'écoulement fluvial: Callejon de Huaylas, Pérou. *Hydrological Sciences Journal*, *50*(6), 975–988.

Mark, B. G., & Seltzer, G. O. (2003). Tropical glacier meltwater contribution to stream discharge: a case study in the Cordillera Blanca, Peru. *Journal of Glaciology*, *49*(165), 271–281.

Markovich, K. H., Maxwell, R. M., & Fogg, G. E. (2016). Hydrogeological response to climate change in alpine hillslopes. *Hydrological Processes*, *30*(18), 3126–3138.

Maussion, F., Gurgiser, W., Großhauser, M., Kaser, G., & Marzeion, B. (2015). ENSO influence on surface energy and mass balance at Shallap Glacier, Cordillera Blanca, Peru. *The Cryosphere*, *9*(4), 1663–1683.

Mayer, K. U., Frind, E. O., & Blowes, D. W. (2002). Multicomponent reactive transport modeling in variably saturated porous media using a generalized formulation for kinetically controlled reactions. *Water Resources Research*, *38*(9), 13–1.

McClain, M. E., & Naiman, R. J. (2008). Andean influences on the biogeochemistry and ecology of the amazon river. *BioScience*, *58*(4), 325–338.

McGuire, K., McDonnell, J. J., Weiler, M., Kendall, C., McGlynn, B., Welker, J., & Seibert, J. (2005). The role of topography on catchment-scale water residence time. *Water Resources Research*, *41*(5).

McLaughlin, R. (2017). *Hydrochemical Signatures of Glacial Meltwater on Volcán Chimborazo, Ecuador*. Ph.D. thesis.

Merritts, D. J., Chadwick, O. A., Hendricks, D. M., Brimhall, G. H., & Lewis, C. J. (1992). The mass balance of soil evolution on late quaternary marine terraces, northern california. *Geological Society of America Bulletin*, *104*(11), 1456–1470.

Messerli, B., Viviroli, D., & Weingartner, R. (2004). Mountains of the World: Vulnerable Water Towers for the 21st Century. *AMBIO Special Report*, *13*(December 2004), 29–34.

Miller, N. L., Bashford, K. E., & Strem, E. (2003). Potential impacts of climate change on california hydrology 1. *JAWRA Journal of the American Water Resources Association*, *39*(4), 771–784.

Milner, A. M., Khamis, K., Battin, T. J., Brittain, J. E., Barrand, N. E., Füreder, L., Cauvy-Fraunié, S., Gíslason, G. M., Jacobsen, D., Hannah, D. M., et al. (2017). Glacier shrinkage driving global changes in downstream systems. *Proceedings of the National Academy of Sciences*, *114*(37), 9770–9778.

Minaya, V. G., Maldonado (2016). Ecohydrology of the Andes Páramo Region. *PhD diss., IHE Delft Institute for Water Education*.

Molina, A., Vanacker, V., Corre, M. D., & Veldkamp, E. (2019). Patterns in soil chemical weathering related to topographic gradients and vegetation structure in a high andean tropical ecosystem. *Journal of Geophysical Research: Earth Surface*, *124*(2), 666–685.

Montzka, C., Herbst, M., Weihermüller, L., Verhoef, A., & Vereecken, H. (2017). A global data set of soil hydraulic properties and sub-grid variability of soil water retention and hydraulic conductivity curves. *Earth System Science Data*, *9*(2), 529–543.

Moquet, J.-S., Guyot, J.-L., Morera, S., Crave, A., Rau, P., Vauchel, P., Lagane, C., Sondag, F., Lavado, C. W., Pombosa, R., et al. (2018). Temporal variability and annual budget of inorganic dissolved matter in andean pacific rivers located along a climate gradient from northern ecuador to southern peru. *Comptes Rendus Geoscience*, *350*(1-2), 76–87.

Moret, P., Muriel, P., Jaramillo, R., & Dangles, O. (2019). Humboldts tableau physique revisited. *Proceedings of the National Academy of Sciences*, *116*(26), 12889–12894.

Moriasi, D. N., Arnold, J. G., Van Liew, M. W., Bingner, R. L., Harmel, R. D., & Veith, T. L. (2007). Model evaluation guidelines for systematic quantification of accuracy in watershed simulations. *Transactions of the ASABE*, *50*(3), 885–900.

Morueta-Holme, N., Engemann, K., Sandoval-Acuña, P., Jonas, J. D., Segnitz, R. M., & Svenning, J.-C. (2015). Strong upslope shifts in Chimborazo's vegetation over two centuries since Humboldt. *Proceedings of the National Academy of Sciences*, *112*(41), 12741–12745.

Mulligan, M. (2013). Waterworld: a self-parameterising, physically based model for application in data-poor but problem-rich environments globally. *Hydrology Research*, *44*(5), 748–769.

Nash, J., & Sutcliffe, J. (1970). River forecasting using conceptual models: Part 1-a discussion of principles. *Journal of Hydrology*, *10*(3), 280–290.

Nédeltcheva, T., Piedallu, C., Gégout, J.-C., Stussi, J.-M., Boudot, J.-P., Angeli, N., & Dambrine, E. (2006). Influence of granite mineralogy, rainfall, vegetation and relief on stream water chemistry (vosges mountains, north-eastern france). *Chemical Geology*, *231*(1-2), 1–15.

Neilson, R. P., & Marks, D. (1994). A global perspective of regional vegetation and hydrologic sensitivities from climatic change. *Journal of vegetation science*, *5*(5), 715–730.

Neilson, R. P., Pitelka, L. F., Solomon, A. M., Nathan, R., Midgley, G. F., Fragoso, J. M., Lischke, H., & Thompson, K. (2005). Forecasting regional to global plant migration in response to climate change. *Bioscience*, *55*(9), 749–759.

Ng, G.-H. C., Wickert, A. D., Somers, L. D., Saberi, L., Cronkite-Ratcliff, C., Niswonger, R. G., & McKenzie, J. M. (2018). GSFLOW-GRASS v1. 0.0: GIS-enabled hydrologic modeling of coupled groundwater–surface-water systems. *Manuscript under review for journal Geosci. Model Dev.*.

NRCS, U. (2009). Part 630 Hydrology National Engineering Handbook.

Ochoa-Tocachi, B., Buytaert, W., De Bievre, B., Celleri, R., Crespo, P., Villacs, M., Llerena, C. A., Acosta, L., Villazn, M., Guallpa, M., Gil-Ros, J., Fuentes, P., Olaya, D., Vias, P., Rojas, G., & Arias, S. (2016a). Impacts of land use on the hydrological response of tropical Andean catchments. *Hydrological Processes*, *30*(22), 4074–4089.

Ochoa-Tocachi, B. F., Buytaert, W., De Bièvre, B., Célleri, R., Crespo, P., Villacís, M., Llerena, C. A., Acosta, L., Villazón, M., Guallpa, M., Gil-Ríos, J., Fuentes, P., Olaya, D., Viñas, P., Rojas, G., & Arias, S. (2016b). Impacts of land use on the hydrological response of tropical Andean catchments. *Hydrological Processes*, *30*(22), 4074–4089.

Omani, N., Srinivasan, R., Smith, P. K., & Karthikeyan, R. (2017). Glacier mass balance simulation using SWAT distributed snow algorithm. *Hydrological Sciences Journal*, *62*(4), 546–560.

O'Neil-Dunne, J. P., MacFaden, S. W., Royar, A. R., & Pelletier, K. C. (2013). An object-based system for lidar data fusion and feature extraction. *Geocarto International*, *28*(3), 227–242.

Ostheimer, G. J., Hadjivasiliou, H., Kloer, D. P., Barkan, A., & Matthews, B. W. (2005a). Structural analysis of the group ii intron splicing factor crs2 yields insights into its protein and rna interaction surfaces. *Journal of molecular biology*, *345*(1), 51–68.

Ostheimer, G. J., Hadjivasiliou, H., Kloer, D. P., Barkan, A., & Matthews, B. W. (2005b). Structural Analysis of the Group II Intron Splicing Factor CRS2 Yields Insights into its Protein and RNA Interaction Surfaces. *Journal of Molecular Biology*, *345*(1), 51–68.

Parkhurst, D. L., Appelo, C., et al. (1999). User's guide to phreeqc (version 2): A computer program for speciation, batch-reaction, one-dimensional transport, and inverse geochemical calculations. *Water-resources investigations report*, *99*(4259), 312.

Pellicciotti, F., Brock, B., Strasser, U., Burlando, P., Funk, M., & Corripio, J. (2005). An enhanced temperature-index glacier melt model including the shortwave radiation

balance: development and testing for Haut Glacier dArolla, Switzerland. *Journal of Glaciology*, *51*(175), 573–587.

Pepin, N., Bradley, R. S., Diaz, H. F., Baraer, M., Caceres, E. B., Forsythe, N., Fowler, H., Greenwood, G., Hashmi, M. Z., Liu, X. D., Miller, J. R., Ning, L., Ohmura, A., Palazzi, E., Rangwala, I., Schöner, W., Severskiy, I., Shahgedanova, M., Wang, M. B., Williamson, S. N., & Yang, D. Q. (2015). Elevation-dependent warming in mountain regions of the world. *Nature Climate Change*, *5*(5), 424–430.

Podwojewski, P., Poulenard, J., Zambrana, T., & Hofstede, R. (2002). Overgrazing effects on vegetation cover and properties of volcanic ash soil in the pàramo of Llangahua and al Esperanza (Tungurahua, Ecuador). *Management*, *18*, 45–55.

Pohl, E., Knoche, M., Gloaguen, R., Andermann, C., & Krause, P. (2015). Sensitivity analysis and implications for surface processes from a hydrological modelling approach in the Gunt catchment, high Pamir Mountains. *Earth Surface Dynamics*, *3*(3), 333–362.

Polk, M. H., Young, K. R., Baraer, M., Mark, B. G., McKenzie, J. M., Bury, J., & Carey, M. (2017). Exploring hydrologic connections between tropical mountain wetlands and glacier recession in Peru's Cordillera Blanca. *Applied Geography*, *78*(January), 94–103.

Poppe, L., Paskevich, V., Hathaway, J., & Blackwood, D. (2001). A laboratory manual for x-ray powder diffraction. *US Geological Survey open-file report*, *1*(041), 1–88.

Pribulick, C. E., Foster, L. M., Bearup, L. A., Navarre-Sitchler, A. K., Williams, K. H., Carroll, R. W., & Maxwell, R. M. (2016). Contrasting the hydrologic response due to land cover and climate change in a mountain headwaters system. *Ecohydrology*, *9*(8), 1431–1438.

Prommer, H., Barry, D., & Zheng, C. (2003). Pht3d-a modflow/mt3dms based reactive multi-component transport model. *Ground Water*, *42*(2), 247–257.

Qu, Y., & Duffy, C. J. (2007). A semidiscrete finite volume formulation for multiprocess watershed simulation. *Water Resources Research*, *43*(8), 1–18.

Rabatel, A., Francou, B., Soruco, A., Gomez, J., Cáceres, B., Ceballos, J. L., Basantes, R., Vuille, M., Sicart, J.-E., Huggel, C., Scheel, M., Lejeune, Y., Arnaud, Y., Collet, M., Condom, T., Consoli, G., Favier, V., Jomelli, V., Galarraga, R., Ginot, P., Maisincho, L., Mendoza, J., Ménégoz, M., Ramirez, E., Ribstein, P., Suarez, W., Villacis, M., & Wagnon, P. (2013). Current state of glaciers in the tropical Andes: a multi-century perspective on glacier evolution and climate change. *The Cryosphere*, *7*(1), 81–102.

Rasouli, K., Pomeroy, J. W., & Whitfield, P. H. (2019). Are the effects of vegetation and soil changes as important as climate change impacts on hydrological processes? *Hydrology and Earth System Sciences*, *23*(12), 4933–4954.

Reveillet, M., Vincent, C., Six, D., & Rabatel, A. (2017). Which empirical model is best suited to simulate glacier mass balances? *Journal of Glaciology*, *63*(237), 39–54.

Rodell, M., Houser, P. R., Jambor, U. E. A., Gottschalck, J., Mitchell, K., Meng, C. J., Arsenault, K., Cosgrove, B., Radakovich, J., & Bosilovich, M. (2004). The global land data assimilation system. *Bulletin of the American Meteorological Society*, *85*(3), 381–394.

Romero-Mujalli, G., Hartmann, J., Börker, J., Gaillardet, J., & Calmels, D. (2019). Ecosystem controlled soil-rock pco2 and carbonate weathering–constraints by temperature and soil water content. *Chemical Geology*, *527*, 118634.

Ryu, J.-S., Lee, K.-S., & Chang, H.-W. (2007). Hydrochemistry and isotope geochemistry of Song Stream, a headwater tributary of the South Han River, South Korea. *Geosciences Journal*, *11*(2), 157–164.

Saberi, L., Crystal Ng, G.-H., Nelson, L., Zhi, W., Li, L., La Frenierre, J., & Johnstone, M. (2020). Spatiotemporal drivers of hydrochemical variability in a tropical glacierized watershed in the andes. *Water Resources Research*, (p. e2020WR028722).

Saberi, L., McLaughlin, R. T., Crystal Ng, G., La Frenierre, J., Wickert, A. D., Baraer, M., Zhi, W., Li, L., & Mark, B. G. (2019). Multi-scale temporal variability in meltwater contributions in a tropical glacierized watershed. *Hydrology and Earth System Sciences*, *23*(1), 405–425.

Salve, R., Rempe, D. M., & Dietrich, W. E. (2012). Rain, rock moisture dynamics, and the rapid response of perched groundwater in weathered, fractured argillite underlying a steep hillslope. *Water Resources Research*, *48*(11).

Samaniego, P., Barba, D., Robin, C., Fornari, M., & Bernard, B. (2012). Eruptive history of Chimborazo volcano (Ecuador): A large, ice-capped and hazardous compound volcano in the Northern Andes. *Journal of Volcanology and Geothermal Research*, *221-222*, 33–51.

Sarmiento, L. (2000). Water Balance and Soil Loss under Long Fallow Agriculture in the Venezuelan Andes. *Mountain Research and Development*, *20*(3), 246–253.

Schilling, O. S., Cook, P. G., & Brunner, P. (2019). Beyond classical observations in hydrogeology: The advantages of including exchange flux, temperature, tracer concentration, residence time, and soil moisture observations in groundwater model calibration. *Reviews of Geophysics*, *57*(1), 146–182.

Schlesinger, W., & Bernhardt, E. (2013). Biogeochemistry: An analysis of global change. edn 15–48.

Schlesinger, W. H., Reynolds, J. F., Cunningham, G. L., Huenneke, L. F., Jarrell, W. M., Virginia, R. A., & Whitford, W. G. (1990). Biological feedbacks in global desertification. *Science*, *247*(4946), 1043–1048.

Schmieder, J., Garvelmann, J., Marke, T., & Strasser, U. (2018). Spatio-temporal tracer variability in the glacier melt end-member - How does it affect hydrograph separation results? *Hydrological Processes*, *2016*.

Schreiner-McGraw, A. P., Vivoni, E. R., Ajami, H., Sala, O. E., Throop, H. L., & Peters, D. P. (2020). Woody plant encroachment has a larger impact than climate change on dryland water budgets. *Scientific reports*, *10*(1), 1–9.

Shanley, J. B., McDowell, W. H., & Stallard, R. F. (2011). Long-term patterns and short-term dynamics of stream solutes and suspended sediment in a rapidly weathering tropical watershed. *Water Resources Research*, *47*(7).

Shi, Y., Davis, K. J., Duffy, C. J., & Yu, X. (2013). Development of a Coupled Land Surface Hydrologic Model and Evaluation at a Critical Zone Observatory. *Journal of Hydrometeorology*, *14*(5), 1401–1420.

Shoji, S., Nanzyo, M., & Dahlgren, R. (1994). *Volcanic ash soils: genesis, properties and utilization*. Elsevier.

Sicart, J. E., Hock, R., & Six, D. (2008). Glacier melt, air temperature, and energy balance in different climates: The Bolivian Tropics, the French Alps, and northern Sweden. *Journal of Geophysical Research*, *113*(D24), D24113.

Smith, J. A., Mark, B. G., & Rodbell, D. T. (2008a). The timing and magnitude of mountain glaciation in the tropical Andes. *Journal of Quaternary Science*, *23*(6-7), 609–634.

Smith, J. A., Mark, B. G., & Rodbell, D. T. (2008b). The timing and magnitude of mountain glaciation in the tropical andes. *Journal of Quaternary Science: Published for the Quaternary Research Association*, *23*(6-7), 609–634.

Somers, L. D., Gordon, R. P., McKenzie, J. M., Lautz, L. K., Wigmore, O., Glose, A. M., Glas, R., Aubry-Wake, C., Mark, B., Baraer, M., & Condom, T. (2016). Quantifying groundwater–surface water interactions in a proglacial valley, Cordillera Blanca, Peru. *Hydrological Processes*, *30*(17), 2915–2929.

Somers, L. D., McKenzie, J. M., Mark, B. G., Lagos, P., Ng, G.-H. C., Wickert, A. D., Yarleque, C., Baraër, M., & Silva, Y. (2019). Groundwater buffers decreasing glacier melt in an andean watershed, but not forever. *Geophysical Research Letters*, *46*(22), 13016–13026.

Soruco, A., Vincent, C., Rabatel, A., Francou, B., Thibert, E., Sicart, J. E., & Condom, T. (2015). Contribution of glacier runoff to water resources of La Paz city, Bolivia (16° S). *Annals of Glaciology*, *56*(70), 147–154.

Soulsby, C., Petry, J., Brewer, M., Dunn, S., Ott, B., & Malcolm, I. (2003). Identifying and assessing uncertainty in hydrological pathways: a novel approach to end member mixing in a Scottish agricultural catchment. *Journal of Hydrology*, *274*(1-4), 109–128.

Stachnik, Ł., Majchrowska, E., Yde, J. C., Nawrot, A. P., Cichała-Kamrowska, K., Ignatiuk, D., & Piechota, A. (2016). Chemical denudation and the role of sulfide oxidation at werenskioldbreen, svalbard. *Journal of Hydrology*, *538*, 177–193.

Stallard, & Edmond (1983). Geochemistry of the amazon: 2. the influence of geology and weathering environment on the dissolved load. *Journal of Geophysical Research: Oceans*, *88*(C14), 9671–9688.

Stallard, Robert, & Murphy, S. (2014). A unified assessment of hydrologic and biogeochemical responses in research watersheds in eastern puerto rico using runoff–concentration relations. *Aquatic geochemistry*, *20*(2-3), 115–139.

Starks, P., & Moriasi, D. (2017). Impact of eastern redcedar encroachment on stream discharge in the north canadian river basin. *Journal of Soil and Water Conservation*, *72*(1), 12–25.

Steefel, C. I., Appelo, C., Arora, B., Jacques, D., Kalbacher, T., Kolditz, O., Lagneau, V., Lichtner, P., Mayer, K. U., Meeussen, J., et al. (2015). Reactive transport codes for subsurface environmental simulation. *Computational Geosciences*, *19*(3), 445–478.

Steefel, C. I., & Maher, K. (2009). Fluid-rock interaction: A reactive transport approach. *Reviews in mineralogy and geochemistry*, *70*(1), 485–532.

Stern, C. R. (2004). Active andean volcanism: its geologic and tectonic setting. *Revista geológica de Chile*, *31*(2), 161–206.

Stocker, T., Qin, D., Plattner, G., Tignor, M., Allen, S., Boschung, J., Nauels, A., Xia, Y., Bex, V., & Midgley, P. (2013). Ipcc, 2013. *Climate change*.

Suecker, J. K., Ryan, J. N., Kendall, C., & Jarrett, R. D. (2000). Determination of hydrologic pathways during snowmelt for alpine/subalpine basins, Rocky Mountain National Park, Colorado. *Water Resources Research*, *36*(1), 63–75.

Tague, C., Grant, G., Farrell, M., Choate, J., & Jefferson, A. (2008). Deep groundwater mediates streamflow response to climate warming in the Oregon Cascades. *Climatic Change*, *86*(1-2), 189–210.

Tague, C., & Grant, G. E. (2009). Groundwater dynamics mediate low-flow response to global warming in snow-dominated alpine regions. *Water Resources Research*, *45*(7), 1–12.

Takahashi, T., & Shoji, S. (2002). Distribution and classification of volcanic ash soils. *GLOBAL ENVIRONMENTAL RESEARCH-ENGLISH EDITION-*, *6*(2), 83–98.

Tetzlaff, D., Seibert, J., McGuire, K., Laudon, H., Burns, D. A., Dunn, S., & Soulsby, C. (2009). How does landscape structure influence catchment transit time across different geomorphic provinces? *Hydrological Processes: An International Journal*, *23*(6), 945–953.

Thompson, L., Mosley-Thompson, E., Davis, M., & Brecher, H. (2011). Tropical Glacier, Records and Indicator of Climate Change, Are Disappearing Globally. *Annals of Glaciology*, *52*(59), 23–34.

Tipper, E. T., Bickle, M. J., Galy, A., West, A. J., Pomiès, C., & Chapman, H. J. (2006). The short term climatic sensitivity of carbonate and silicate weathering fluxes: insight from seasonal variations in river chemistry. *Geochimica et Cosmochimica Acta*, *70*(11), 2737–2754.

Torres, M. A., Moosdorf, N., Hartmann, J., Adkins, J. F., & West, A. J. (2017). Glacial weathering, sulfide oxidation, and global carbon cycle feedbacks. *Proceedings of the National Academy of Sciences*, *114*(33), 8716–8721.

Torres, M. A., West, A. J., & Clark, K. E. (2015). Geomorphic regime modulates hydrologic control of chemical weathering in the andes–amazon. *Geochimica et Cosmochimica Acta*, *166*, 105–128.

Tranter, M. (2006). Sediment and solute transport in glacial meltwater streams. *Encyclopedia of Hydrological Sciences*.

Tranter, M., Brown, G. H., Hodson, A. J., & Gurnell, A. M. (1996). Hydrochemistry as an indicator of subglacial drainage system structure: a comparison of alpine and sub-polar environments. *Hydrological Processes*, *10*(4), 541–556.

Trudgill, S. T., et al. (1977). Soil and vegetation systems. *Soil and Vegetation Systems.*.

Ugolini, F. C., Dahlgren, R. A., et al. (2002). Soil development in volcanic ash. *GLOBAL ENVIRONMENTAL RESEARCH-ENGLISH EDITION-*, *6*(2), 69–82.

Urrutia, R., & Vuille, M. (2009). Climate change projections for the tropical andes using a regional climate model: Temperature and precipitation simulations for the end of the 21st century. *Journal of Geophysical Research: Atmospheres*, *114*(D2).

Van Der Lee, J., De Windt, L., Lagneau, V., & Goblet, P. (2003). Module-oriented modeling of reactive transport with hytec. *Computers & Geosciences*, *29*(3), 265–275.

Veettil, B. K., Bremer, U. F., de Souza, S. F., Maier, E. L. B., & Simões, J. C. (2016). Influence of ENSO and PDO on mountain glaciers in the outer tropics: case studies in Bolivia. *Theoretical and Applied Climatology*, *125*(3-4), 757–768.

Veettil, B. K., Leandro Bayer Maier, E., Bremer, U. F., & de Souza, S. F. (2014a). Combined influence of PDO and ENSO on northern Andean glaciers: a case study on the Cotopaxi ice-covered volcano, Ecuador. *Climate Dynamics*, *43*(12), 3439–3448.

Veettil, B. K., Maier, E. L. B., Bremer, U. F., & de Souza, S. F. (2014b). Combined influence of PDO and ENSO on northern Andean glaciers: a case study on the Cotopaxi ice-covered volcano, Ecuador. *Climate dynamics*, *43*(12), 3439–3448.

Vermote, E. (2015). MOD09A1 MODIS/Terra Surface Reflectance 8-Day L3 Global 500m SIN Grid V006. *NASA EOSDIS Land Processes DAAC*.

Viles, H. (1990). The agency of organic beings: A selective review of recent work in biogeomorphology. *Vegetation and Erosion*, (pp. 5–24).

Vuille, M., & Bradley, R. S. (2000). the tropical Andes. *Geophysical Research Letters*, *27*(23), 3885–3888.

Vuille, M., Bradley, R. S., & Keimig, F. (2000). Climate Variability in the Andes of Ecuador and Its Relation to Tropical Pacific and Atlantic Sea Surface Temperature Anomalies. *Journal of Climate*, *13*(14), 2520–2535.

Vuille, M., Bradley, R. S., Werner, M., & Keimig, F. (2003). 20th Century Climate Change in the Tropical Andes: Observations and Model Results. In *Climatic Change*, vol. 59, (pp. 75–99).

Vuille, M., Carey, M., Huggel, C., Buytaert, W., Rabatel, A., Jacobsen, D., Soruco, A., Villacis, M., Yarleque, C., Elison Timm, O., Condom, T., Salzmann, N., & Sicart, J.-E. (2018). Rapid decline of snow and ice in the tropical Andes: Impacts, uncertainties and challenges ahead. *Earth-Science Reviews*, *176*(November 2016), 195–213.

Vuille, M., Francou, B., Wagnon, P., Juen, I., Kaser, G., Mark, B. G., & Bradley, R. S. (2008). Climate change and tropical Andean glaciers: Past, present and future. *Earth-Science Reviews*, *89*(3-4), 79–96.

Vuille, M., & Keimig, F. (2004). Interannual Variability of Summertime Convective Cloudiness and Precipitation in the Central Andes Derived from ISCCP-B3 Data. *Journal of Climate*, *17*(17), 3334–3348.

Wagnon, P., Ribstein, P., Francou, B., & Sicart, J. E. (2001). Anomalous heat and mass budget of Glaciar Zongo , Bolivia , during the 1997 / 98 El Ni · o year. *Journal of Glaciology*, *47*(156), 21–28.

Walther, G.-R., Beißner, S., & Burga, C. A. (2005). Trends in the upward shift of alpine plants. *Journal of Vegetation Science*, *16*(5), 541.

Wang, X., Sun, L., Zhang, Y., & Luo, Y. (2016). Rationalization of altitudinal precipitation profiles in a data-scarce glacierized watershed simulation in the karakoram. *Water*, *8*(5), 186.

Wen, H., Perdrial, J., Abbott, B. W., Bernal, S., Dupas, R., Godsey, S. E., Harpold, A., Rizzo, D., Underwood, K., Adler, T., et al. (2020). Temperature controls production but hydrology regulates export of dissolved organic carbon at the catchment scale. *Hydrology and Earth System Sciences*, *24*(2), 945–966.

West, A. J. (2012). Thickness of the chemical weathering zone and implications for erosional and climatic drivers of weathering and for carbon-cycle feedbacks. *Geology*, *40*(9), 811–814.

White, A. F., Blum, A. E., Schulz, M. S., Vivit, D. V., Stonestrom, D. A., Larsen, M., Murphy, S. F., & Eberl, D. (1998). Chemical weathering in a tropical watershed, luquillo mountains, puerto rico: I. long-term versus short-term weathering fluxes. *Geochimica et Cosmochimica Acta*, *62*(2), 209–226.

Wickert, A. D. (2014). The ALog: Inexpensive, Open Source, Automated Data Collection in the Field. *The Bulletin of the Ecological Society of America*, *95*(2), 166–176.

Wickert, A. D., Sandell, C. T., Schulz, B., & Ng, G.-H. C. (2019). Open-source arduino-compatible data loggers designed for field research. *Hydrology and Earth System Sciences*, *23*(4), 2065–2076.

Wilcox, B. P. (2002). Shrub control and streamflow on rangelands: A process based viewpoint.

Williams, M. W., Hood, E., Molotch, N. P., Caine, N., Cowie, R., & Liu, F. (2015). The teflon basin myth: hydrology and hydrochemistry of a seasonally snow-covered catchment. *Plant Ecology & Diversity*, *8*(5-6), 639–661.

Wilson, A. M., Williams, M. W., Kayastha, R. B., & Racoviteanu, A. (2016). Use of a hydrologic mixing model to examine the roles of meltwater, precipitation and groundwater in the Langtang River basin, Nepal. *Annals of Glaciology*, *57*(71), 155–168.

Winnick, M. J., Carroll, R. W., Williams, K. H., Maxwell, R. M., Dong, W., & Maher, K. (2017). Snowmelt controls on concentration-discharge relationships and the balance of oxidative and acid-base weathering fluxes in an alpine catchment, e ast r iver, c olorado. *Water Resources Research*, *53*(3), 2507–2523.

Wlostowski, A., Gooseff, M., McKnight, D., & Lyons, W. (2018). Transit times and rapid chemical equilibrium explain chemostasis in glacial meltwater streams in the mcmurdo dry valleys, antarctica. *Geophysical Research Letters*, *45*(24), 13–322.

Wolery, T. J. (1992). Eq3/6, a software package for geochemical modeling of aqueous systems: package overview and installation guide (version 7.0).

Wosten, J. H. M., Lilly, A., Nemes, A., & Le Bas, C. (1999). Development and use of a database of hydraulic properties of European soils. *Geoderma*, *90*(3-4), 169–185.

Wymore, A. S., Brereton, R. L., Ibarra, D. E., Maher, K., & McDowell, W. H. (2017a). Critical zone structure controls concentration-discharge relationships and solute generation in forested tropical montane watersheds. *Water Resources Research*, *53*(7), 6279–6295.

Wymore, A. S., Brereton, R. L., Ibarra, D. E., Maher, K., & McDowell, W. H. (2017b). Critical zone structure controls concentration-discharge relationships and solute generation in forested tropical montane watersheds. *Water Resources Research*, *53*(7), 6279–6295.

Zakharova, E., Pokrovsky, O. S., Dupré, B., Gaillardet, J., & Efimova, L. (2007). Chemical weathering of silicate rocks in karelia region and kola peninsula, nw russia: assessing the effect of rock composition, wetlands and vegetation. *Chemical Geology*, *242*(1-2), 255–277.

Zhang, L., Dawes, W., & Walker, G. (2001). Response of mean annual evapotranspiration to vegetation changes at catchment scale. *Water resources research*, *37*(3), 701–708.

Zhang, Y., Slingerland, R., & Duffy, C. (2016). Fully-coupled hydrologic processes for modeling landscape evolution. *Environmental Modelling & Software*, *82*, 89–107.

Zhi, W., Li, L., Dong, W., Brown, W., Kaye, J., Steefel, C., & Williams, K. H. (2019). Distinct source water chemistry shapes contrasting concentration-discharge patterns. *Water Resources Research*, *55*(5), 4233–4251.

Zhi, W., Shi, Y., Wen, H., Saberi, L., Ng, G.-H. C., & Li, L. (2020). Biort-flux-pihm v1. 0: a watershed biogeochemical reactive transport model. *Geoscientific Model Development Discussions*, (pp. 1–41).

Appendix A

Supplemental Materials: Multi-scale temporal variability in meltwater contributions in a tropical glacierized watershed

A.1 Figures

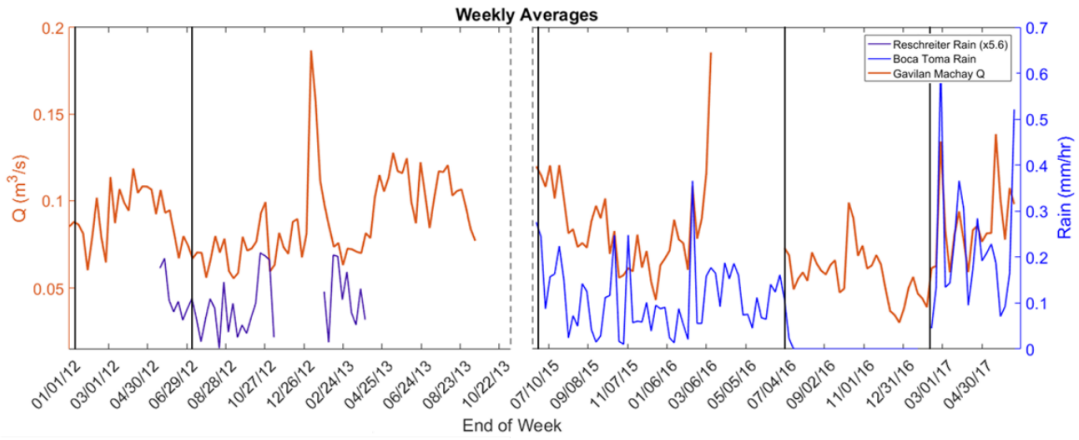

Figure A1: Comparison of average weekly discharge (m^3/s) at Gavilan Machay and rainfall (mm/hr) at Boca Toma. Vertical black dashed lines indicate weeks where sampling occurred. Despite gaps in data, it can be seen that precipitation was higher in the time surrounding the 2015 sampling campaign than in the times surrounding the other campaigns.

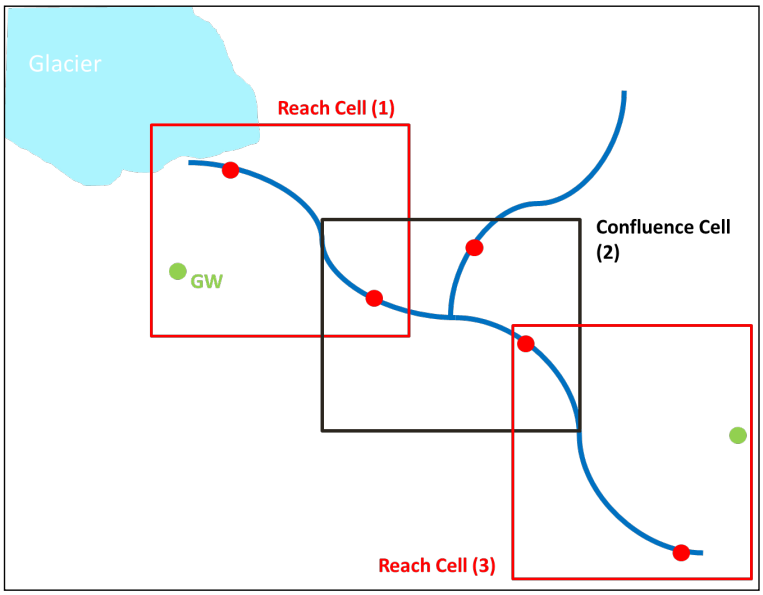

Figure A2: The reach and confluences cells relative to a stream system.

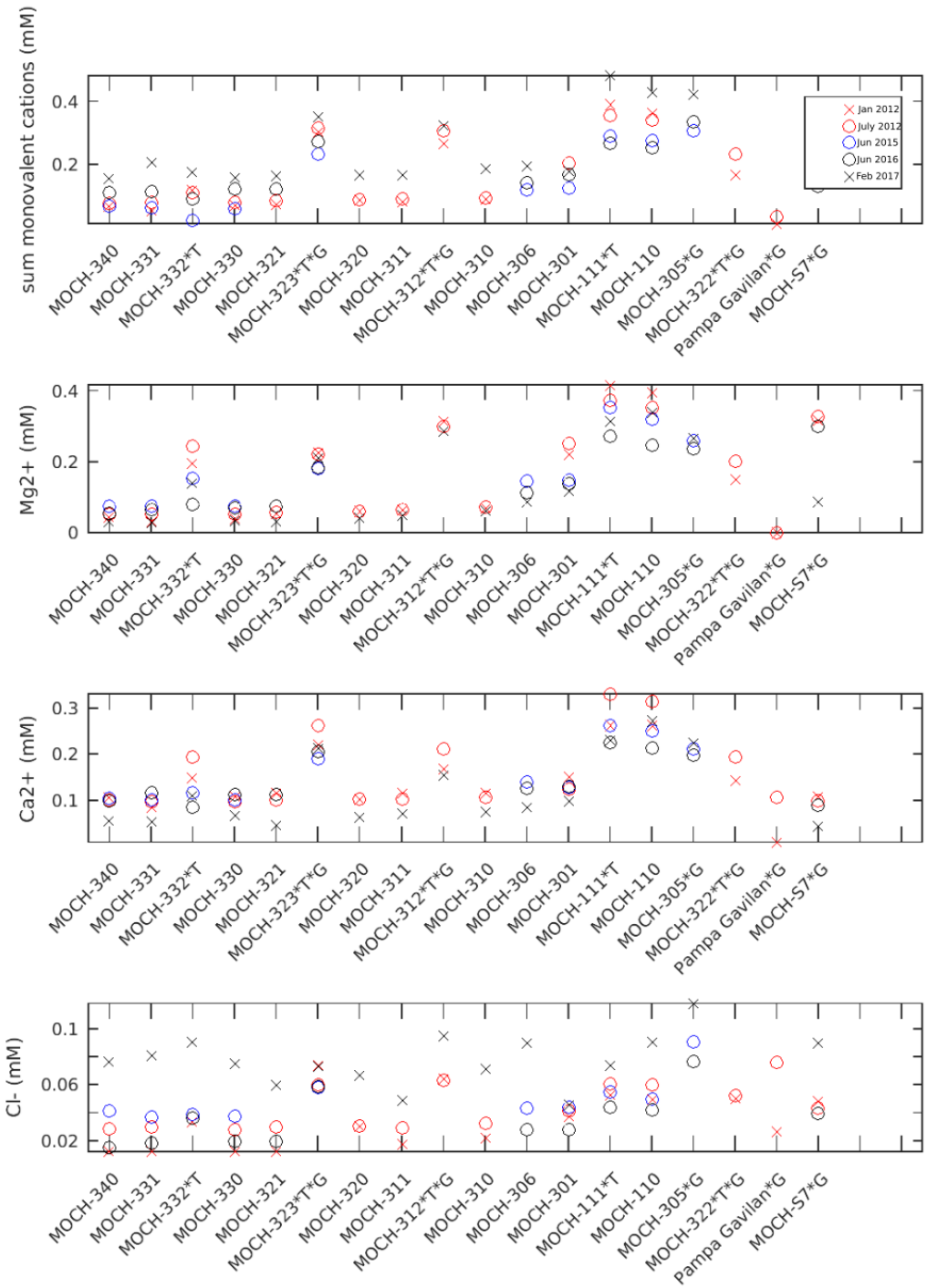

Figure A3: The concentrations of anions and cations across the different sampling periods.

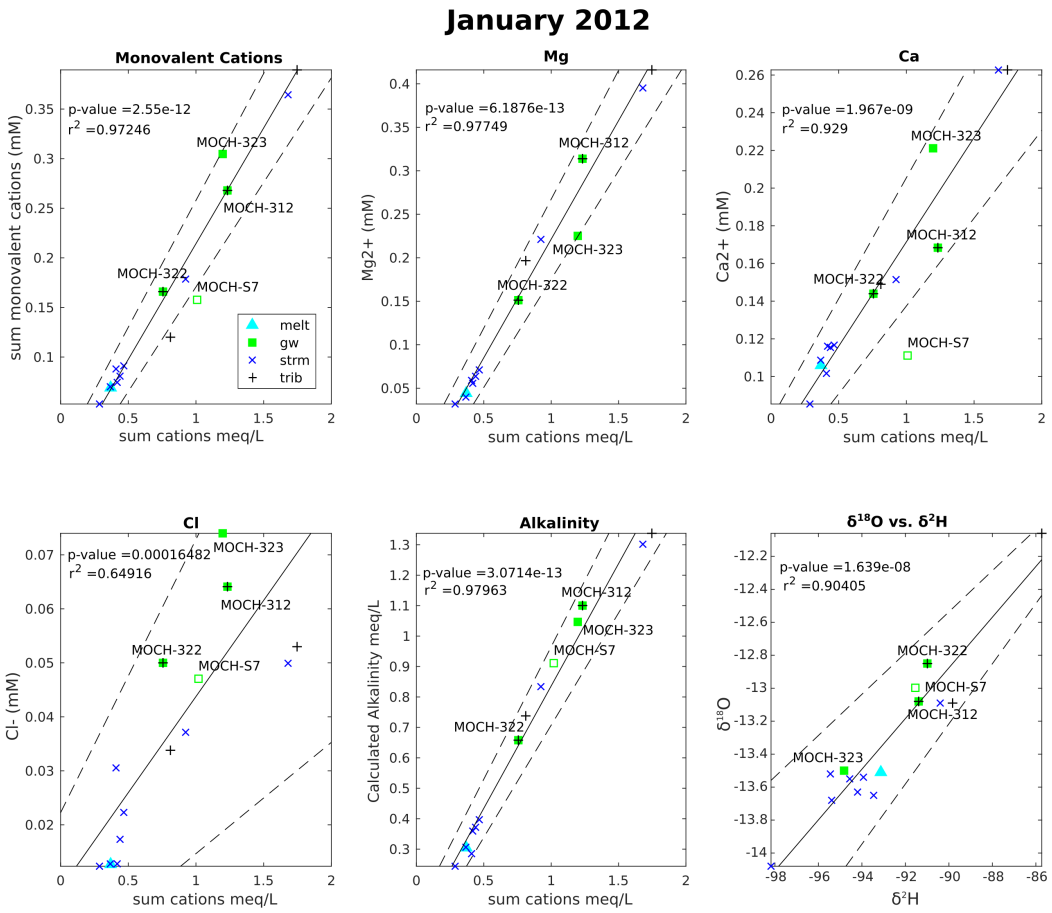

Figure A4: Bivariate diagrams of tracers selected for January 2012 analysis. The solid black lines represent linear regressions through all samples and dashed black lines indicated the regressions' 95% confidence intervals. Samples from the main Rio Mocha channel before and after the Gavilan stream joins it (filled green circles) consistently plot outside or away from the mixing line created between groundwater and meltwater. MOCH-S7 was not considered in the analysis (shown with hallow square). These samples are also responsible for the poor R2 and p-values of sulfate and chloride.

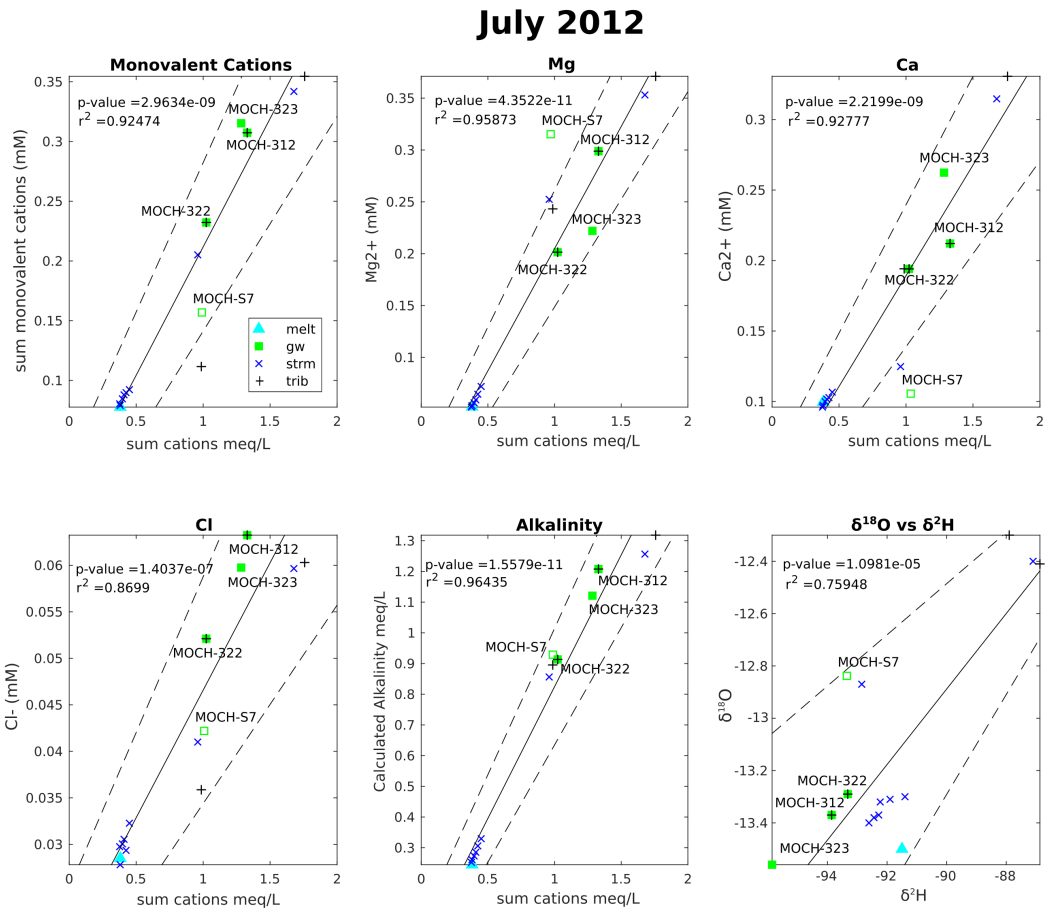

Figure A5: Bivariate diagrams of tracers selected for July 2012 analysis. The solid black lines represent linear regressions through all samples and dashed black lines indicated the regressions' 95% confidence intervals. Samples from the main Rio Mocha channel before and after the Gavilan stream joins it (filled green circles) consistently plot outside or away from the mixing line created between groundwater and meltwater. MOCH-S7 was not considered in the analysis (shown with hollow square). These samples are also responsible for the poor R2 and p-values of sulfate and chloride.

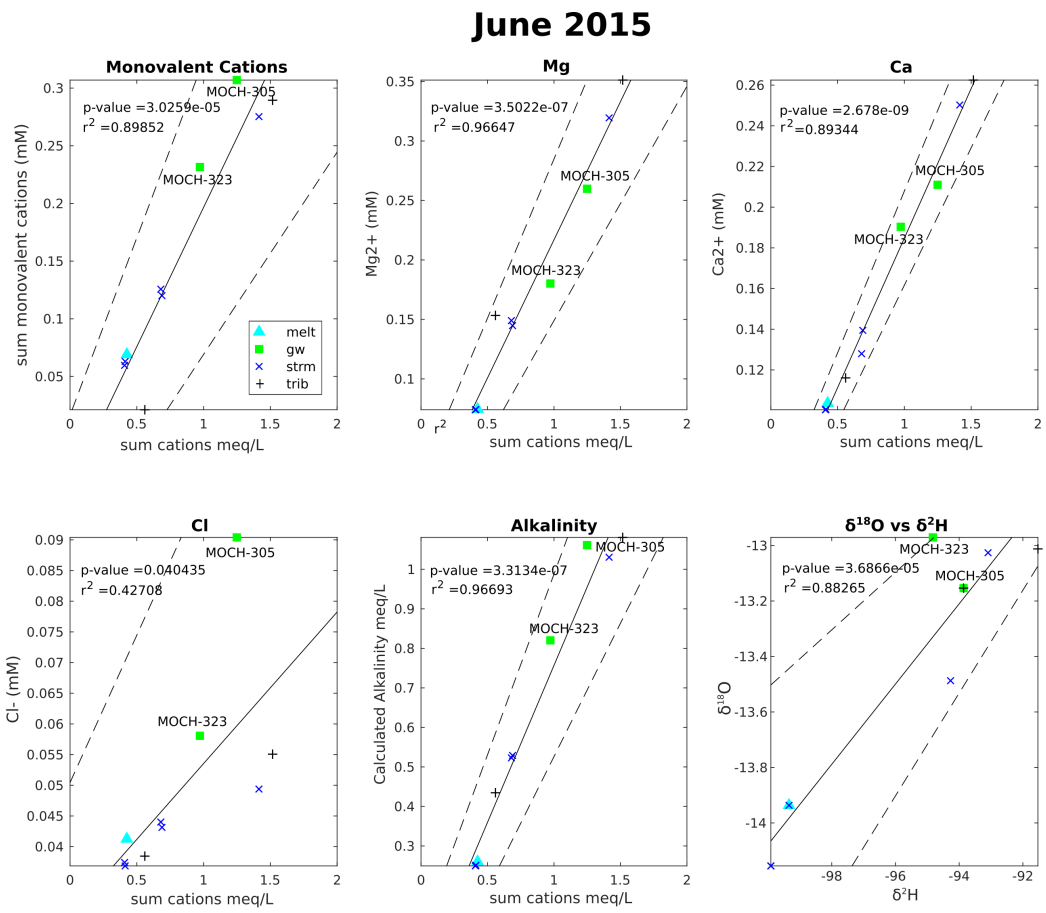

Figure A6: Bivariate diagrams of tracers selected for June 2015 analysis. The solid black lines represent linear regressions through all samples and dashed black lines indicated the regressions' 95% confidence intervals. Samples from the main Rio Mocha channel before and after the Gavilan stream joins it (filled green circles) consistently plot outside or away from the mixing line created between groundwater and meltwater. MOCH-S7 was not considered in the analysis (shown with hallow square). These samples are also responsible for the poor R2 and p-values of sulfate and chloride.

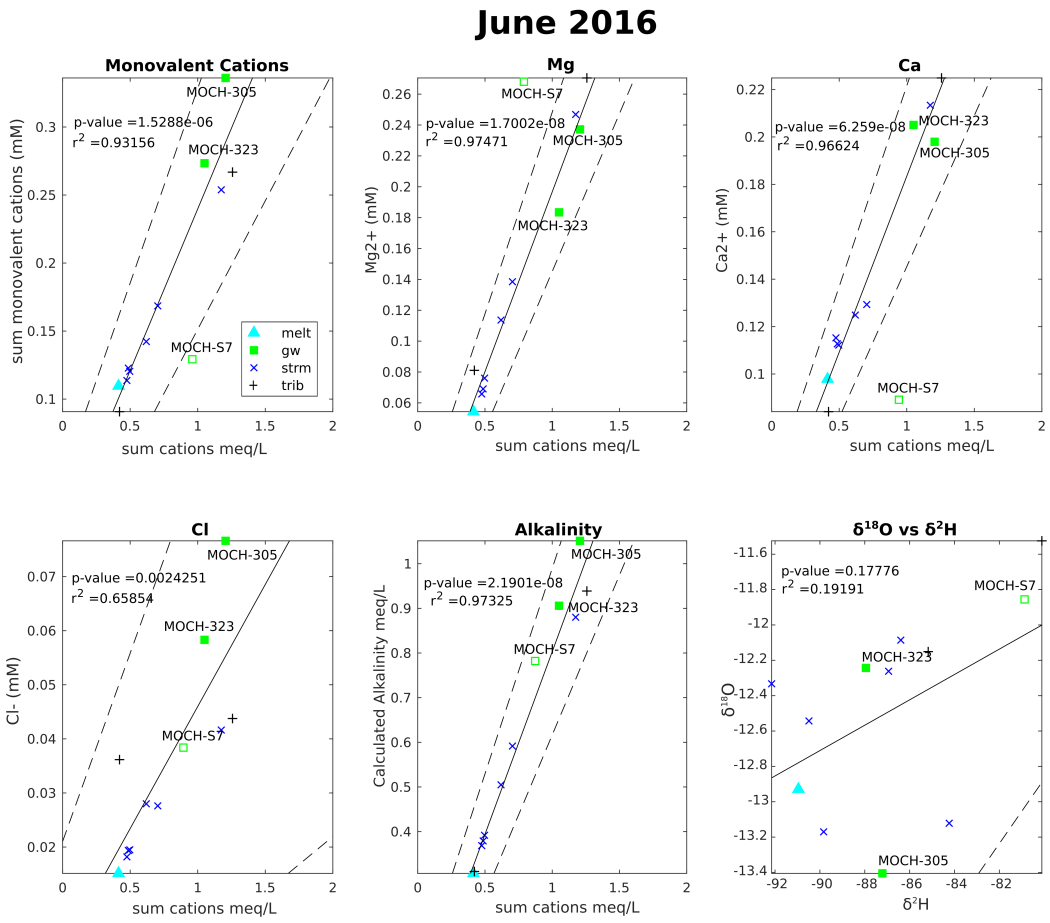

Figure A7: Bivariate diagrams of tracers selected for June 2016 analysis. The solid black lines represent linear regressions through all samples and dashed black lines indicated the regressions' 95% confidence intervals. Samples from the main Rio Mocha channel before and after the Gavilan stream joins it (filled green circles) consistently plot outside or away from the mixing line created between groundwater and meltwater. MOCH-S7 was not considered in the analysis (shown with hallow square). These samples are also responsible for the poor R2 and p-values of sulfate and chloride.

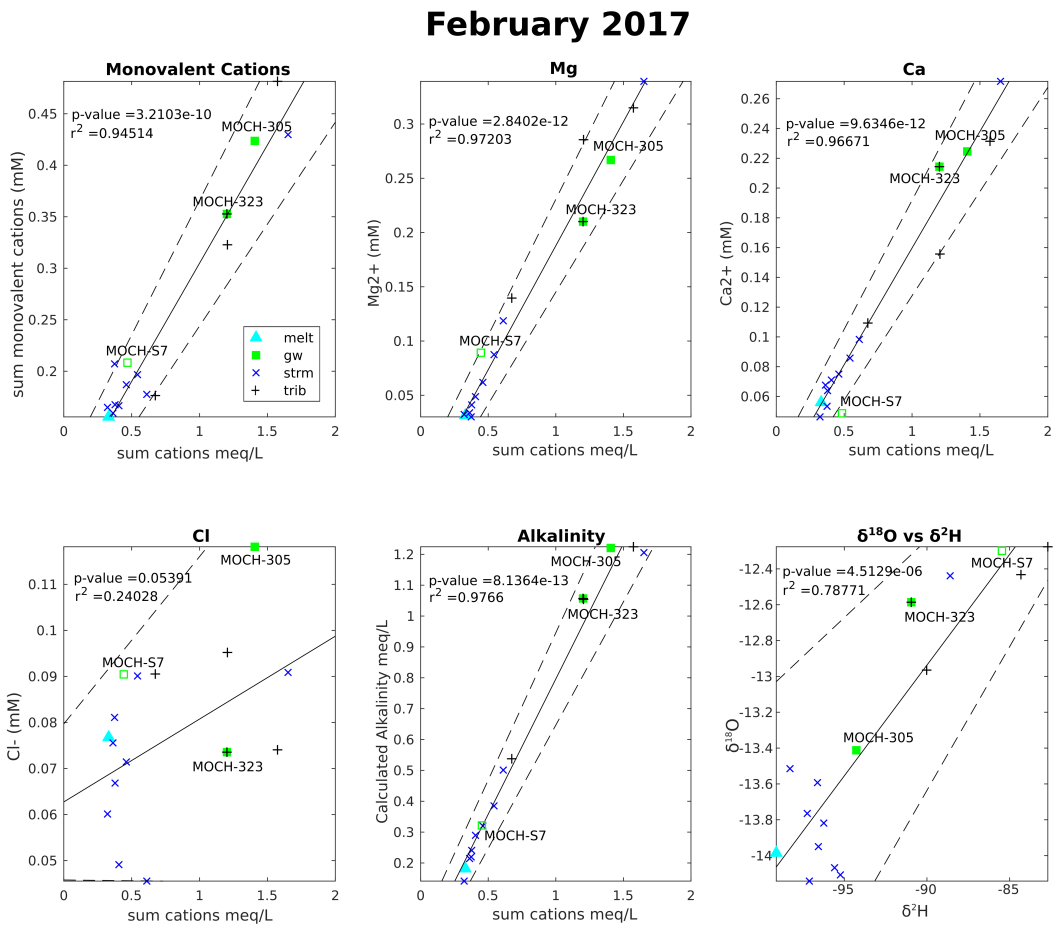

Figure A8: Bivariate diagrams of tracers selected for February 2017 analysis. The solid black lines represent linear regressions through all samples and dashed black lines indicated the regressions' 95% confidence intervals. Samples from the main Rio Mocha channel before and after the Gavilan stream joins it (filled green circles) consistently plot outside or away from the mixing line created between groundwater and meltwater. MOCH-S7 was not considered in the analysis (shown with hallow square). These samples are also responsible for the poor R2 and p-values of sulfate and chloride.

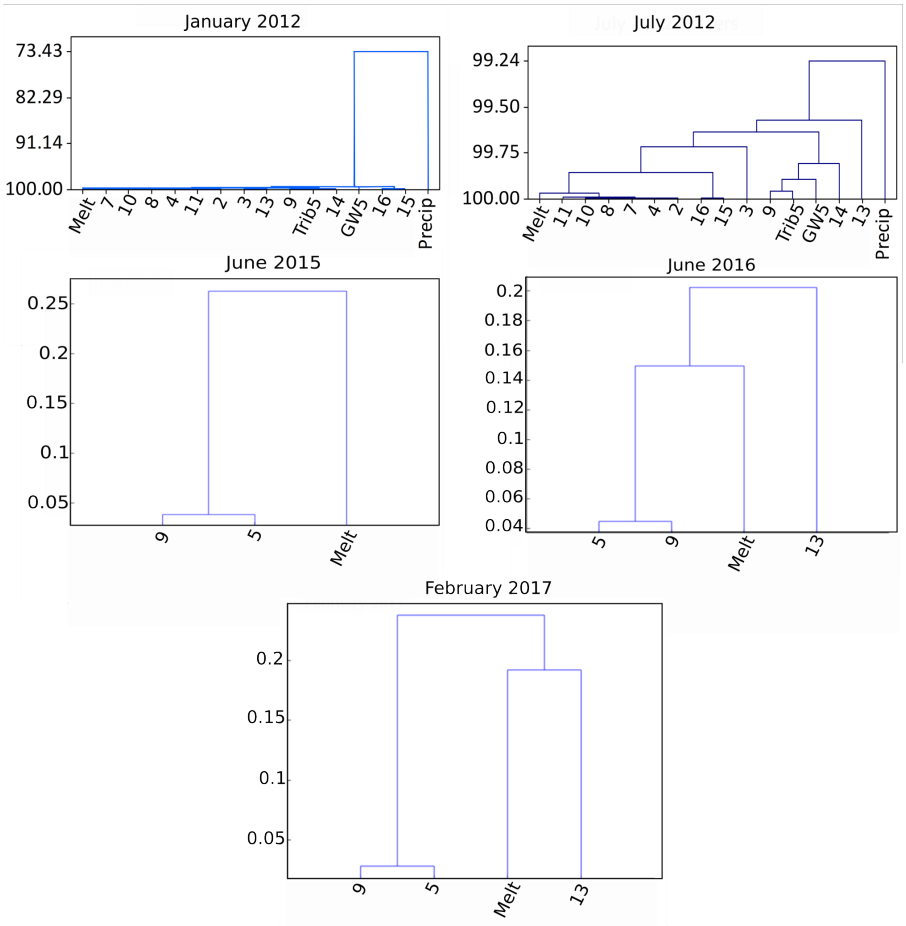

Figure A9: Hierarchical cluster analysis dendrograms for tracers used in HCBM for January 2012, July 2012, June 2015, June 2016, and February 2017. Sample grouping verifies effectiveness of selected tracers in distinguishing between source waters, as groundwater samples (GW) cluster separately from melt water (Melt) samples. GW-7 is considered an outlier, and is suspected to be a mixed source sample or to originate from a unique geology.

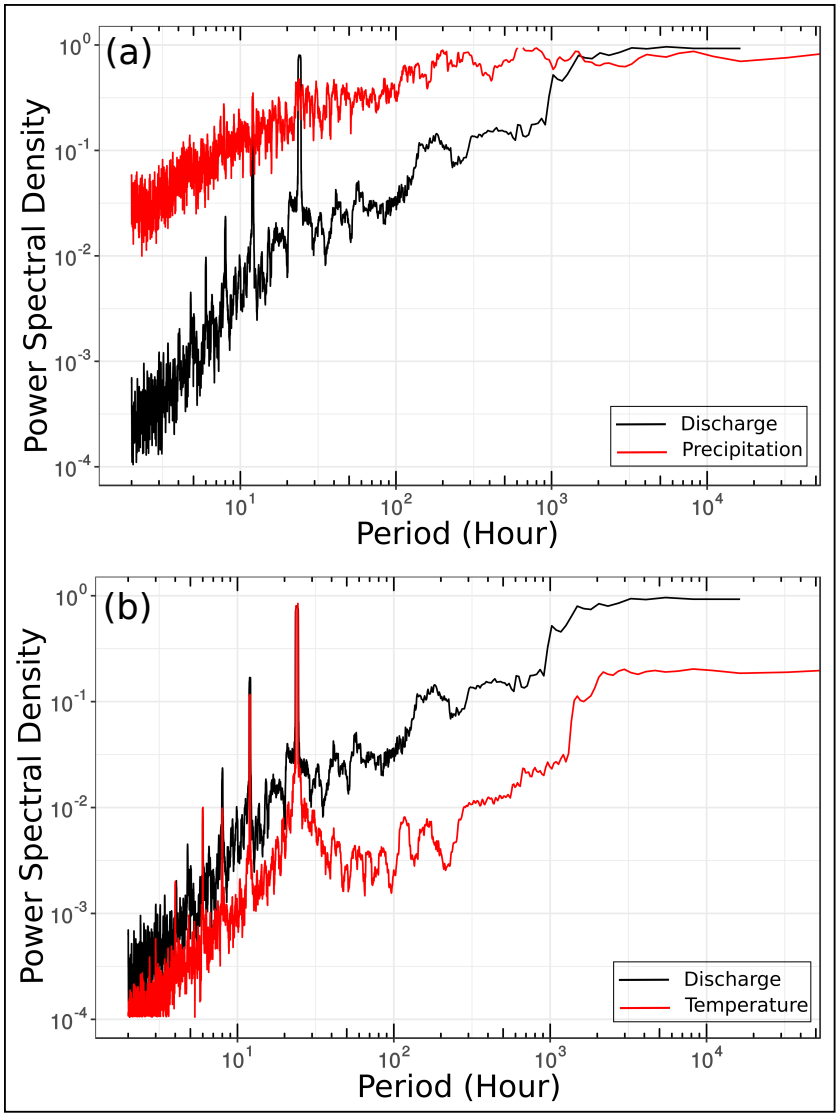

Figure A10: Power spectral density of **(a)**discharge and temperature, **(b)** discharge and precipitation

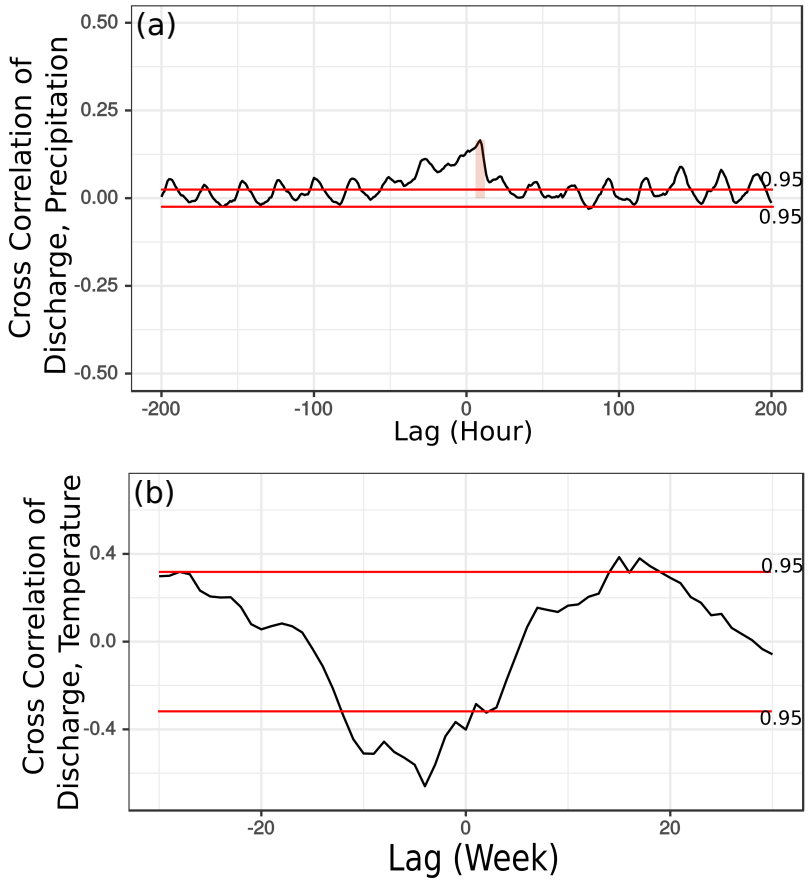

Figure A11: Cross-correlation of **(a)**hourly discharge and precipitation, **(b)** weekly discharge and temperature

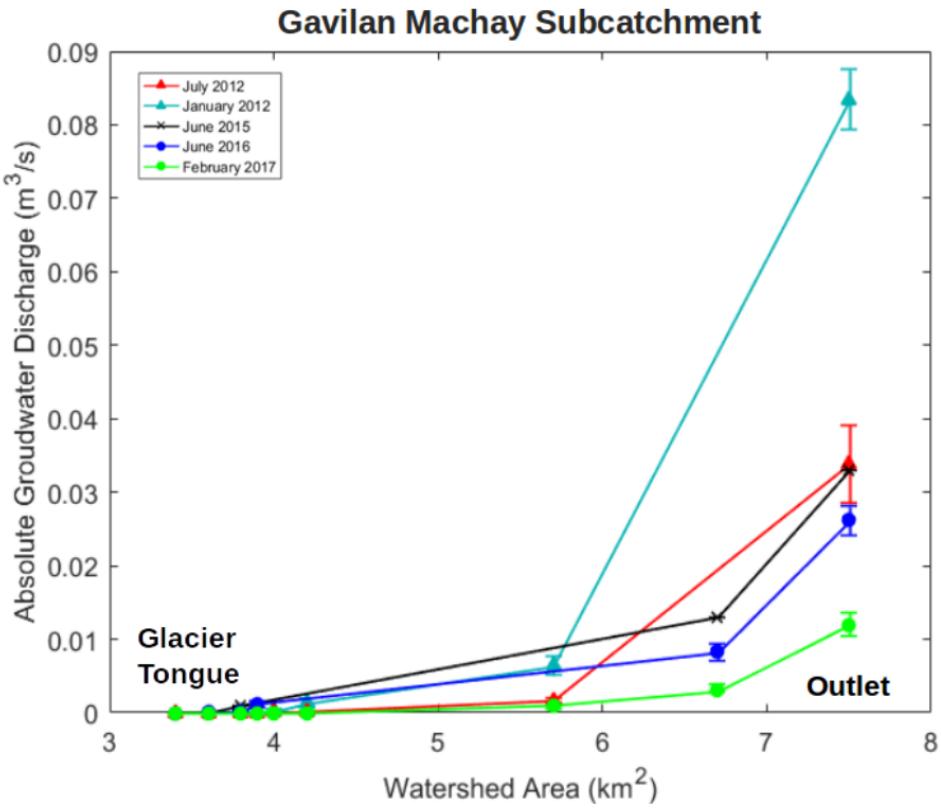

Figure A12: Calculated absolute groundwater discharge versus percentage of total watershed area drained for Gavilan Machay subcatchment (McLaughlin, 2017).

A.2 Hydrochemical Basin Characterization Model (HBCM)

The following set of mass-balance equations for J tracers applies to each HBCM cell:

$$C_{tot_j} = \frac{\sum_{i=1}^{I}(C_{i,j} * Q_i) + \epsilon_j}{Q_{tot}} \tag{A1}$$

Where:

j: index for a specific natural tracer, 1 through J

i: index for a specific source to the cell (ice, tributary, or groundwater), 1 through I

C_{tot_j}: concentration of tracer j at the cell outlet

$C_{i,j}$: concentration of tracer j in source i

Q_{tot}: Total discharge at cell outlet

Q_i: Contribution to discharge from source i

ϵ_j: residual error between the observed and predicted concentration flux out of the cell for tracer j

HBCM solves for the unknown relative contributions of each source (Q_i/Q_{tot}) by minimizing the sum of the residual errors:

$$\sum_{j=1}^{J} \epsilon_j \tag{A2}$$

In order to over-constrain the problem, the model requires $J = I$ tracers and, preferably, $J > I$ tracers should be utilized in order to avoid the possibility of correlated tracers that do not independently constrain the problem. HBCM checks that a tracer is conservative within each cell via three tests:

1. A tracer value in a cell outflow cannot be outside the range bracketed by the possible contributors;
2. The tracer value at the cell outflow, along with that of at least one input component, must be greater than the detection limit of the analytical methods (confirmed by user); and
3. There must be a minimum 5% difference between the concentration of a tracer from each source.

If any of these requirements is not met, HBCM will reject the tracer for use in the cell.

A.3 Tables

	Observed				Flux-PIHM pedotransfer function results						
	Sand (%mass)	Silt (%mass)	Clay (%mass)	OC (%mass)	KINF (m/s)	KSATV (m/s)	KSATH (m/s)	SMCMAX (-)	SMCMIN (-)	ALPHA (1/m)	BETA (-)
Podwojewski et al. 2002, Pantano 60-80	26	41	8	12	4.52E-07	6.44E-07	6.44E-06	0.479	0.05	1.908	1.157
Patano 80-95+	33	39	14	8	1.47E-06	1.58E-06	1.58E-05	0.481	0.05	3.491	1.136
Humid páramo 0-15	26	44	7	10	6.24E-07	1.03E-06	1.03E-05	0.48	0.05	2.267	1.173
Humid páramo 15-30	32	41	8	7	1.51E-05	6.76E-06	3.05E-05	0.418	0.05	5.34	1.26
Dry páramo 0-15	30	43	8	7	8.28E-05	3.71E-05	6.96E-05	0.493	0.05	5.82	1.22
Dry páramo 15-30	35	33	20	5	8.28E-05	3.71E-05	6.96E-05	0.493	0.05	5.82	1.22
Minaya (2016), Low Elev.	20.28	31.98	6.24	22	3.71E-08	8.42E-08	8.42E-07	0.482	0.05	0.327	1.144
Minaya (2016), Middle Elev.	26.07	30.81	11.06	21	6.13E-08	1.03E-07	1.03E-06	0.479	0.05	0.466	1.124
Minaya (2016), Highest Elev.	23.4	39.6	6.3	10	4.28E-07	1.70E-07	1.70E-06	0.465	0.05	1.442	1.1

Table A1: Páramo soil measurments applied into pedotransfer functions (Podwojewski et al., 2002; Minaya, 2016)

Appendix B

Supplemental Materials: Spatiotemporal Drivers of Hydrochemical Variability in a Tropical Glacierized Watershed in the Andes

B.1 Introduction

The supporting information below includes text, tables, and figures that provide additional details on the methods used for the paper and other results related to the main points in the text. This includes more information on XRD analysis, model calibration, and supporting interpretations.

B.2 XRD and Grain Size Analysis of Soil Samples

In addition to soil samples S-1, S-2, and S-3, which were collected over a single shallow depth interval, an additional deeper profile was augered at a fourth location, S-4 (located just downgradient of S-3, outside of Gavilan Machay), where the soil auger did not hit

refusal on shallow cobbles. At S-4, two separate depth intervals were analyzed: 3-20 cm and 20-40 cm. The XRD analyses at the two different depths suggest that the vertical soil structure may be fairly homogeneous (Table B1). We assume that this could be representative of the watershed mineralogy.

Mineral	**Chemical Formula**	**S-4 at Depth 3-20 cm**	**S-4 at Depth 20-40 cm**
Albite	$Na(AlSi_3O_8)$	✓	✓
Anorthite	$Ca(Al_2Si_2O_8)$	✓	✓
Diopside	$Ca(Mg,Al)(Si,Al)_2O_6$	✓	✓
Sanidine	$K(Si_3Al)O_8$	✓	

Table B1: Soil Mineralogy of sample S-4 at depth 3-5 and 20cm at Volcán Chimborazo.

To further investigate the soil texture of the watershed, approximately 50g of each bulk soil sample was dry-sieved by hand. We conducted grain size analysis and found 8.5% and 18% of the bulk samples collected from approximate 4-25 cm depth intervals at 3800 m a.s.l. and 4500 m a.s.l., respectively, were clay- and silt-sized particles (smaller than 63 μm diameter). These estimates are consistent with previous soil studies on Chimborazo. Podwojewski et al. (2002) showed that shallow soil samples at 3800-4200 m a.s.l. on the drier northwestern flank of Chimborazo contain an average of 8.5% clay. Bartoli et al. (2007) found a slightly higher amount of 23% organo-mineral clay at 3800 m a.s.l. using a larger 2 mm diameter definition. It is possible the fine fraction in our samples also contains organo-mineral clays that were resistant to our hydrogen peroxide treatment, as well as minerals with a poor crystalline structure. Bartoli et al. (2007) characterized the Chimborazo's soils as aluandic andosols, which are regarded as non-allophanic andosol predominantly composed of aluminum complexed with organic matter (Takahashi & Shoji, 2002).

B.3 PHREEQC Model Simulations and Results

The measured major ion concentrations in groundwater (Table 3.2 in the main text) were used to evaluate the saturation index (SI) of the dominant minerals (albite and

diopside) found through XRD as well as common clay and secondary minerals (kaolinite, halloysite, and gibbsite) that can potentially precipitate following silicate mineral weathering. Saturation index of each mineral is calculated as follows:

$$SI = log(\frac{IAP}{K_{eq}}) \tag{B1}$$

where IAP is the ion activity product of the dissolved ions of the mineral (Table 3.3 in the main text) and K_{eq} is the solubility product. SI is negative when the solution is under-saturated (if the mineral is present, it can dissolve), it is zero when the mineral and solution are at chemical equilibrium, and it is positive when the solution is over-saturated (precipitation can occur to form the respective mineral). Table B2 shows the SI values for kaolinite, halloysite, gibbsite, albite, and diopside at different locations in the watershed, calculated by PHREEQC Parkhurst et al. (1999).

Mineral	**Location**	**Saturation Index (SI)**
Kaolinite	GW-1	-0.98
	GW-2	-0.13
Hallyosite	GW-1	-1.34
	GW-2	-0.65
Gibbsite	GW-1	-0.25
	GW-2	-0.09
Albite	GW-1	-11.5
	GW-2	-9.53
Diopside	GW-1	-2.04
	GW-2	-1.61

Table B2: Kaolinite, hallyosite, gibbsite, albite, and diopside saturation indexes (SI) calculated using the PHREEQC model. Sampling locations are shown in Figure 2a.

The SI values presented in Table B2 shows that the solution is undersaturated with respect to albite and diopside, such that dissolution can occur. Results further show that the solution is undersaturated with respect to kaolinite, gibbsite, and halloysite, indicating they have not yet begun to precipitate - though they may be close at GW-2, near the outlet).

B.4 Model Calibration With Hydrochemical Constraints

The implementation of BioRT-Flux-PIHM enables us to constrain flow pathways using both hydrological and hydrochemical data, through coupling of hydrological, land-surface, and reactive transport processes. Integrating solute and tracers concentrations into the calibration reduces the uncertainty associated with hydraulic parameter estimates and the streamflow partitioning Schilling et al. (2019). Constraining the model simulations with observed hydrochemical concentrations in addition to stream discharge resulted in lower calibrated porosity and van Genuchten parameters than those obtained via calibration without hydrochemical constraints in saberi2019 (Table B3). saberi2019 calibrated the model to solely discharge observations, and hydrochemical data were only indirectly considered through comparison of model simulations with coarse-scale estimates of melt and groundwater contributions from a simple hydrochemical mixing model.

	KINFV (m/s)		KSATV (m/s)		KSATH (m/s)		Porosity		α (1/m)		β (-)	
	W/o	W	W/o	W	W/o	W	W/o	W	W/o	W	W/o	W
Ice-covered	2.07E-7	1.64E-7	4.56E-8	5.36E-8	6.71E-7	7.56E-7	0.461	0.296	0.863	0.412	1.06	1.038
Sparsely Vegetated	1.43E-7	1.74E-7	4.63E-8	4.85E-8	4.63E-7	5.85E-7	0.459	0.296	0.585	0.437	1.063	1.038
Grassland	1.23E-7	1.87E-7	4.02E-8	5.27E-8	4.02E-7	5.27E-7	0.493	0.297	0.488	0.469	1.066	1.039

Table B3: Calibrated parameters with hydrochemical constraints (this study) ("W/") and without hydrochemical constraints Saberi et al. (2019) ("W/o"). Parameters include hydraulic conductivities for vertical infiltration (KINFV), vertical saturated flow (KSATV), horizontal saturated flow (KSATH), porosity, residual soil moisture, and shape parameters (α and β) for the van Genuchten moisture retention curve: $\theta = \theta_{res} + porosity \times \left(\frac{1}{1+|\alpha\psi|^{\beta}}\right)^{(1-\frac{1}{\beta})}$, with water content θ and pressure head ψ.

Although the estimated ice-melt contribution to discharge remained unchanged (52%), direct model calibration to hydrochemical data provided a stronger constraint on melt-groundwater interactions. The estimate of discharge originating from meltwater-fed groundwater that first infiltrates and travels as groundwater before flowing to streams changed from a highly uncertain 16% to a much better constrained 37% after calibrating the model on hydrochemical observations (Figure B1 a). The percent melt contribution to the groundwater is estimated using simulation scenarios with and

without ice melt:

$$\%\ Melt\ in\ Groundwater = \frac{(Groundwater_{WithIcemelt} - Groundwater_{WithoutIcemelt})}{Groundwater_{WithIcemelt}} \times 100 \tag{B2}$$

where $Groundwater_{WithIcemelt}$ and $Groundwater_{WithoutIcemelt}$ is the lateral groundwater flow to the stream in scenarios with and without ice-melt, respectively. Simulations show that as the temperature increases during the El Niño event, the ice melt contribution to the groundwater increases, with some time lag (Figure B1).

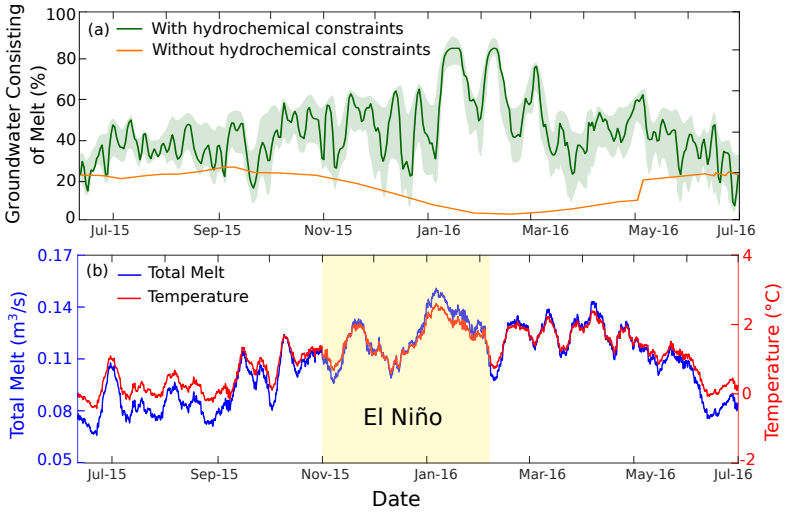

Figure B1: Temporal variability over the watershed of (a) the percentage of groundwater that constitutes ice melt, with the calibration uncertainty in green shading; (b) average air temperature over the ablation zone (glacier-covered areas below the ELA (5050 m a.s.l.)) and simulated glacier melt production. The yellow box highlights the time period during which an El Niño event occurred over the watershed. The x-labels indicate the start of the corresponding month.

B.5 Model Calibration using Monte Carlo Simulations

Input parameters included in the model calibration are shown in Table B4 along with the range of literature values from Andean and other volcanic sites, the standard deviation of values found in literature, pre-calibration nominal values for the parameters, the

pre-calibration range of values for the Monte Carlo runs, the calibrated parameter value, and the calibration uncertainty range. Pre-calibration nominal values for soil hydraulic properties were set to measurements from Chimborazo presented in Podwojewski2002, and pre-calibration nominal values for mineral SSA values were first manually tested within the literature range for computational efficiency. The pre-calibration range was set to the pre-calibration nominal value ± the literature-based standard deviation. Uniformly distributed parameters were drawn using Latin Hypercube sampling from the pre-calibration range for the Monte Carlo runs.

Input Parameter	**Range Found in Literature**	**Literature StdDev**	**Literature References**	**Pre-Calib Nominal Value**	**Pre-Calib Range Assigned**	**Calibrated Value**	**Calibration Uncertainty Range**
Horizontal Hydraulic Conductivity (m/day)	0.009 to 6.015	2.24	Podwojewski et al., 2002 Minaya, 2016 Celleri and Feyen, 2009	Grass=0.89 Bare-Soil=0.83 Ice-covered=0.77	0.009 to 3.13	Grass=0.045 Bare-Soil=0.042 Ice-covered=0.039	0.02 to 0.6
Vertical Hydraulic Conductivity (m/day)	0.0009 to 3.2	1.36	Podwojewski et al., 2002 Minaya, 2016	Grass=0.0089 Bare-Soil=0.0087 Ice-covered=0.0077	0.0009 to 1.46	Grass=0.0045 Bare-Soil=0.0042 Ice-covered=0.0039	0.0009 to 0.24
Porosity	0.25 to 0.8	0.13	Podwojewski et al., 2002 Minaya, 2016 Shoji et al., 1993	0.38	0.25 to 0.51	0.3	0.25 to 0.42
α	0.3 to 5.82	2.2	Podwojewski et al., 2002 Minaya, 2016 Montzka et al., 2017	Grass=2.26 Bare-Soil=2.08 Ice-covered=1.97	0.3 to 4.47	Grass=0.47 Bare-Soil=0.43 Ice-covered=0.41	0.3 to 1.2
β	0.8 to 4.3	0.96	Podwojewski et al., 2002 Minaya, 2016 Montzka et al., 2017	1.173	0.9 to 2.12	1.04	0.9 to 1.5
Albite SSA (m^2/g)	0.02 to 1.09	–	Brantley, 2008	0.07	0.02 to 1.09	0.075	0.02 to 0.5
Diopside SSA (m^2/g)	0.001 to 2.3	–	Brantley, 2008	0.07	0.001 to 2.3	0.086	0.001 to 1.5

Table B4: Seven key parameters perturbed for the Monte Carlo runs, the range of literature values, the standard deviation (StdDev) of literature values, references, the pre-calibrated nominal value and range, and the calibrated value and uncertainty.

Among the 100 Monte Carlo simulations, we found a unique set of parameters that minimizes the mismatch between simulations and observations, quantified using NRSMD_{ave} (Equation 3.6 in the main text) (Figure B2). The normalization term s in Equation 3.6 (in the main text), is often set to the observation uncertainty, which is typically much larger than instrument errors due to field installation/sampling errors and representativeness errors between the model and field data. Thus, we used the standard deviations of each observation type (stream discharge, major ion concentrations in

the stream, and major ion concentrations in groundwater) as a measure of spread for the corresponding s. The parameter combination with the lowest NRSMD$_{ave}$ value was used in the final simulation.

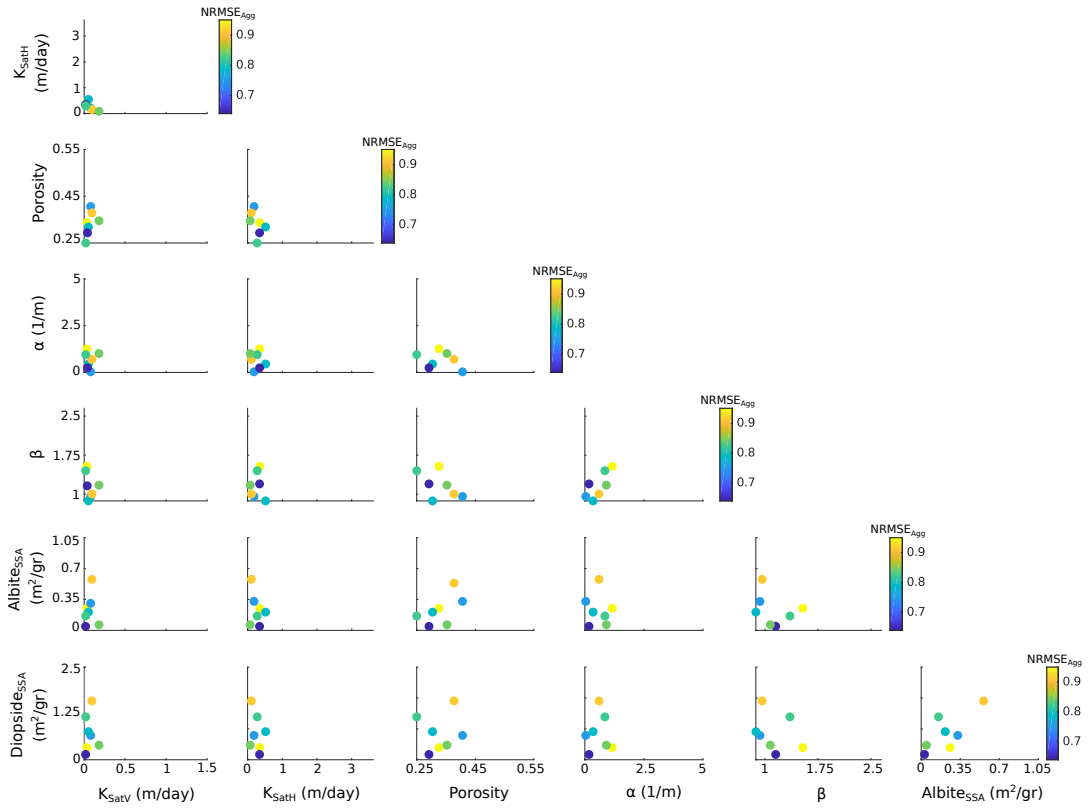

Figure B2: Monte Carlo simulation results with NRMSD$_{ave} < 1$ (equation 3.6), with the lowest NRMSD$_{ave}$ of 0.45 representing the best consistency with observations, and the set of simulations with NRMSD$_{ave} < 1$ representing the calibration uncertainty. The axis limits are set to the pre-calibration parameter range for all Monte Carlo simulations (Table B4) to demonstrate that the calibrated parameter set and uncertainty are well-constrained by the observations.

From the 100 Monte Carlo simulations, 7 model simulations had NRMS$_{Dave} < 1$, and these were chosen to represent the calibration uncertainty. The significantly smaller calibrated uncertainty ranges relative to the pre-calibration range for the Monte Carlo runs (Figure B2) lend confidence in the final estimates.

In addition to results for Na^{+} in the main document (Figure 3.4), the calibrated concentrations of Ca^{2+} and Mg^{2+} at four different sampling points along the stream (SW-1 to SW-4) are shown in Figure B3. Measured concentrations during June 2015 and June 2016 field campaigns are shown in circle and diamond shapes, respectively. The shaded area represents the calibration uncertainty accompanying the simulations.

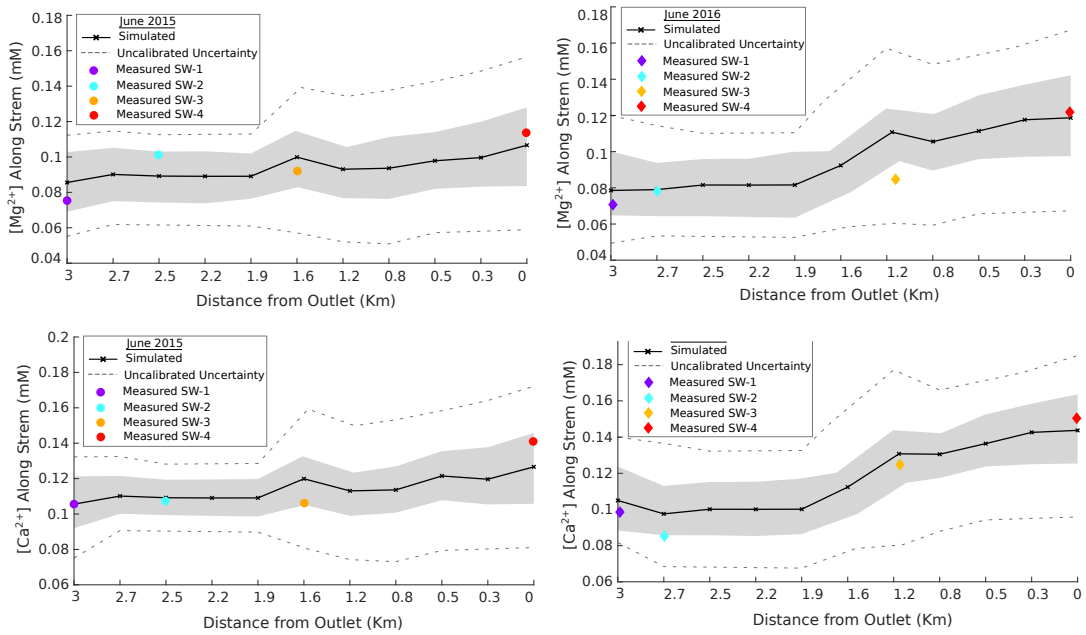

Figure B3: Simulated Ca^{2+} and Mg^{2+} concentrations at four different locations along the stream compared to measured concentrations from June 2015 and June 2016. Dashed lines show the uncertainty boundary of the unconstrained Monte-Carlo simulations. Shaded area shows the uncertainty in the calibrated result, which is significantly reduced from the unconstrained range.

B.6 Steady-State Mass Balance Equation for Non-reactive and Reactive Solutes

B.6.1 Non-reactive Solute (Cl^-)

A simple mass balance assuming steady-state helps demonstrate the expected relative controls of infiltration and ET on groundwater concentrations of non-reactive solutes:

$$C_p \times I = G_{gw} \times (I - ET) \tag{B3}$$

where C_p is the solute concentration in precipitation and ice-melt (assumed to be uniform over the watershed), I is infiltration (I = Precipitation + Melt - Runoff), and C_{gw} is the average solute concentration in the saturated and unsaturated zones. Eq. B3 can be rearranged to show the dependence of groundwater concentrations of Cl^- on the ratio of ET to infiltration (higher ET/I results in higher groundwater concentration):

$$C_{gw} = \frac{C_p}{1 - (\frac{ET}{I})} \tag{B4}$$

B.6.2 Reactive Solutes

The steady-state mass balance equation for reactive solutes is a straightforward extension of the non-reactive case for Cl^- (equations B3 and B4):

$$C_{gw} = \frac{(R_r + C_p \times I)}{I - ET} \tag{B5}$$

where R_r is the solute release rate through mineral dissolution. It can be seen that with ET>0, the solute input from mineral dissolution (R_r) is amplified by a factor of $\frac{1}{(1-\frac{ET}{I})}$ when determining the groundwater concentration.

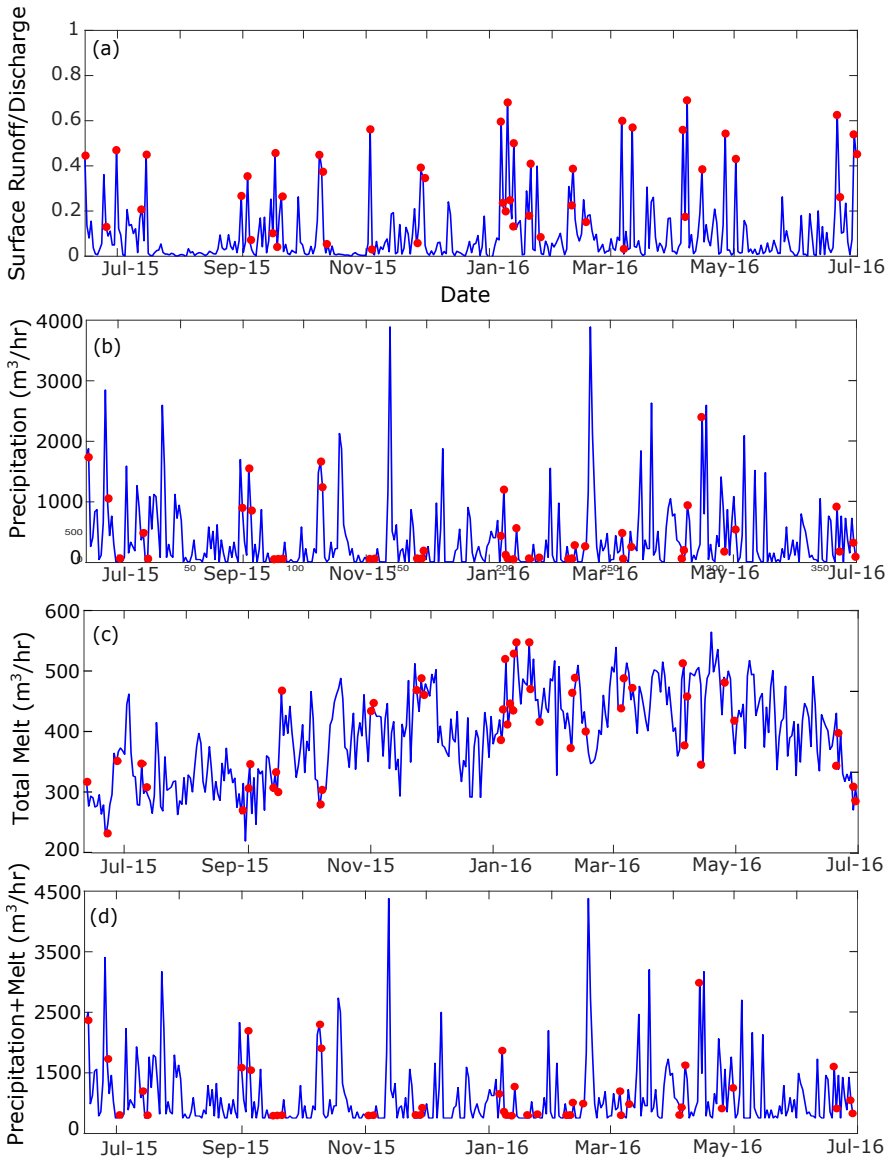

Figure B4: (a) The Surface runoff to stream discharge ratio, (b) precipitation, (c) ice melt input, (d) precipitation plus ice melt. Red dots represent the dilution events at the outlet (red dots correspond to those shown in Figure 3.8 in the main text). Most of the red dots occur when there is a melt peak corresponding with a precipitation peak.

Figure B5: A roadcut showing deposited ash layers on Volcán Chimborazo.

Appendix C

Supplemental Materials: Evaluating the Hydrological Response of a Tropical Glacierized Mountainous Watershed to Upslope Vegetation Migration

C.1 Figures

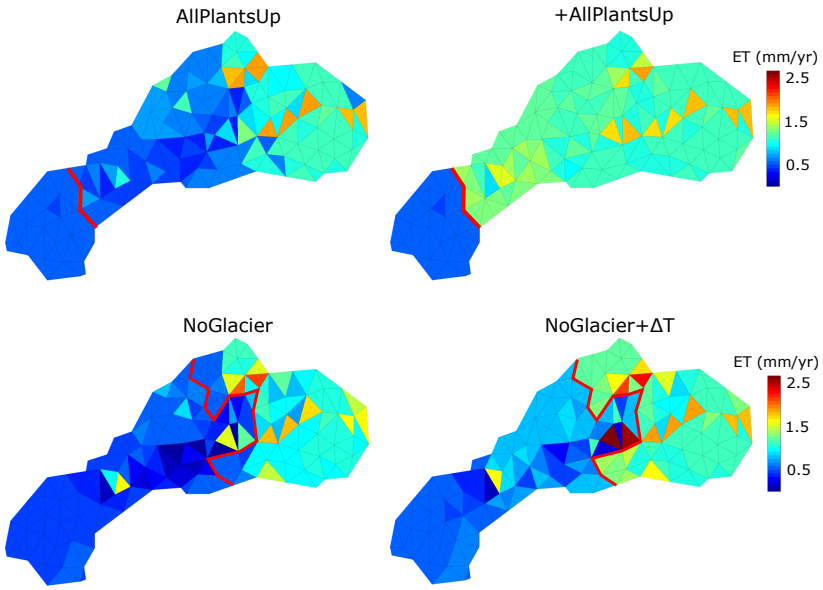

Figure C1: Time-averaged simulations of total evapotrasnpiration for AllPlantsUp, +AllPlantsUp, NoGlacier, and NoGlacier+ΔT scenarios. The vegetation line is shown with red line.